Davy-Faraday Research Laboratory,

The Royal Institution of Great Britain

Department of Chemistry, University College London,

University of London

A Theoretical Study of Lithium Intercalation in Transition Metal Oxides

Thesis submitted for the degree of Philosophiæ Doctor

by

James Spencer Braithwaite

2000

Abstract

The physical and electronic structural changes that occur during lithium intercalation into two vanadium oxides. V_2O_5 and V_6O_{13}, and the mixed metal spinel materials, $Li_xCo_yMn_{4-y}O_8$, where y = 0,1,2, 4 and x = 0,1,2, have been studied using a combination of theoretical methods. These transition metal oxides are of great interest as are possible cathode materials in solid-state lithium-ion batteries. Both interatomic potential based static lattice or 'atomistic' modelling, and electronic structure calculations based on Density Functional Theory have been used in this study.

An interatomic potential model for V_6O_{13} has been derived using empirical fitting methods. We use Mott-Littleton methods to find the lowest energy sites occupied by intercalated lithium ions in both V_2O_5 and V_6O_{13}. Electronic structure methods have been used to investigate the relative stability of a series of $Li_xV_2O_5$ phases, where $0 \leq x \leq 2$, and $Li_xV_6O_{13}$ phases, where $0 \leq x \leq 4$, which has allowed us to predict average discharge voltages for both materials that are in good agreement with experiment. Calculated electron density distributions show that the lithium insertion reaction is accompanied by the localised reduction of vanadium metal atoms in both $Li_xV_2O_5$ and $Li_xV_6O_{13}$. Li^+ has been shown to be mobile along the [*010*] direction in V_2O_5.

Calculated average voltages for the spinel family, $Li_xCo_yMn_{4-y}O_8$, are in good agreement with experiment, and clearly show that the presence of cobalt is fundamental to the generation of voltages over 5V. The oxygen atoms are also shown to accept electron density during lithium intercalation and may play a role in the generation of such high voltages.

Acknowledgements

Firstly, I would like to thank Richard Catlow, John Harding, and Julian Gale for all their help and support over the last three years. Not only have they given me an excellent grounding in theoretical chemistry, but they have also proof read this thesis – thank you. Thanks also to Sally Price, my supervisor at UCL Chemistry, for her assistance, advice, and a little FORTRAN.

I feel lucky to have been able to work at the DFRL, where I have been surrounded by a group of people that are very knowledgeable and also good friends. Thanks to Alexei Sokol, Scott 'The Wit' Woodley, and Ben Slater for help on theoretical stuff, and Furio Cora for advice on modelling transition metal oxides with DFT i.e. 'don't bother'. Sam for being a great mate throughout (take it easy, Daddy). Martin and Stef for the good times at Goldhawk Road - and Andy Monteith for that matter, Ian, Carolyn, Peter, Jo, Jo, Justin, Matt, Gavin, Steve, Will, Mark C, Lee 'Webmaster', Lee 'Lardby', Lee 'Cantona', Andy Davies, David Coombs, Mark Green, Marta, and everyone else – you have all made working at the RI a lot of fun.

Mum and Joy, thanks for always being there, this thesis is dedicated to you.

And finally, Gayna, thank you for putting up with me while all this has been going on. I apologise for the number of times I've said, 'it'll be finished next week'. Well now it is.

Contents

List of Figures

List of Tables

Chapter 1

Introduction

In this thesis we use a combination of theoretical techniques to model the lithium intercalation reaction in a number of transition metal oxide materials, and thereby gain a better understanding of the structural and electronic changes that occur at the cathodes of solid-state lithium-ion batteries.

In the last ten years there has been a huge increase in the demand for small, portable, and rechargeable electronic devices; mobile phones and laptop computers being two outstanding examples. To meet this demand, the need to develop portable power sources has become increasingly important, with lithium-ion batteries being a leading technology in this area. The demands on these battery components are high, with size and weight at a premium, while consistent performance over a lifetime of over 100 recharge cycles is desirable. Environmental concerns are also of increasing importance: at present, commercial lithium-ion batteries are constructed using electrode materials that contain toxic transition metals, such as cobalt.

An important possible future use of secondary battery technology will be in Zero Emission Vehicles, especially as legislation to cut vehicle emissions, already in place in California, is likely to be enacted in many developed countries. This type of application offers even more challenges, as the voltages and energy densities of existing lithium-ion cells are not high enough, while their cost, at present, is prohibitive. With the potential of solid-state batteries in mind, the United States Department of Energy and a consortium of US car manufacturers have set a number of performance targets for batteries designed for electric vehicles (DOE 1987). It is hoped that this kind of exercise will stimulate further investment in the field, and speed up new developments.

A selection of these targets are listed below:

Specific energy at a discharge rate of capacity / 3	200Wh/kg.
Cycle life at 80% depth of discharge	1000 cycles
Normal recharge time	6 hours
Battery lifetime	10 years
Cost	< 100 $/kWh

Table 1.1. Performance targets for battery cells in electric vehicles.

While some of the targets in Table 1.1 have already been achieved, for example the cathode material V_6O_{13} has a theoretical specific energy of over 800Wh/kg, it is still a relatively distant goal to combine these performance targets in a single battery system.

1.1 Basic electrochemical cell construction

A traditional electrochemical cell is made by separating two electrochemically active materials (the electrodes), with an electrolyte that is an ionic conductor but an electrical insulator. The cell voltage is produced by the potential difference caused by the redox processes that occur at each electrode. The cathode is defined as the electrode with the higher electron affinity, and therefore accepts electrons during the cell reaction, while oxidation takes place at the anode. As electrons move through the circuit, from the anode to cathode, there is an accompanying movement of ions through the electrolyte. In the simplest cells the electrodes are made from two different metals and the electrolyte is an aqueous salt solution containing both metal ions. As the battery is discharged, the anode is 'dissolved' as ions are released into the electrolyte, while reduction at the cathode results in plating of the electrode. A typical set up for this type of basic electrochemical cell is shown in Fig. 1.1

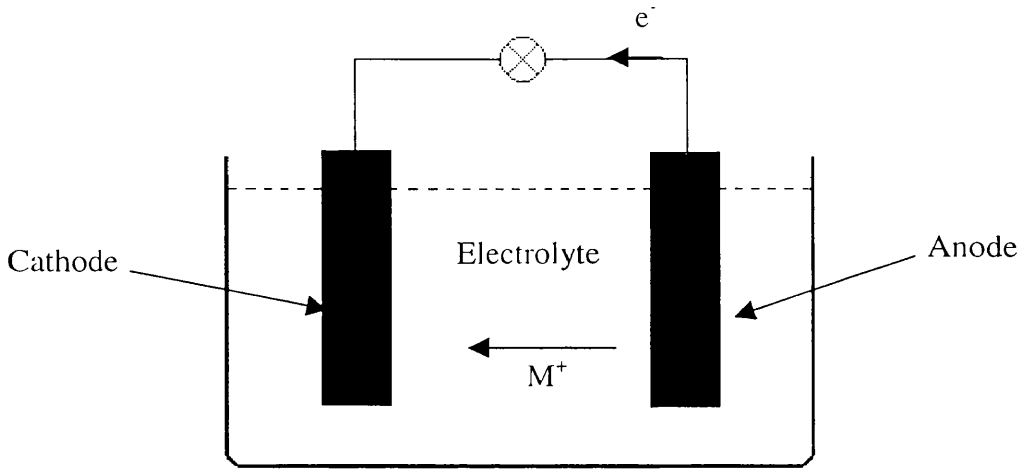

Fig. 1.1. Traditional cell during discharge.

One of the most successful secondary batteries, which are still widely used today, is the NiCd cell, developed by Waldemar Jugner in 1899. The cell reactions, which produce a cell potential of 1.3V, are as follows:

Anode: $Cd + 2OH^- \rightarrow Cd(OH)_2 + 2e^-$

Cathode: $2NiOOH + 2H_2O + 2e^- \rightarrow 2Ni(OH)_2 + 2OH^-$

Total cell reaction: $Cd + 2NiOOH + 2H_2O \Leftrightarrow Cd(OH)_2 + 2Ni(OH)_2$

The main disadvantage of this cell arrangement is the use of cadmium, a heavy metal that is highly toxic and persists in the environment over long periods of time. The NiMH cell, which replaces the cadmium electrode with a nickel hydride, is considerably more environmentally friendly. This NiMH battery has a specific energy density of

around 60Wh/kg, which, although this battery is in wide use, compares unfavourably with the performance targets detailed in Table 1.1.

1.2 Lithium batteries

The lithium-polymer battery was developed by Armand and co-workers at the end of the 1970's. A lithium anode was combined with an ion conducting polymer electrolyte and a lithium insertion host material cathode. While lithium is an ideal candidate for an anode material, as it has the lowest electrode potential of any element and is extremely lightweight, its use with an aqueous electrolyte causes obvious problems of reactivity. The cathode material in this type of battery is usually a transition metal oxide, into which lithium ions can be intercalated in a reversible fashion. A number of metal sulphides, such as TiS_2 (Whittingham 1976), have also been advanced as possible cathode materials.

The battery is constructed much like a 'complex sandwich', where the lithium anode, polymer electrolyte, metal oxide cathode, and current collecting material are bound together in layers. The cathode is usually a composite material containing the electrochemically active lithium-ion insertion compound and, if necessary, an electrical conductor, often a fine carbon powder, to improve the conducting properties of the transition metal oxide. The expansion / contraction of the cathode as lithium ions move in and out of the material can cause problems. In particular, this process can lead to a loss of electrical contact between the layer components of the solid-state cell. The problem is overcome by using a polymer binder in the cathode, which not only holds the

oxide and carbon particles together and facilitates lithium ion migration, but helps to absorb some of the volume changes as well.

Lithium metal does not make an ideal anode material as, not only is it highly reactive, but there are problems caused by the repetitive erosion and plating of the metal surface. This plating leads to dendrite formation and a loss of electrical contact between the anode and the rest of the battery components. In lithium-ion batteries these problems are overcome by using lithium-ion insertion materials for both electrodes, usually graphite or coke for the anode and a composite material for the cathode, which has already been described. In this type of cell, the lithium ions 'shuttle back and forth' between the electrodes, via the polymer electrolyte, which leads, not only to an increase in stability, but to an improvement of the cycling properties of the battery.

The local structure of the carbon material has an important effect on the amount of lithium that can be reversibly inserted (Flandrois 1999). Other insertion compounds, such as tin dioxide (Courtney 1997), are also being considered as anode materials. The main disadvantage of this type of cell is that the potentials that can be achieved are roughly 0.1 to 0.2V lower than those obtained using a lithium metal anode (Endo 2000), due to the relative stability of the lithium insertion material. Recently, tin oxides (Wolfenstine 1998) and lithium-tin alloys (Winter 1999) have also been used as anode materials as higher cell voltages are generated. A simple schematic of a lithium-ion cell is shown in Fig.1.2.

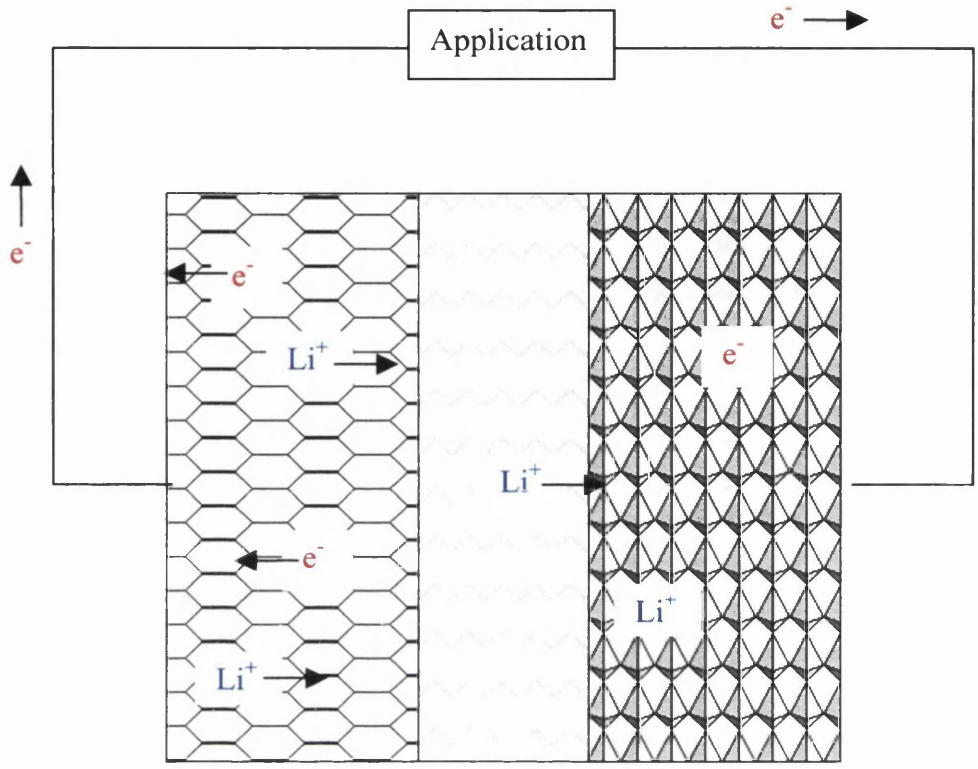

Fig.1.2. A lithium-ion battery cell under discharge.

Many of the ongoing problems with lithium-ion cells are related to the interface between the electrodes and the polymer electrolyte. Unwanted side-reactions, including phase changes, electrolyte decomposition, lithium metal deposition, and the irreversible intercalation of lithium ions all affect the performance of the cell, and, in particular, cause a loss of capacity during repeated cycling.

1.3 Cathode materials

This thesis will concentrate on a number of transition metal oxide materials that are promising candidates as the electrochemically active component in battery cathodes for solid-state lithium-ion batteries. This is an area of battery design that is undergoing constant development, with promising new materials appearing on a regular basis. Although the suitability of a wide range of oxides and sulphides, which are known to intercalate lithium ions, has been assessed experimentally, we apply a number of theoretical modelling techniques to this problem - methods that, until recently, have been underused in this area.

Transition metal oxides have proved to be the most promising family of materials for solid-state battery cathode materials and can be separated into two structural groups: layered materials and 3-dimensional lattices. Layered structures, such as V_2O_5 and MoO_3 contain 2-dimensional sheets of metal-oxygen polyhedra with weak interlayer bonding, which facilitates the insertion of lithium ions between the layers of the oxide. Lithium diffusion is often limited to a direction parallel to the layers. Three-dimensional structures must contain cavities that are large enough to incorporate Li^+ ions with good local co-ordination to oxygen. Diffusion of lithium ions often occurs along all three directions.

The scope of this thesis will include two vanadium oxides, V_2O_5 and V_6O_{13}, which have both been extensively studied experimentally, and a number of spinel phases with the general formula, $Li_xCo_yMn_{(4-y)}O_8$, which are promising new cathode materials of great

interest. Relevant experimental background has been included within the chapters that deal with each system in detail, although details of recent theoretical work on lithium-ion battery cathode materials are given in the next section.

Our study will concentrate on the structural changes that occur during lithium insertion, and the electronic rearrangement that is induced by the intercalated Li^+ ions, processes that determine the cell voltage produced by a given cathode material. The stabilities of a number of possible lithium sites within each material are compared, and the activation energies of lithium diffusion are also calculated. Comparison with experiment is made whenever data is available, which we consider to be an important aspect of our work. This thesis does not attempt to study the effects of repeated cycling on cathode structure, as this type of complex dynamic process is, at present, beyond the reach of the computational techniques employed here.

1.4 Previous Theoretical Studies

The application of theoretical methods, both interatomic potential based simulation and electronic structure calculations, to battery cathode materials is a relatively new development. The complexity of many cathode systems had prevented the use of computational simulation, in particular methods based on quantum theory, until recent increases in computer power. Now, *ab initio* methods can be used routinely to carry out a full geometry optimisation of periodic systems containing over forty atoms, making such methods a powerful tool for studying transition metal oxide systems.

Interatomic potential based simulation has been used successfully to model lithium intercalation into a number of systems, including the spinel Fe_3O_4 and the superconductor $YBa_2Cu_3O_7$ (Islam 1993), $NiMn_2O_4$ (Islam 1988), and lithium manganates (Ammundson 1997, 1998). These studies show that, given the use of good interatomic potentials, static lattice simulation can give useful information about the relative stabilities of lithium sites and the energetics of lithium migration.

Aydinol *et al* (Aydinol 1997a) showed that *ab initio* methods based on Density Functional Theory could be used successfully to predict the discharge voltage of a range of hypothetical transition metal oxides with the α-$NaFeO_2$-type structure. The same authors also stress the need to carry out full geometry optimisations when predicting discharge voltages, as local co-ordination of the lithium ions affects the band structure, and leads to differences of up to 0.5V in the calculated voltage. In the same year, Deiss *et al* (Deiss 1997) used DFT to calculate the average voltage, energy density, and specific energy of two anode-cathode couples, LiC_6/MoO_2 and LiC_6/NiO_2. Their results are in reasonable agreement with experimental values. The authors also show, by calculating the vibrational energies of each system, that temperature will have a minor effect on these values.

First-principles techniques have been used to investigate the ordering of lithium vacancies in the commercial cathode material, $LiCoO_2$, and to calculate successfully the discharge voltage and the thermodynamic stability of a number of phases in the same material (Wolverton 1998). Ceder *et al* used *ab initio* methods to show that doping $LiCoO_2$ with aluminium should increase the cell voltage, a proposition that is supported by the accompanying experimental results (Ceder 1998). The authors suggested that the

presence of aluminium increases the involvement of the oxygen atoms in accepting electron density during the lithium insertion reaction, and that as these oxygen states are lower in energy than the transition metal *d* states that are now no longer available, the resulting voltages are higher.

A number of spinel structures have also been studied recently using electronic structure methods, including $LiCoO_2$ (Van der Ven 1999), $LiTi_2O_4$ (Benco 1999), and $LiMnO_2$ (Aydinol 1997b). Van der Ven *et al* investigated the ordering of lithium on both the tetrahedral and octahedral sites within the spinel lattice, and calculated average cell voltages. Benco *et al* used *ab initio* and semiempirical methods to compare the stabilities of the spinel, $LiTi_2O_4$, with the trigonal phase, $LiTiO_2$. The spinel phase was found to be more stable, which is in agreement with experimental results. Finally, Aydinol *et al* predicted average open-circuit voltages in $Li_xMn_2O_4$, for x = 0.0 to 2.0, using first-principles calculations. Calculated voltages are in good agreement with experiment.

Chapter 2

Theoretical Methods

This study of solid-state battery cathode systems has used a variety of simulation methods to probe the atomic and electronic structure of these materials. Essentially, two levels of complexity have been used: classical interatomic potential based methods (often referred to as 'atomistic' modelling), and *ab initio* electronic structure techniques, which are far more computationally expensive. Our basic strategy has been to use atomistic calculations to learn about the basic behaviour of materials at the atomic level, then to probe the electronic structure of these materials with *ab initio* methods. Approaching the modelling in more than one way gives us confidence in our results and can lead to substantial savings in computer time.

2.1 Static Lattice Techniques

2.1.1 The Model

In the solid state many systems are made up of an extended lattice of atoms or ions. The interaction between these particles can be represented using the Born model of the solid, which approximates these interactions using simple potential functions. Calculation and minimisation of the lattice energy using these interatomic forces allows the total energy of the system and the most stable atomic arrangement to be found. This 'atomistic' approach been used with great success to model a wide range of solid state systems over the last twenty years. many examples can be found in the reviews of Catlow (1987, 1997).

2.1.1.1 Interatomic Potentials

All the ions in a cluster or an extended lattice experience a potential due to the other ions in the lattice. While, in practice, this potential is due to many complex interatomic interactions, its shape can be modelled using simple analytical functions relating the potential to the interatomic distances. The interatomic potential, V, of n interacting ions at co-ordinates r_i to r_n can be expressed as a series of many body terms:

$$V = V(r_i - r_n) = V_1 + \sum_{i,j=1, i\neq j}^{N} V_2(r_i, r_j) + \sum_{i,j,k=1, i\neq j\neq k}^{N} V_3(r_i, r_j, r_k) + \ldots + \sum_{i \quad n=1, i\neq j\neq k\ldots\neq n}^{N} V_n (r_1 \ldots r_n). \quad 2.1$$

The first term, V_1, is the formation or self energy of the non-interacting ions in the lattice. This is the energy needed to create the ions in the required electronic state. No attempt to calculate this term is made in most atomistic simulations; rather, it determines the zero of energy for the calculation. The subsequent terms in equation 2.1 are interaction energies involving two, three, and in principle, up to all atoms in the system. Taken together, these terms define the internal energy of the system. We note that the summations must be carried out for $i \neq j \neq k$ etc. to prevent the inclusion of terms in which the ions are interacting with themselves.

The number of terms that need to be included to represent the interatomic forces depends on the accuracy that is required. In ionic lattices, two-body terms by themselves usually give good estimates of lattice energies but cannot reproduce correctly all the elastic constants and phonon frequencies, even for classic ionic materials such as cubic MgO. Three-body interactions can often have a significant effect on the vibrational properties of the lattice and must be included for molecular systems. The primary focusof this work is the structure and relative stabilities of defects within the lattice, therefore energetics are of primary importance. Accordingly, only two-body interactions, where the function depends only on the magnitude of the interatomic spacing, have been calculated and these are defined as follows:

$$V_2(r_i, r_j) = \frac{q_i q_j}{4\pi\varepsilon_0 r_{ij}} + \phi(r_{ij}), \qquad 2.2$$

where $r_{ij} = |r_i - r_j|$. Essentially, this divides all two-body interactions into a Coulombic component and a short-range component, $\phi(r_{ij})$, which includes all other two-body

interactions such as van der Waals attraction, Pauli repulsion, and any elements of covalent bonding between atoms. It is this short-range term that is described using simple functions and is usually called a central force pair potential.

Many two-body functions are available, of which some, such as the harmonic or Morse potentials, are more suited to modelling bonded interactions. Others are best used for non-bonded interactions, and these include the widely used Lennard-Jones and Buckingham potentials. This work employs the Buckingham potential for most ionic interactions and the Morse potential for specific bonds where a degree of covalency is present.

The Buckingham potential has the following form:

$$\phi_{ij}(r_{ij}) = A_{ij} \exp\left(\frac{-r_{ij}}{\rho_{ij}}\right) - \frac{C_{ij}}{r_{ij}^{6}}, \qquad 2.3$$

where r_{ij} is the interatomic distance and A_{ij}, ρ_{ij}, and C_{ij} are all fitted parameters. The potential uses an exponential for the repulsive component and an r_{ij}^{-6} attractive term for dispersion effects, which can cause problems at very small values of r_{ij}, as r_{ij}^{-6} tends to negative infinity while the exponential term is finite. This effect causes ϕ_{ij} to tend to negative infinity for small r_{ij}, although it is not usually important as the repulsive barrier should be too large for interatomic distances to sample this part of the potential. We note that sometimes the Buckingham potential is used with $C_{ij} = 0$, making it purely repulsive.

The Morse potential is also used in the following form, where $\phi_{ij} = -D_0$ at the energy minimum:

$$\phi_{ij}(r) = D_0\left(\left\{1 - \exp\left[-\alpha_{ij}\left(r_{ij} - r_0\right)\right]\right\}^2 - 1 \right), \qquad 2.4$$

where D_0 is the dissociation energy of the bond, r_0 is usually equilibrium bond length, and α_{ij} is a fitted constant, related to the curvature of the minimum. This potential is best used when interatomic interactions are especially strong, as the potential well is often deep. It is often used when it is useful to relate the position of the potential minimum to the experimental bond length, and this is done by subtracting the Coulombic component of the interatomic interaction. The Morse potential is well behaved for small values of r_{ij}.

Potential parameters must be derived in some way, either through an empirical fitting process that compares calculated data to experimental properties, or by calculation of potential energy surfaces using simple 'electron gas' or more detailed quantum mechanical methods. These methods will be discussed in more detail later.

2.1.1.2 The Shell Model

The theoretical model that has been discussed so far describes the ion as a point charge. To model ionic solids adequately, especially if the lattice dynamics are to be calculated, some attempt at including ionic polarisation must be made. In particular, it is impossible to calculate the high frequency dielectric constant using a rigid ion model because the high frequency dielectric constant of the material, ε_∞, must be equal to unity, which, in

turn, makes it impossible to calculate the optical phonon modes correctly. Currently the most popular solution, which is used in this work, is the shell model developed by Dick and Overhauser (1958).

The shell model of ionic polarisability is a simple mechanical treatment in which an ion is split into two components: a core of charge q_{core}, which is coupled to a 'shell' of charge q_{shell}. The core contains all the mass of the ion; the shell is massless. There is no Coulombic interaction between the core and shell as this would generate a meaningless (and often infinite) energy term. Instead, the core and the centre of the shell are connected together by a harmonic spring with force constant k, which is a parameter of the model. This spring is the only interaction between the core and the shell. This is shown in the figure 2.1.

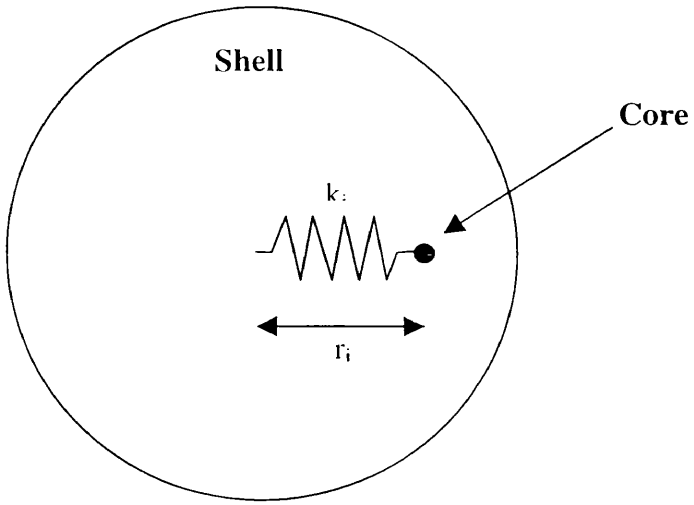

Fig. 2.1. Simple schematic of the shell model of ionic polarisability.

The total charge on the ion is:

$$q = q_{core} + q_{shell}, \qquad 2.5$$

and the interaction between the core and the shell is given by Hooke's Law:

$$\phi(r_i) = \frac{1}{2} k_i r_i^2. \qquad 2.6$$

The polarisability of the free ion in the shell model is given as:

$$\alpha_i = \frac{q_{shell}^2}{k_i}. \qquad 2.7$$

It is usual for q_{shell} to be negative, so that, roughly, the shell can be thought of as the valence electron cloud while the core is the nucleus and the core electrons of the ion. The important feature of this model is that short-range forces usually only act between the shells of the interacting species which, in contrast to the point polarisible ion (PPI) model, couple the ionic polarisation to these forces. This coupling stops the overall polarisation within the lattice being overestimated (Catlow 1982a) or, in some cases, the system collapsing during the energy minimisation.

2.1.1.3 Derivation Of Interatomic Potential Parameters.

Although atomistic modelling is now well established as a useful tool in computational chemistry and libraries of potentials are available for modelling a wide range of systems, it is still necessary to derive new potentials before modelling a number of materials, including some transition metal oxides. There are essentially two approaches to the evaluation of potential parameters; either empirical methods that rely on fitting potentials to experimental data, or theoretical methods whereby potentials are obtained fitting functions to various types of quantum mechanical calculations. All the parameters that are derived in this work have been obtained empirically by fitting to crystal structure data and dielectric constants. Empirical methods will, therefore, be described in greater detail, while only a brief summary of the theoretical methods available will be given. Further details of the fitting methods used can be found in Gale (1996).

Empirical fitting of the Buckingham potential parameters, A_{ij}, ρ_{ij}, and C_{ij}, uses experimental data such as the crystal structure, dielectric, elastic and piezoelectric constants, and phonon frequencies within a least-squares minimisation routine. The main drawback of empirical fitting is that experimental data tends to be concentrated over a very small region of the potential energy surface, close to the equilibrium bond lengths, which can make empirically derived potentials unreliable when modelling systems under high pressure or with interstitial or vacancy defects. This problem is particularly pronounced if the symmetry of the system is high, so that the number of

inequivalent bonds is likely to be low. Fitting simultaneously to more than one crystal structure can help to overcome the difficulty.

There are a number of schemes available to fit potentials to experimental data. The fastest method is, for a given set of potentials, to calculate the forces on all the atoms and the properties of the crystal structure, and then, by changing the potential parameters, to minimise the forces while reproducing the crystal properties. This works well even though an approximation has to be used when properties are required. These must be calculated using the experimental structure but with the first derivative of the lattice energy with respect to the atomic co-ordinates being non-zero, as no optimised structure is available. The shell model can be incorporated into this fitting scheme by including the shell positions in the list of variables, along with the interatomic potential parameters. The shell positions can then be varied during the fitting scheme so that the forces on the shells are minimised, which improves the predicted crystal properties.

An alternative fitting method, employed for the majority of the work in this thesis, carries out a structural optimisation, using the current potential parameters, during each cycle of the fitting procedure. The interatomic potential parameters are derived by comparing the calculated structure and properties to experimental values, within a least-squares minimisation scheme. This method treats the shells explicitly, and properties can be calculated accurately using the optimised structure, but it is considerably more computationally expensive. Along with the increased cost of the calculation, it is important to begin with a robust potential model, i.e. one that will lead to a valid optimisation of the atomic structure and gives a sensible local curvature of the potential

energy surface. It is often advisable to use this method to improve a potential that has already been derived using the previous fitting scheme.

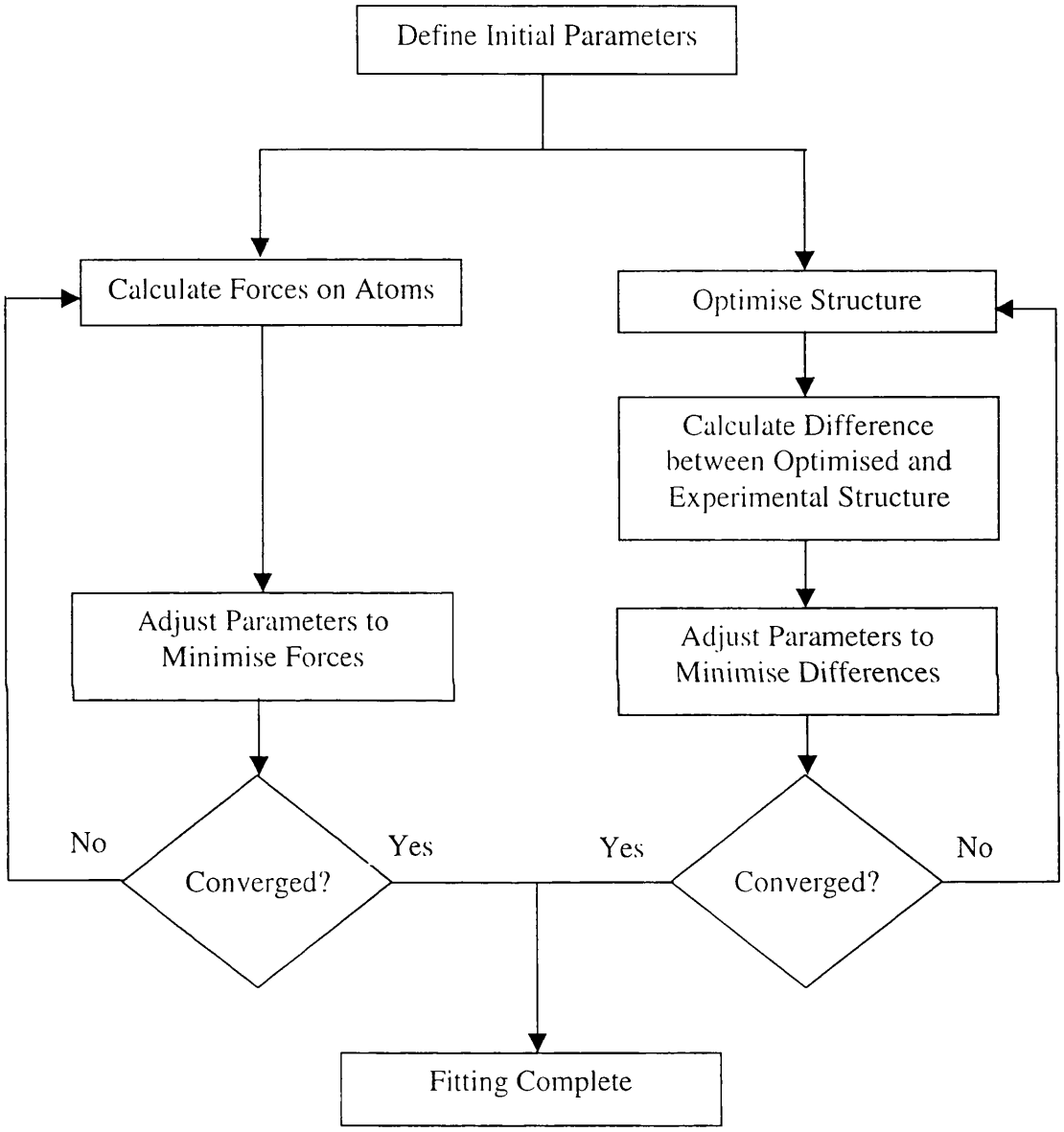

Fig. 2.2. Interatomic potential fitting schemes within the GULP code.

Theoretical quantum mechanical methods are also available for potential fitting and have the advantage that they can be used to develop potential models for systems where there is insufficient experimental data for empirical fitting. *Ab-initio* hyper-surface fitting uses data from quantum mechanical calculations on periodic or cluster systems to build up a detailed description of the potential energy surface around each atom. This is

achieved by calculating the binding energy for a number of atomic configurations and then fitting this data to a specified functional form. This type of fitting can lead to potentials that are highly transferable, as the calculated energy surface contains information about the interatomic interactions for a wide range of distances.

The electron-gas method, developed by Wedepohl in 1967 and later by Gordon and Kim (1972), can be used to derive potentials by calculating the interaction between the electron densities on the interacting species. The electron densities on the isolated ions may be calculated by using a local potential function. This should contain the Madelung term but may also include the effect of orthogonalisation to the wavefunction of the surrounding ions. The total electron density can be approximated as the sum of the individual electron densities of the interacting species. The total energy of interaction of two ions can then be calculated as:

$$\Phi_{ij}(r_{ij}) = E_{NUC} + E_{COUL} + E_{EXCH} + E_{KIN} + E_{CORR}, \qquad 2.8$$

where the terms are the internuclear repulsions, the Coulombic interactions, and the exchange, kinetic and correlation energies respectively. The last three terms are approximated by the electron gas method using functionals. It is not possible to include a description of dispersion effects in the interaction energy.

While the method involves several approximations, it leads to potentials that are compatible and transferable, as long as the Madelung well used to simulate the bulk lattice is consistent. They can be used successfully for both bulk and defect calculations.

It is also possible to calculate ion pair interactions directly using Hartree-Fock methods (Fowler 1983).

2.1.1.4 Electrostatic Interactions

The Coulombic interactions arise, of course, from the electrostatic interactions between ions, and the total Coulombic energy in atomic units can be written as:

$$E = \sum_{i<j} \frac{q_i q_j}{r_{ij}}. \qquad 2.9$$

This term corresponds to the monopole - monopole interactions and neglects all higher-order terms, and therefore works well for systems that contain spherical ions. Real systems are unlikely to have such an isotropic charge distribution, due to covalent contributions to the bonding or other distortions, such as the Jahn - Teller effect. Instead of trying to calculate higher terms, such as dipole-dipole interactions directly, approximations such as the shell model and Distributed Multipole Analysis, DMA. (Stone 1985) are used to represent non-spherical charge distributions. In this way the Coulombic contribution can be calculated more accurately.

This contribution is simple to calculate for an isolated cluster of ions but for a system, made up of an infinite, periodic, three-dimensional lattice, it is difficult. The difficulty is due to the long-range nature of the Coulombic interaction and the rapidly increasing number of interacting species, as the cutoff distance increases. This is demonstrated by the Madelung sum for a cubic lattice like NaCl):

$$E = \frac{q_i}{4\pi\varepsilon_0}\left\{-\frac{6q_j}{r_{ij}} + \frac{12q_k}{\sqrt{2}r_{ik}} - \frac{8q_l}{\sqrt{3}r_{il}} + \frac{6q_m}{\sqrt{4}r_{im}} \ldots\ldots\ldots\right\}. \qquad 2.10$$

The total summation is conditionally convergent; therefore, direct summation of this series is an unreliable procedure.

This problem is overcome by using a technique developed by Ewald (1921), in which the calculation is split into two parts, one in real space, and the other in reciprocal space. Briefly, the Laplace transform is used to express r^{-1} as the integral:

$$\frac{1}{r} = \frac{2}{\pi^{1/2}}\int_0^\infty \exp\left(-r^2t^2\right)dt, \qquad 2.11$$

where t is a variable. This identity can be split into two terms at an arbitrary point η:

$$\frac{1}{r} = \frac{2}{\pi^{1/2}}\int_0^\eta \exp\left(-r^2t^2\right)dt + \frac{2}{\pi^{1/2}}\int_\eta^\infty \exp\left(-r^2t^2\right)dt. \qquad 2.12$$

The first term (from 0 to η) is solved by transformation into reciprocal space by Fourier analysis, to give:

$$\frac{2}{\pi^{1/2}}\int_0^\eta \exp\left(-r^2t^2\right)dt = \frac{4\pi}{V}\sum_{\underline{G}}\frac{1}{G^2}\exp\left(\frac{-G^2}{4\eta}\right)\exp\left(-i\underline{\mathbf{G}}.\underline{\mathbf{r}}\right), \qquad 2.13$$

where $\underline{\mathbf{G}}$ is a reciprocal lattice vector and V is the volume of the unit cell. The second term in equation 2.12 is evaluated in real space as follows:

$$\frac{2}{\pi^{1/2}}\int_{\eta}^{\infty}\exp\left(-r^2t^2\right)dt = \frac{1}{r}\mathrm{erfc}(\eta r), \qquad 2.14$$

where erfc(ηr) is the complementary error function:

$$\mathrm{erfc}(n) = 1 - \mathrm{erf}(n). \qquad 2.15$$

The value of η determines the balance between the amount of the calculation performed in real and reciprocal space and is crucial in determining the speed of convergence of the summation.

2.1.2 The Calculation

The General Utility Lattice Program, or GULP (Gale 1997, Woodley 1999) has been used for all of the atomistic work in this thesis. GULP was developed by J.D. Gale, at the Royal Institution and Imperial College, London, and can be used to carry out static lattice simulations for both bulk and defect calculations: these will be discussed in detail in the following section. The lattice energy, a range of physical properties, bond lengths, and phonon frequencies can be calculated for the optimised geometry. GULP has also been used to fit new potentials to experimental data.

2.1.2.1 Energy Minimisation

Once a potential model of a system such as an ionic lattice has been set up then the potential energy of the lattice can be calculated with respect to the atomic positions within the lattice. Coulombic and short-range interactions produce forces on each ion in the lattice, and the energy minimum may be calculated by reducing these forces to zero. For a system of N atoms acted on by a force, F_i at position. r_i, the energy minimum is found when:

$$F_i = 0, \text{ for } i = 1,N. \qquad 2.16$$

Let us consider the procedure of energy minimisation in greater detail. A fruitful approach is to use a Taylor series expansion of the energy function around an initial atomic configuration, $\underline{\mathbf{r}}$.

$$f(\underline{\mathbf{r}} + \delta) = f(\underline{\mathbf{r}}) + f'(\underline{\mathbf{r}}).\delta + \frac{1}{2} f''(\underline{\mathbf{r}}).\delta^2 + \ldots\ldots, \qquad 2.17$$

where δ represents a small change in $\underline{\mathbf{r}}$. As δ is small, higher terms tend to zero and can be ignored. Sampling points on the surface, which represents calculating the first term in the Taylor series, is computational cheap but, even if the sampling is done in a systematic manner such as the downhill simplex method (Nelder 1965), very inefficient. Using first and even second derivatives, to give information about the shape of the surface, reduces the number of cycles needed to reach convergence, as the direction in

which the minimum lies can now be estimated. Three methods of energy minimisation are outlined below.

The most basic way of using first derivative information is called steepest descent minimisation, where the new positions are predicted using the gradient vector from the current geometry. Therefore, if, for each n^{th} cycle, the first derivative of the lattice energy with respect to all the positional variables, $\underline{\mathbf{X}}^{(n)}$, is:

$$\mathbf{g}^{(n)} = \frac{\partial E}{\partial \underline{\mathbf{X}}^{(n)}}, \qquad 2.18$$

and the displacement vector for the n^{th} cycle, $\underline{\mathbf{s}}$, is defined as:

$$\underline{\mathbf{s}}^{(n)} = -\mathbf{g}^{(n)}, \qquad 2.19$$

then the positions are updated as follows:

$$\underline{\mathbf{x}}^{(n+1)} = \underline{\mathbf{x}}^{(n)} + C^{(n)}\underline{\mathbf{s}}^{(n)}, \qquad 2.20$$

where $C^{(n)}$ is a constant which is altered to optimise the speed of convergence of the calculation.

The steepest descent method is usually very robust but can become very inefficient under certain circumstances. If the potential energy surface contains a long valley that leads down to the minimum then this method can 'bounce' from one side of the valley

to the other, leading to very slow convergence. This happens because the direction of 'steepest decent' across the potential energy surface is rarely the direction in which the minimum lies.

The conjugate gradient method uses first derivatives from the present and previous iterations to calculate the next changes in atomic positions, which usually leads to a speed up in convergence as the minimiser uses information about the route already taken to calculate the direction of the next step. This overcomes the problem outlined in the previous paragraph. The displacement vector, $\underline{\mathbf{s}}^{(n)}$, now becomes:

$$\underline{\mathbf{s}}^{(n)} = -\mathbf{g}^{(n)} + \underline{\beta}^{(n)}\underline{\mathbf{s}}^{(n-1)}, \qquad 2.21$$

where:

$$\underline{\beta}^{(n)} = \frac{\mathbf{g}^{T(n-1)}.\mathbf{g}^{(n-1)}}{\mathbf{g}^{T(n-2)}.\mathbf{g}^{(n-2)}}. \qquad 2.22$$

Although the conjugate gradient method is usually stable, it is possible for $\mathbf{g}^{(n)}$ to become too dependent on $\mathbf{g}^{(n-1)}$ over a large number of iterations, at which point the minimisation will break down. This possibility is often overcome by repeatedly switching to steepest decent methods for a small number of iterations during the minimisation procedure, which ensures that the search direction calculated correctly.

The last minimisation method that will be discussed uses second derivative information to further reduce the number of iterations required for convergence. In the Newton-

Raphson method the second derivative information is often referred to as the Hessian and is stored in a matrix, $\underline{\mathbf{W}}$, so that

$$\underline{\mathbf{W}} = \frac{\partial^2 E}{\partial \underline{\mathbf{x}}^2} . \qquad 2.23$$

The first three terms of the Taylor expansion for the energy, $\underline{\mathbf{x}}^{(n)}$, $\mathbf{g}^{(n)}$, and $\underline{\mathbf{H}}^{(n)}$ respectively, are now included in the search algorithm. The updating scheme for $\underline{\mathbf{x}}$ becomes:

$$\underline{\mathbf{x}}^{(n+1)} = \underline{\mathbf{x}}^{(n)} - \alpha \underline{\mathbf{H}}^{(n)} . \mathbf{g}^{(n)}, \qquad 2.24$$

where α is a scaling coefficient and $\underline{\mathbf{H}}$ is the inverse of the second derivative matrix, $\underline{\mathbf{W}}$:

$$\underline{\mathbf{H}} = \underline{\mathbf{W}}^{-1}. \qquad 2.25$$

An increase in the overall speed of the calculation does not usually result from the basic Newton scheme because calculation and inversion of the second derivative matrix or Hessian during each iteration is very computationally expensive, especially for large systems. Another problem with using second derivatives is that the matrix must be stored in an array that requires a lot of memory for large systems. $\underline{\mathbf{H}}$ has $(3N)^2$ elements (where N is the number of atoms), although just over half, 1/2[3N(3N+1)], of these elements are actually needed because of the symmetry of the matrix.

As the calculation of $\underline{\mathbf{H}}$ during each cycle is computationally expensive, it is now common to use some kind of updating method that uses first derivative information to estimate the second derivative matrix for the next iteration. One of the first applications of this method was by Davidon (1959), and Fletcher and Powell (1963). The Hessian matrix is usually recalculated exactly at regular intervals so that errors do not become too large. This type of *quasi*-Newton method is used in GULP; the Hessian is updated using the BFGS method, due to Broyden, Fletcher, Goldfarb, and Shanno (Press 1992) and is usually recalculated exactly every 10 cycles, unless errors become significant before then.

2.1.2.2 Perfect Lattice Optimisation

In the GULP code, energy minimisation of a periodic ionic lattice is achieved using the Ewald summation of the Coulombic terms, and a direct summation of the short range terms, within a *quasi*-Newton optimisation scheme. Periodic boundary condition are used to simulate an infinite lattice in three dimensions. Unit cell dimensions, as well as ionic positions, can be optimised. Properties, such as dielectric and elastic constants, are calculated from the second derivatives of the energy with respect to the internal and external strains on the lattice.

2.1.2.3 Defect Optimisation

The energy required to create a lattice defect is given by:

$$E_{DEFECT} = E_{DEFECTIVE\ LATTICE} - E_{PERFECT\ LATTICE}. \qquad 2.26$$

Calculating the energy of a defective lattice requires a method of reproducing a configuration of defects in an infinite lattice. Modelling an isolated defect breaks the periodic boundary conditions, so some form of approximation has to be used. There are two main methods available: the supercell method and the Mott-Littleton approximation.

It is possible to model a lattice defect with an array of defects using periodic boundary conditions, if the defect separation is large enough. This is done by using a supercell made up of a number of unit cells of the original bulk material and containing a single defect site. The size of the supercell is crucial and must be large enough so that the energy associated with any interaction between the defect and its closest image is small - a requirement which can lead to large simulation cells and, therefore, costly calculations. Charged defects can also be modelled in this way: either a compensating background charge must be used through out the supercell, so that the total charge on the system is zero, or charge compensating defects must be introduced explicitly.

An alternative scheme, which avoids the problems associated with the use supercells, was developed from the continuum theories of Mott and Littleton (1938) and developed by Lidiard and Norgett (1972), and has been used in this work to model all point defects. It splits the space around the defect centre into spherical regions, with the defect at the centre. Neutral defects can be treated with two regions. The atoms within the inner region, region I, which includes the defect itself, are treated explicitly, meaning that a full atomistic optimisation is performed. In region II, which extends to infinity, the polarisation energy is calculated using a quasi-continuum approximation: i.e. the

energy associated with the perturbation of region II, due to the atomic movement within region I, is included by calculating the forces on the atoms, and then approximating their displacements from the perfect lattice positions as harmonic. This is a good approximation assuming that region I is large enough, so that the perturbations on region II are small.

The defect energy can now be defined in terms of the atomic co-ordinates of region I, $\underline{\mathbf{r}}_1$, and the displacements within region II, $\delta\underline{\mathbf{r}}_2$:

$$E_{DEFECT} = E_1(\underline{\mathbf{r}}_1) + E_{12}(\underline{\mathbf{r}}_1, \delta\underline{\mathbf{r}}_2) + E_2(\delta\underline{\mathbf{r}}_2), \qquad 2.27$$

where the terms are, respectively, the energy of region I, the interaction energy between the regions, and the energy of region II. As we have assumed harmonic displacements, $\delta\underline{\mathbf{r}}_2$, within region II, E_2 can be expressed as a quadratic function of $\delta\underline{\mathbf{r}}_2$:

$$E_2(\delta\underline{\mathbf{r}}_2) = \frac{1}{2}(\delta\underline{\mathbf{r}}_2.\underline{\mathbf{A}}.\delta\underline{\mathbf{r}}_2), \qquad 2.28$$

where $\underline{\mathbf{A}}$ is a force constant matrix. Assuming that $\delta\underline{\mathbf{r}}_2$ satisfies the equilibrium condition that:

$$\left(\frac{\partial E}{\partial(\delta\underline{\mathbf{r}}_2^0)}\right)_x = 0, \qquad 2.29$$

then we can substitute the above expression into equation 2.27 to give:

$$\left(\frac{dE_{DEFECT}}{d\delta\underline{\mathbf{r}}_2}\right)_0 = \left(\frac{dE_{12}\left(\underline{\mathbf{r}}_1, \delta\underline{\mathbf{r}}_2^0\right)}{d\delta\underline{\mathbf{r}}_2}\right) + \underline{\mathbf{A}}.\delta\underline{\mathbf{r}}_2^0 = 0. \qquad 2.30$$

From the above and equation 2.28, we can write a new expression for E_2:

$$E_2(\delta\underline{\mathbf{r}}_2) = -\frac{1}{2}\delta\underline{\mathbf{r}}_2\left(\frac{dE_{12}\left(\underline{\mathbf{r}}_1, \delta\underline{\mathbf{r}}_2^0\right)}{d\delta\underline{\mathbf{r}}_2}\right). \qquad 2.31$$

Substitution of the above formula into our original expression for the defect energy (equation 2.27) allows us to eliminate the dependence of the defect energy on the energy of region II:

$$E_{DEFECT} = E_1(\underline{\mathbf{r}}_1) + E_{12}(\underline{\mathbf{r}}_1, \delta\underline{\mathbf{r}}_2) - \frac{1}{2}\left(\frac{dE_{12}\left(\underline{\mathbf{r}}_1, \delta\underline{\mathbf{r}}_2^0\right)}{d\delta\underline{\mathbf{r}}_2}\right)\delta\underline{\mathbf{r}}_2. \qquad 2.32$$

It is possible to evaluate the terms in the above expression with the same techniques used for the perfect lattice. The starting positions for the atoms within region I are usually given by a preceding energy minimisation of the perfect lattice.

Charged defects can be treated in a similar way but, in this case, region II is split into two sections, IIa and IIb, which are shown in the Fig. 2.3.

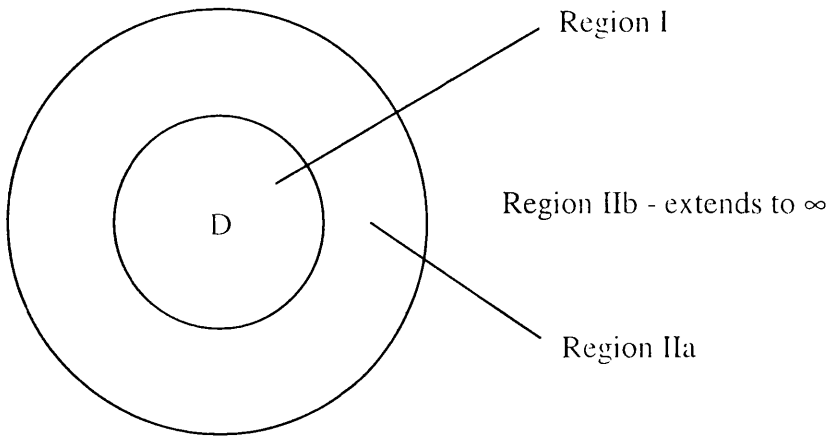

Fig. 2.3. A schematic representation of the Mott-Littleton method; D denotes the defect centre.

The atoms in region IIa are relaxed harmonically around their perfect lattice positions as before, while region IIb, which extends to infinity, is treated as a dielectric continuum and only responds to the total charge of the defect, Q. The polarisation of the region IIb continuum, P_c, due to a charge, Q, at distance, $\underline{\mathbf{r}}$, can be calculated from the classical polarisation theory of Mott and Littleton:

$$P_c = \frac{V}{4\pi}\left(1 - \frac{1}{\varepsilon_0}\right)\frac{Q\underline{\mathbf{r}}}{r^3}, \qquad 2.33$$

where ε_0 is the static dielectric constant of the continuum and V is the volume of the unit cell. The situation is more complex in materials where the dielectric response is not isotropic, but the basic approach is the same (Catlow 1982b). The polarisation of the continuum, P_c, can be used to calculate the harmonic displacements of the ions in region IIb at all distances, from the defect centre out to infinity.

The interaction energy between region I and the region IIb continuum, E_{12b}, can be approximated as follows:

$$E_{12b} = -\frac{Q^2}{2}\sum_{j\in IIb} q_j \frac{M_j}{\underline{r}_j^4}, \qquad 2.34$$

where Q is the charge on the defect and the summation is taken over the whole of region IIb. M_j is the Mott-Littleton parameter for the ionic lattice and is given by:

$$M_j = \frac{\alpha_j}{\sum_k \alpha_k}\left(1-\frac{1}{\varepsilon_0}\right), \qquad 2.35$$

where α_j is the polarisability of the j^{th} ion in region IIb. Minimisation techniques, such as the *quasi*-Newton scheme already described, can be applied to this formulation to give the optimised atomic positions in region I and the defect energy.

This approximation works well, although it assumes that any atomic rearrangement of the lattice due to the defect is included within region I. Therefore, an appropriate choice of the radius of region I is crucial to the success of the calculation and should be made so that the calculated defect energy is convergent with increasing region I size. Modern defect calculations often use a region I that contains around 400-500 atoms (Harding 1989, Sim 1989, Grimes 1990, Pavlides 1994, Williford 2000).

2.2 Electronic Structure Techniques

It has long been realised that an exact solution to Schrödinger's equation would lead to a complete understanding of atomic structure and properties on a fundamental level. Although this still proves impossible for systems more complex than the hydrogen atom, various methods have been devised which allow self-consistent, approximate, but increasingly accurate, solutions to be found. As computational power has increased it has been recognised that these methods could be used to calculate the electronic wavefunction in ever more complex materials and that these techniques would have an important rôle to play in all areas of physical and chemical research.

To move beyond the simple potential model already described in the first half of this chapter, it is necessary to include electrons explicitly, which allows us to study simple materials in greater depth and also simulate more complex materials where an interatomic potential treatment is unsatisfactory. Calculating the electronic structure of a material is a difficult problem because of the subtle ways in which electrons interact with each other. Particular difficulty has been encountered when attempting to calculate the energy contributions relating to electron correlation and exchange. There are now two main ways of approximating the solution to Schrödinger's equation, Hartree Fock methods and Density Functional Theory or DFT. It is the second method that has been used for all the electronic structure calculations in this thesis because it results in calculations which require significantly fewer resources when modelling the type of periodic system which is of interest here.

2.2.1 The Basics Of Density Functional Theory

In 1964 Hohenburg and Kohn proved that the ground state energy of a system can be expressed as a unique functional of the electron density of the system. For a given electronic density distribution, $\rho(r)$, there is a single value for the energy. Very simply, $E = E(\rho)$.

Using the Born-Oppenheimer approximation, which separates electronic and nuclear motions, the energy of a system of atoms can be divided into a number of components, as follows:

$$E = E_N + E_H + E_K + E_{xc}, \qquad 2.36$$

where the terms correspond to the Coulombic interaction with the nuclei in the system, the Hartree approximation of the Coulombic electron electron interactions, the kinetic energy of the electrons, and the exchange-correlation term respectively. Now, if the potential due to the nuclei in the system is defined as $V_c(r)$ then:

$$E(\rho) = \int V_c(r)\rho(r).dr + F(\rho), \qquad 2.37$$

where $F(\rho)$ gives the kinetic energy of the electrons and all the interelectron interactions.

$$F(\rho) = E_K(\rho) + E_H(\rho) + E_{xc}(\rho). \qquad 2.38$$

We can define E_H as the Coulombic interaction of a system of non-interacting electrons, known as the Hartree energy:

$$E_H = \frac{1}{2} e^2 \int \frac{\rho(r)\rho(r')}{|r - r'|} .dr.dr', \qquad 2.39$$

where E_K, is the kinetic energy of a system of non-interacting electrons with density $\rho(r)$. The other terms in $F(\rho)$ cannot be defined exactly at this point. The exchange-correlation term, E_{xc}, includes all other contributions to the energy that have been omitted from E_H and E_K. This is the key difference between DFT and Hartree-Fock methods, where the electron exchange is calculated exactly and only the correlation term is excluded.

2.2.2 The Local Density Approximation

Now that we have an exact expression for the energy of the system in terms of the electron density of the system, $\rho(r)$, we come to the first important approximation at the heart of density functional theory when used in practice, the local density approximation, LDA (Gunnarsson 1976, Perdew 1981). The local density approximation is concerned with finding a way to deal with the rather loosely defined exchange-correlation term, E_{xc}.

We know exactly the value of E_{xc} for a uniform electron gas from a number of methods, such as many-body perturbation theory (Hedin 1972) and quantum Monte-Carlo calculations (Ceperley 1980). Therefore, the exchange-correlation energy per electron,

$\varepsilon_{xc}(\rho)$, has been accurately estimated and is expressed as an analytical function of the electron density. The LDA states that E_{xc} at any point only depends on the electron density, $\rho(r)$, at that point, which is the same as the case of a uniform electron gas. In other words, E_{xc} is a local function of $\rho(r)$. Therefore, we can write E_{xc} as:

$$E_{xc} = \int \rho(r)\varepsilon_{xc}(\rho(r)).dr\,, \qquad 2.40$$

since $\rho\varepsilon_{xc}(\rho)$ is the density of the exchange-correlation energy in the uniform electron gas.

This may seem rather drastic, as we are suggesting that the exchange-correlation energy does not dependent on the shape of the electron density distribution, but only on the value at a given point. Although the LDA is surprisingly successful it has been found systematically to overestimate binding energies in a wide range of systems, often by as much as 50% (Weinert 1982). New methods have been introduced which try to correct this inadequacy by trying to take account of the way in which the charge density distribution changes in space.

2.2.2.1 The Generalised Gradient Approximation

The generalised gradient approximation, GGA, uses the gradient of the electron density to try to correct the errors that result from the LDA. Simply, GGA (Perdew 1992, White 1994) can be expressed as:

$$E_{xc}^{GGA} = E_{xc}^{LDA} + E_x(\rho'(r)) + E_c(\rho'(r)), \qquad 2.41$$

where the last two terms on the right hand side are corrections to the exchange and correlation energies respectively, which depend on the first derivative of the electron density, ρ'(r). Perdew(1986) and Becke(1988) among others have both proposed functional forms for these 'non-local' corrections terms.

2.2.2.2 Spin Polarisation

Up to this point there has been no discussion of electron spin and how to deal with systems which contain unpaired electrons. Many systems that are of interest will contain an uneven number of electrons or include atoms with magnetic moments, so a method to treat spin polarisation is needed.

The LDA scheme has been generalised to include electron spin by defining the exchange-correlation energy in terms of the electron density, ρ(r), and the spin density, σ(r), where

$$\sigma(r) = \rho_\uparrow(r) - \rho_\downarrow(r), \qquad 2.42$$

while

$$\rho(r) = \rho_\uparrow(r) + \rho_\downarrow(r). \qquad 2.43$$

The spin density is defined as the difference between the density of electrons with spin-up and electrons with spin-down. The dependence of the exchange-correlation term now means that it is possible to model anti-ferromagnetic materials correctly, as atoms with identical electronic populations but opposite magnetic moments can be differentiated. The anti-parallel alignment of the electron spins means that the spin density changes rapidly through space, which makes an important contribution to the calculation of $E_{xc}(\rho)$.

2.2.3 The Kohn-Sham Equations

If we return to our simple expression for the ground state energy:

$$E(\rho) = \int V_c(r)\rho(r).dr + E_K(\rho) + E_H(\rho) + E_{xc}(\rho), \qquad 2.44$$

we can use the variational principle to find the ground-state energy for a system of apparently independent electrons by minimising $E(\rho)$ with respect to $\rho(r)$. When $E(\rho)$ is at a minimum it will be stationary with respect to changes in $\rho(r)$:

$$\frac{\delta E(\rho)}{\delta \rho(r)} = 0. \qquad 2.45$$

Given that the number of electrons in the system, N, is constant then for a small change, $\delta\rho(r)$,

$$0 = \delta E - \mu \delta N, \qquad 2.46$$

where μ is the associated Lagrange multiplier, identified as the chemical potential of the electrons. This gives:

$$0 = \int V_c(r)\rho(r).dr + E_K(\rho) + e^2 \int \frac{\delta\rho(r)\rho(r')}{|r-r'|}.dr.dr' + \int \delta\rho(r)\mu_{xc}(\rho(r)).dr - \mu \int \delta\rho(r).dr, \quad 2.47$$

where:

$$\mu_{xc}(\rho) = \frac{d}{d\rho}(\rho\varepsilon_{xc}(\rho)). \quad 2.48$$

The condition above can be rewritten as:

$$0 = \int (V_{eff}(r) - \mu)\delta\rho(r).dr + \delta E_K, \quad 2.49$$

where:

$$V_{eff} = V_c(r) + e^2 \int \frac{\rho(r')}{|r-r'|}.dr' + \mu_{xc}(\rho(r)). \quad 2.50$$

This is exactly the condition for the ground-state energy of a system of non-interacting electrons acted on by the external potential, V_{eff}. The important result from this is that the ground state energy of a system of *interacting* electrons in the nuclear potential, $V_c(r)$, is equal to the ground state energy of a system of *non-interacting* electrons in

potential V_{eff}. If the electrons do not interact then the terms that depend on electron interactions disappear from the above equation, to leave:

$$V_c(r) = V_{eff}(r). \qquad 2.51$$

This similarity between a system of interacting and non-interacting electrons can be exploited because it is possible to solve the Schrödinger equation for a system of non-interacting particles. This was given by Kohn and Sham (1965) as:

$$\left[-\frac{h^2}{2m}\nabla^2 + V_{eff}(r)\right]\Psi_i(r) = \varepsilon_i\Psi_i(r). \qquad 2.52$$

The possible solutions, Ψ_i, are the single electron orbital wavefunctions while the corresponding eigenvalues, ε_i, give the orbital energies. The electron density distribution can now be expressed as:

$$\rho(r) = \sum_i |\Psi_i(r)|^2. \qquad 2.53$$

The summation is carried out over all occupied states.

It can now be seen that there is an interdependence of the potential, V_{eff}, and the electron density distribution, $\rho(r)$: V_{eff} includes electron-electron interactions and is therefore dependent on $\rho(r)$. The electronic wavefunctions, Ψ_i, are calculated using V_{eff},

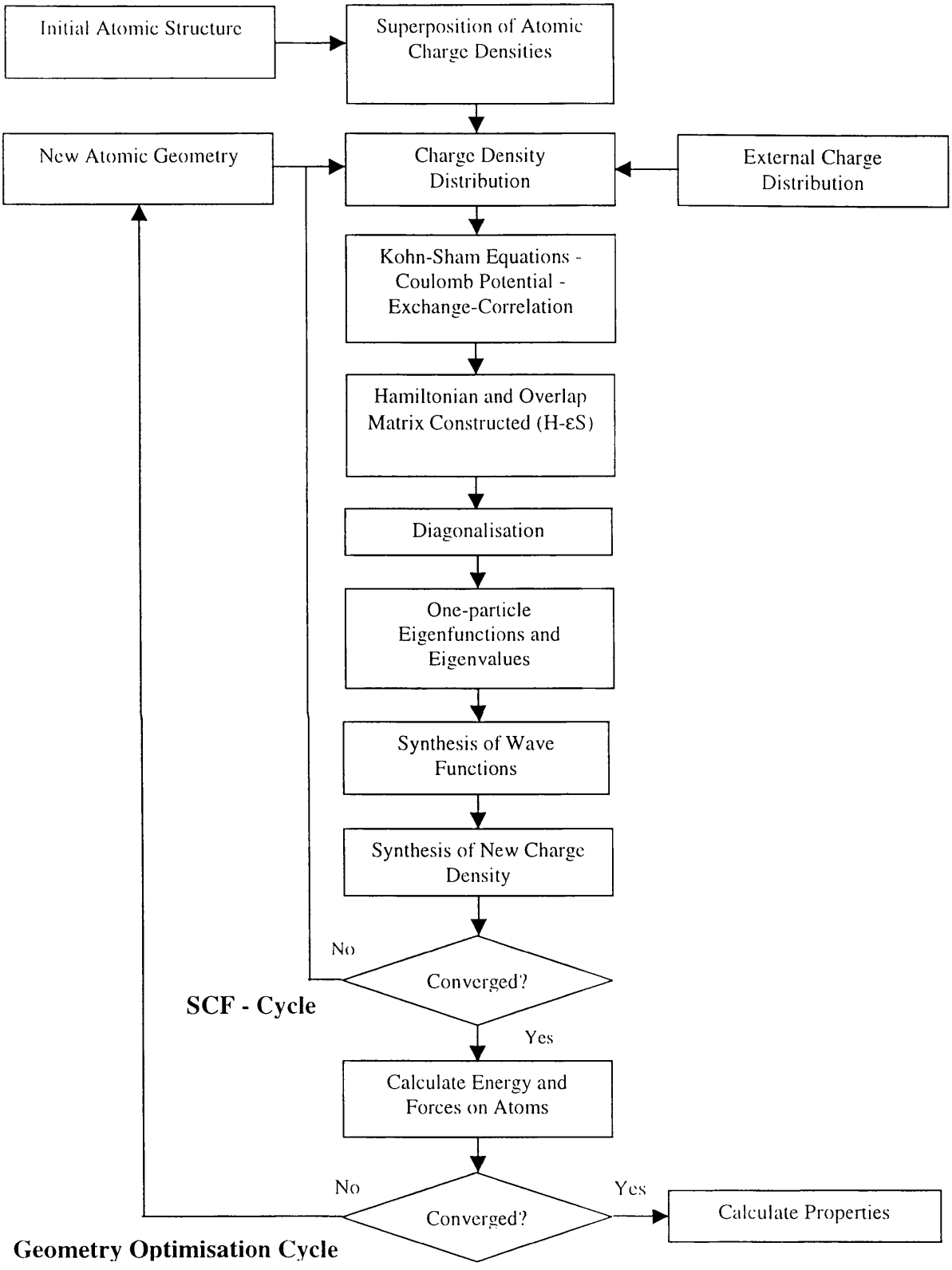

Fig. 2.4. Optimisation scheme used in the electronic structure calculations.

and $\rho(r)$ is calculated as the sum of Ψ_i. Therefore, the solutions, Ψ_i, to the Kohn-Sham equation can only be found in a self-consistent manner, described schematically in Fig. 2.4.

2.2.4 The Method

All the calculations in this thesis have been carried out using the plane wave - pseudopotential method, which uses a plane wave basis set to model the valence electrons while the atomic nuclei and the core electrons are represented together using a potential function known as a pseudopotential. The reasoning to support the choice of this method, and the way pseudopotentials are derived, are now outlined.

2.2.4.1 Planewaves

It has long been recognised that it is the valence electrons of the system that determine the bonding of the atoms within a material. The core electrons, which are tightly held to the nucleus, are hardly affected by the environment around the atom and only determine the potential experienced by the valence electrons. It is, therefore, the valence electrons, acting within the combined potential of the nuclei and the core electrons, which we wish to model in detail.

For a free electron, the eigenfunctions that determine the electronic wavefunctions are planewaves (Gillan 1991). It has also been shown that valence electrons apparently have similar properties to free electrons, as band structures calculated from the free-electron

approximation (Sutton 1993) are very similar to the real band structures in many materials. Since valence electrons are shielded from the strong nuclear potential by the core states, planewaves have been proposed as an efficient way of representing them, as long as the effective potential acting on the electrons is weak. This weak potential is provided by the use of pseudopotentials. Core electrons, on the other hand, do experience the strongly attractive potential due to the atomic nuclei which causes them to oscillate extremely rapidly. These rapid oscillations reflect the high kinetic energies of electrons in the core states and means that a planewave representation is inefficient due to the number and high energy of the planewaves which would be required. The use of a planewave basis set also means that no assumptions are made about the likely valence electron distribution in the calculation.

2.2.4.2 Pseudopotentials

The pseudopotential approach modifies the effective potential experienced by the valence electrons when they move through the core region, which is done carefully so that the rapid electronic oscillations are removed while the orbital energies, ε_i, are kept the same. The weaker effective potential, V_{eff}, produced by the pseudopotential means that the eigenstates of lowest energy have been shifted upwards and now correspond to the valence states: the core states given by the nuclear potential, V_c, have disappeared. This approach, therefore, has the added advantage that the core electrons now no longer need to be modelled: their representation can be included within the functional form of the pseudopotential.

A pseudopotential is derived by carrying out an all electron Density Functional Theory calculation for a given atomic species. The pseudopotential, which usually has an assigned analytical form, is then parameterised to reproduce the eigenfunctions and eigenvalues from the all electron calculation. More precisely, the pseudopotential must reproduce the correct eigenvalues for the valence states and the correct eigenfunctions for $r > r_c$, where r_c is a cutoff radius greater than the atomic core radius. Also, it is important that the electron density within the core region matchs that calculated for the all electron case, in which case the pseudopotential is 'norm-conserving' (Hamann 1979).

In the free atom, the spherical symmetry of the system means that each electronic orbital has a distinct angular momentum quantum number, *l*. The derivation of the pseudopotential must be done separately for each value of *l* so that the correct eigenstates are given. A pseudopotential that has been derived in this way is usually called 'non-local'.

Pseudopotentials are often described as 'hard' or 'soft', depending on the effective potential that they produce. A hard pseudopotential has a smaller core radius and produces an effective potential that is very localised around the atom. The pseudopotentials that have been used for the DFT work in this thesis are known as ultrasoft (Vanderbilt 1990). Ultrasoft pseudopotentials are *fully* nonlocal, so that core states with different radial and angular values are treated separately, which allows the cutoff radius to be increased without the loss of transferability. These pseudopotentials were developed so that calculations on first row transition metal systems could be

carried out using planewaves with lower kinetic energies than those required with standard non-local pseudopotentials.

2.2.4.3 Perfect Lattice Simulation

The planewave, pseudopotential approach is ideally suited to the simulation of periodic systems because the plane wave basis set is already periodic in nature. For a perfect lattice, the effective potential, V_{eff}, must reproduce the periodic symmetry of the unit cell:

$$V_{eff}(\mathbf{r} + \mathbf{t}) = V_{eff}(r), \qquad 2.54$$

where **t** is a vector defined by any translation within the lattice. This means that the electronic eigenfunctions, $\Psi_i(r)$, are Bloch functions and can be expressed as:

$$\Psi_i(r) = \exp(i\mathbf{q}.\mathbf{r})u_i(\mathbf{r}), \qquad 2.55$$

where **q** is a wavevector within the Brillouin zone and $u_i(\mathbf{r})$ is a function which has the full periodicity of the lattice:

$$u_i(\mathbf{r} + \mathbf{t}) = u_i(\mathbf{r}). \qquad 2.56$$

As $u_i(\mathbf{r})$ is periodic, it can be expanded in terms of a planewave basis set whose wavevectors, **G**, are the reciprocal lattice vectors of the periodic system:

$$u_i(\mathbf{r}) = \Omega^{-\frac{1}{2}} \sum_G a_{iG} \exp(i\mathbf{G}.\mathbf{r}), \qquad 2.57$$

where a_{iG} are the planewave coefficients and Ω is the volume of the unit cell. As before, the summation is taken only over occupied states.

In practical simulations there are two methods which are used to limit the cost of the calculation. The first is that the kinetic energy of the plane wave basis set is limited to a maximum cutoff value, E_{cut}. This means that $u_i(\mathbf{r})$ is expanded with a finite number of planewaves - those at shorter wavelengths are excluded. The second feature is that the number of wavevectors included in the calculation must be restricted. In principle, the electron density is integrated over all $\mathbf{q}$. In practice this is approximated with a Brillouin zone sum (Chadi 1973), so that $\rho(\mathbf{r})$ is given by:

$$\rho(\mathbf{r}) = \sum_q w_q \sum_i \left|\Psi_{qi}(\mathbf{r})\right|^2, \qquad 2.58$$

where Ψ_{qi} are the electron eigenfunctions at wavevector $\mathbf{q}$, and w_q are a set of 'weights' used to control the relative contribution from the sampling vectors of k-points, $\mathbf{q}$.

Both these practical considerations limit the ability of the simulation to model systems in which the electron density changes very rapidly through space. Therefore, it is very important to carry out a series of tests to determine the convergence of the ground state energy and the optimised atomic geometry with the planewave cutoff, E_{cut}, and the number of sampling k-points used in the simulation. Convergence tests for the systems studied in this thesis are included at the end of this chapter.

2.2.5 Calculation Details

All the electronic structure work in this thesis has been carried out with the Vienna Ab-initio Simulation Package, VASP, (Kresse 1996a, 1996b) codes which employ Density Functional Theory within the GGA and the pseudopotential approximation, using a planewave basis set. VASP makes use of ultra-soft Vanderbilt (1990) pseudopotentials and conjugate gradient minimisation methods for the location of the ground state energy. The number of k-points and their co-ordinates is determined using the scheme of Monkhorst and Pack (1976), where each reciprocal lattice vector is subdivided to form a k-point grid. The k-point co-ordinates along each reciprocal lattice vector are obtained as follows:

$$X_l = W_l \pm k / 2N \qquad 2.59$$

where W_l is the corresponding component of the optional shift vector, k = 1,3,.....,(N-1) when N is even, and k = 0,2,.....,(N-1) when N is odd. For the purpose of the calculation, the resulting k-point set can be reduced by a half due to the presence of inversion symmetry in reciprocal space.

2.3 Convergence Tests

Before studying a material in detail it is important to gain insight into how the choice of planewave cutoff and the number of k-points used in the calculation affect the calculated ground state energy and the resulting optimised geometry. The convergence

tests for the materials studied in this thesis are outlined in the following sections. It is also important to note that the accuracy of the simulation is always limited by the available computational resources and time. Deciding on the accuracy which is required and monitoring the resulting cost of the calculation is the aim of these tests.

2.3.1 V_2O_5

Our initial work focused on ensuring that our methods reproduced correctly the V_2O_5 structure, and the selection of a suitable planewave cutoff, E_{cut}, for the main body of work. The total energy of the system should converge as E_{cut} is increased. Therefore, the correct cutoff for the system can be found by carrying out a series of geometry optimisations of the V_2O_5 structure with increasing E_{cut}. By comparing the resulting total energies and geometries, a cutoff can be selected that balances accuracy with computational cost. The dependence of the total energy and the unit cell dimensions on planewave cutoff are given in Figs. 2.5 and 2.6.

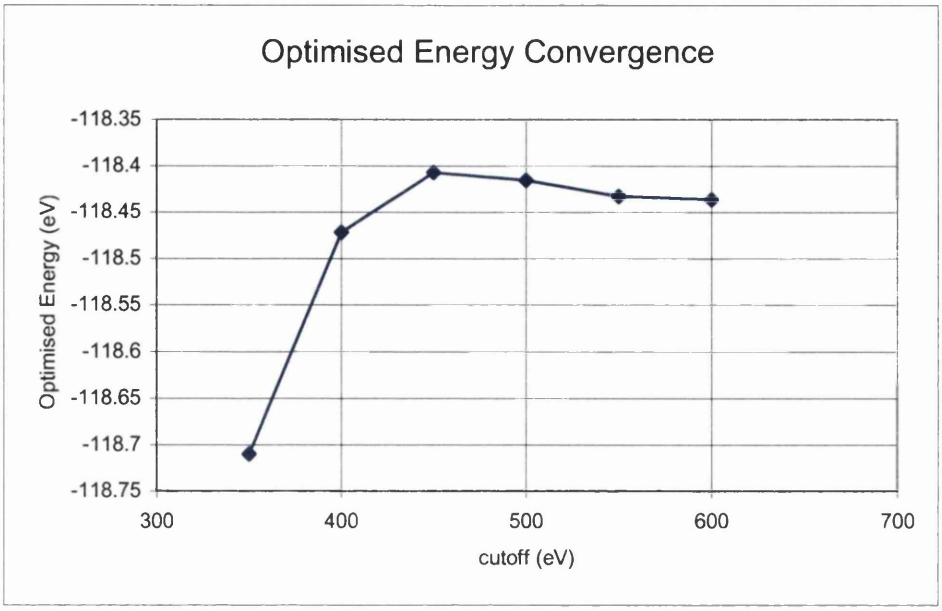

Fig.2.5. Dependence of V_2O_5 optimised energy on planewave cutoff.

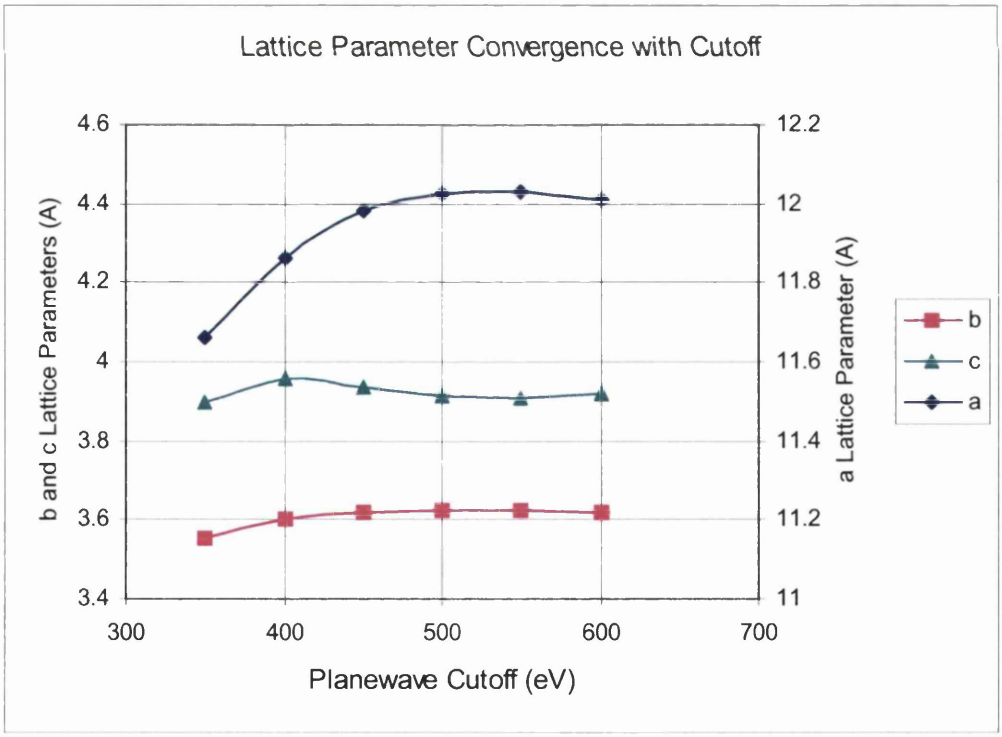

Fig.2.6. Dependence of optimised lattice parameters of V_2O_5 on planewave cutoff.

While the optimised total energies appear to oscillate above a cutoff of 450eV there is still convergence within 0.05 of an eV. Also, the V_2O_5 structure converges at a cutoff of around 500eV. Based on these results we have used a planewave cutoff of 550eV in this work, as it is energy differences and not actual values that are of interest to us.

As the concentration of intercalated lithium increases, the electrical conductivity of the $Li_xV_2O_5$ system improves, and therefore the number of k-points required to accurately sample the Brillouin zone is greater. The convergence of total energies with increasing number of k-points has been examined in a series of single point calculations on $Li_2V_2O_5$, the most highly lithiated phase in this work. The results in Fig. 2.7 show that the number of k-points has a small effect on the value of the total energy, with convergence occurring at around 20 k-points. We have taken this value for the main body of our work, as it keeps the resources needed for the calculations to a manageable size.

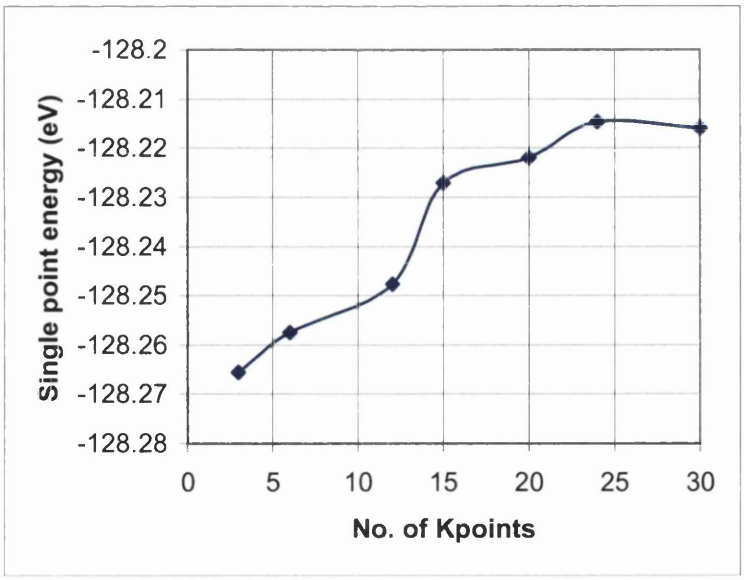

Fig.2.7. The dependence of single point energy of $Li_2V_2O_5$ on the number of k-points used in the calculation.

As the present work concentrates on energy differences and not on absolute values, the effect of any systematic errors that are present is reduced. Calculated lattice parameters and selected bond lengths of the optimised V_2O_5 structure are compared to experiment in Table 2.1.

Observable	Experiment	Calculation	Error (%)
a lattice parameter (Å)	11.512	11.698	1.62
b lattice parameter (Å)	3.564	3.587	0.65
c lattice parameter (Å)	4.368	4.471	2.36
V=O, vanadyl (Å)	1.577	1.607	1.90
V.....O, ionic (Å)	2.793	2.865	2.58

Table 2.1. Calculated structure of V_2O_5 using Density Functional methods.

There is acceptable agreement between the experiment and calculation, although the well-known tendency for GGA methods to underestimate binding energies and therefore overestimate unit cell parameters is seen in Table 2.1.

2.3.2 V_6O_{13}

The convergence of the V_6O_{13} structure with planewave cutoff has been assessed using the same methods described in the previous section. The dependence of the optimised total energy, and the unit cell dimensions on planewave cutoff are given in Figs. 2.8 and 2.9 respectively.

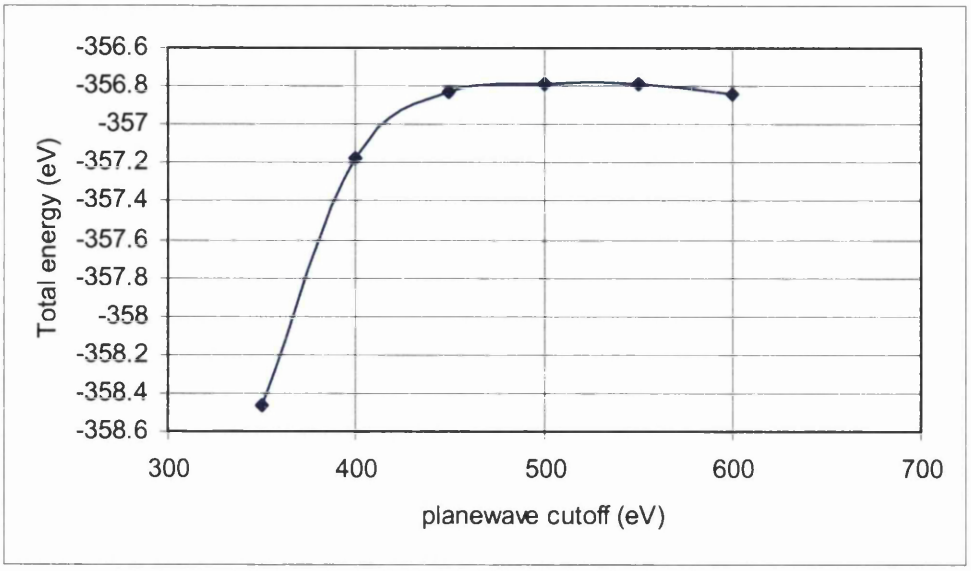

Fig. 2.8. Convergence of optimised total energies with planewave cutoff for V_6O_{13}.

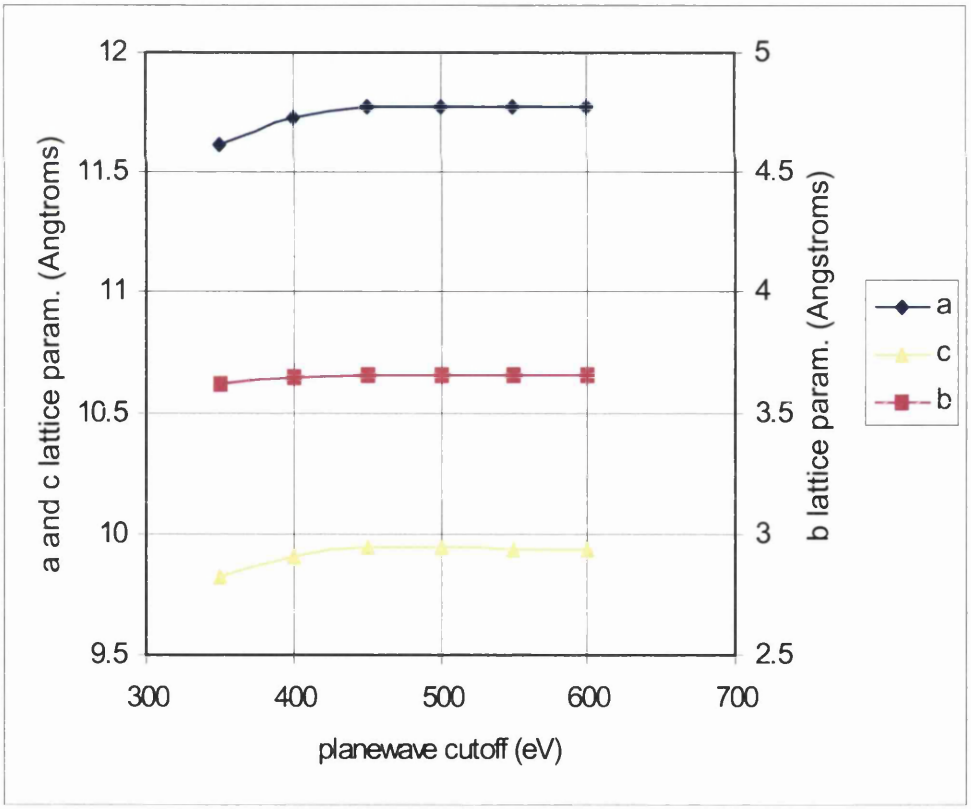

Fig. 2.9. Convergence of optimised cell parameters with planewave cutoff for V_6O_{13}.

Convergence of the optimised total energy and geometry with planewave cutoff occurs at around 500eV, which is similar to the behaviour of the V_2O_5 system. This similarity

is due to the presence of the same atomic species in each material, which results in the same pseudopotentials being used in each set of calculations. Therefore, we have used a planewave kinetic energy cutoff of 550eV for all the DFT calculations of the $Li_xV_6O_{13}$ system - the same cutoff that is employed for $Li_xV_2O_5$.

For the $Li_xV_6O_{13}$ system, the k-points are generated using a 2 x 5 x 2 grid, which gives a k-point spacing which is similar to that in $Li_xV_2O_5$. The k-point grid, which reflects the dimensions of the reciprocal unit cell, is the finest mesh that could be used, while keeping the calculations to a manageable size.

2.3.3 Spinels

We have also used density functional theory to simulate a number of spinel phases, $Li_xCo_yMn_{(4-y)}O_8$, by employing the planewave pseudopotential approach. As the metal species are different in this series of calculations, the pseudopotentials that are used will produce a different effective potential, and this may affect the convergence of the optimised energy and geometry with planewave kinetic energy cutoff. The convergence of the total energy and the unit cell dimensions with planewave cutoff are given in Figs. 2.10 and 2.11.

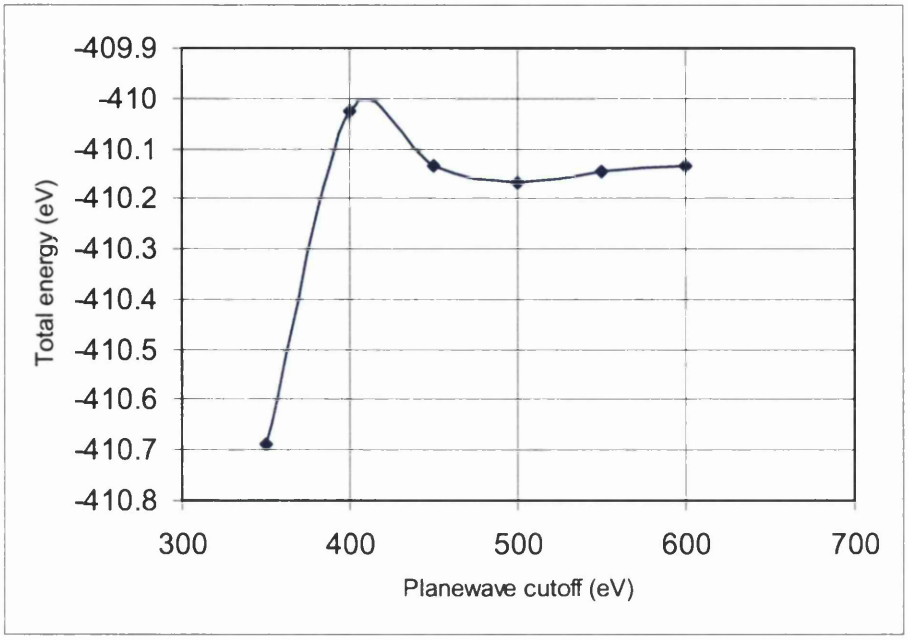

Fig. 2.10. Convergence of optimised total energies with planewave cutoff for spinel phase $Li_2CoMn_3O_8$.

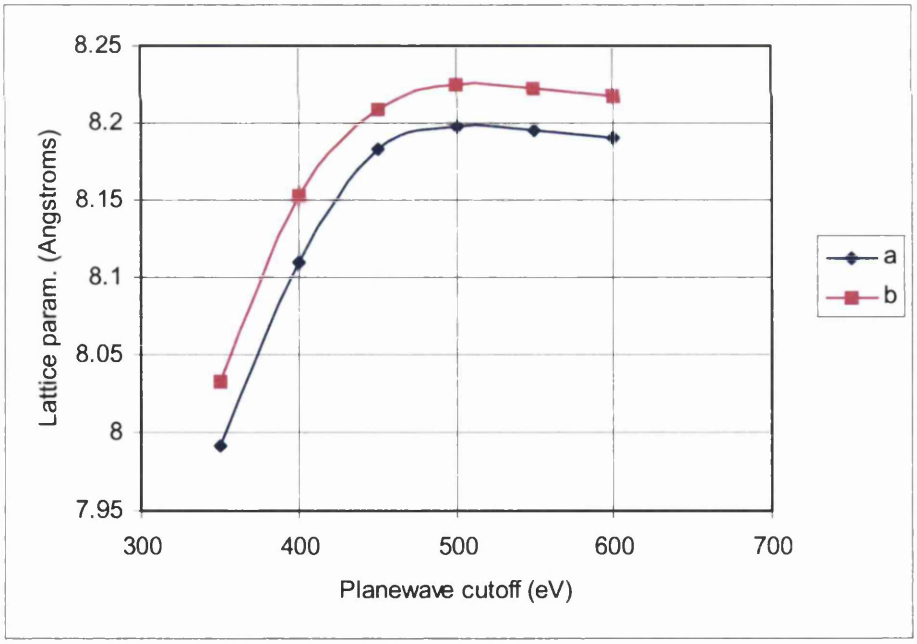

Fig. 2.11. Convergence of optimised cell parameters with planewave cutoff for spinel phase $Li_2CoMn_3O_8$.

As we have already shown for the vanadium oxides the convergence, with planewave cutoff, of the optimised total energy and geometry of the spinel $Li_2CoMn_3O_8$ occurs at around 500eV. The similarity of the convergence of all three systems is likely to be due

to the effective potential generated by the oxygen pseudopotential, which requires the most extensive valence electron basis set. Consequently all the DFT simulations of the $Li_xCo_yMn_{4-y}O_8$ system have been carried out with a planewave cutoff of 550eV.

Chapter 3

Lithium Intercalation into V_2O_5

3.1 Introduction

V_2O_5 was first suggested as a cathode material in the 1970s (Day 1972) because it was found that the material could incorporate large concentrations of lithium ions in a reversible manner. Great interest in the material was aroused when test cells, constructed with a lithium metal anode, were found to perform well when cycled over 100 times while giving reasonably high voltages. V_2O_5 cathodes have since undergone extensive experimental study by a large number of authors (Cava 1986, West 1993, Cocciantelli 1995, Prouzet 1996, Vivier 1998, Zhang 1998). A number of these studies are reviewed in more detail later in the chapter.

More recently, theoretical methods such as Density Functional Theory have started to be used to study cathode materials. Studies on first row transition metal oxides and sulphides have proved to be very successful although, to date, relatively few studies have been reported on the vanadium oxides (Kempf 1993, Benedek 1997, Aydinol

1997a, Ceder 1997). Atomistic simulation techniques have been used to study the catalytic properties of V_2O_5 surfaces (Sayle 1996a, 1996b, 1996c) but this is the first time that such techniques have been used to investigate lithium intercalation into V_2O_5. Comparisons with other theoretical work will be made where possible.

Studying a material that is well known experimentally has allowed us to thoroughly test the theoretical methods used. It is important that both atomistic and electronic structure methods can reproduce the layered V_2O_5 structure accurately, and that any structural changes on lithium intercalation can also be modelled correctly. After this has been demonstrated we use a combination of theoretical methods to predict the voltage during cell discharge and investigate the changes to the electronic structure that accompanies lithium insertion. This leads to a better understanding of the factors which influence the cell voltage and cycling performance, and therefore helps in the design of better cathode materials for use in solid state lithium ion batteries.

3.2 Experimental Structural Properties

3.2.1 Vanadium Pentoxide

The first crystallographic data on V_2O_5 was reported by Ketelaar in 1936 and later by Byström *et al* (1950). The oxide has a structure made up of octahedra joined by edge and corner sharing. The electrostatic repulsion between neighbouring vanadium atoms results in the vanadium atoms being displaced away from the base of each pyramid and towards the apex oxygen. This displacement produces a short vanadyl bond, at only

1.577Å, from the vanadium atom to the apex oxygen. The longest V-O bond is trans to the vanadyl V=O and, at 2.791Å, is essentially an ionic bond.

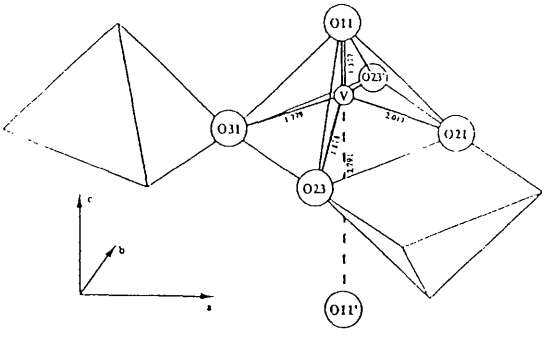

Fig.3.1. Local oxygen co-ordination around the vanadium.

The VO_6 octahedra are distorted to such an extent that, in a detailed refinement of the structure carried out by Enjalbert and Galy in 1986, it was suggested that V_2O_5 is better represented by VO_5 square based pyramidal units, as shown in Fig.3.1. This representation helps to stress the layered structure of the material and the relatively weak bonding between the layers, a property that is of fundamental importance to its performance as a cathode material.

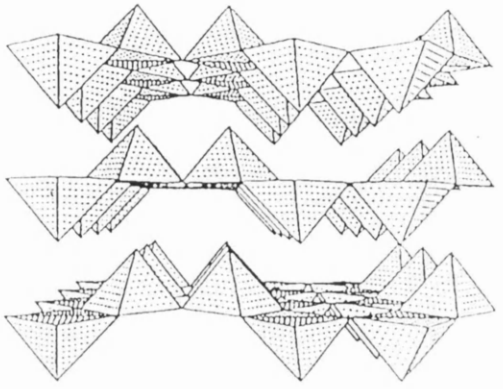

Fig.3.2. The layered structure of V_2O_5

V_2O_5 has been found to intercalate a number of alkali, alkaline earth, and transition metal cations, such as Li^+, Na^+, K^+, Sr^{2+}, Ca^{2+}, and Cu^+, into the interlayer space. A double layer structure, where the cations are incorporated between alternate layers, is sometimes adopted for large metal species in high concentrations. Water can also be introduced into the structure to produce sol-gel like structures.

3.2.2 Lithiated Phases

The $Li_xV_2O_5$ system can adopt many structural phases depending on temperature and lithium concentration, x, and this leads to a relatively complex phase diagram, which is shown in Fig.3.3. The method of preparation also has an important influence over the structural phase obtained. It is possible to use electrochemical techniques to synthesis $Li_xV_2O_5$ compositions which are meta-stable compared to those on the phase diagram.

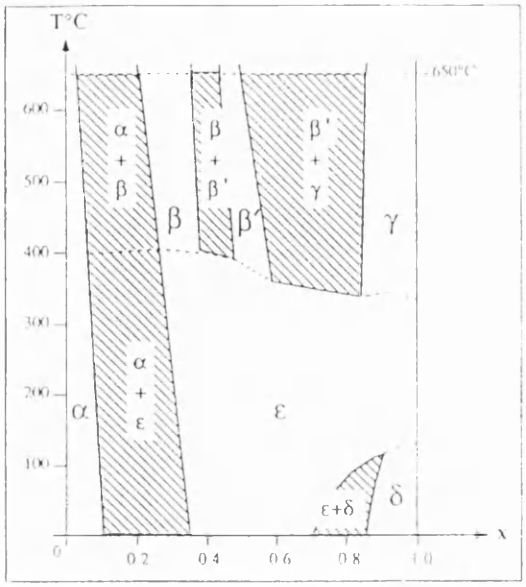

Fig.3.3. Phase diagram for $Li_xV_2O_5$ (Galy 1992).

Phases which occur at low levels of lithium intercalation, such as α-$Li_xV_2O_5$ and ε-$Li_xV_2O_5$, involve very little structural distortion of the bulk oxide and have X-ray powder diffraction patterns which are almost identical to those of pure V_2O_5 (Cava 1986). The α phase, which has a very low lithium content ($x \leq 0.1$) and the ε phase ($0.35 \leq x \leq 0.70$) are both stable at temperatures below 400°C. The only distortion of the V_2O_5 structure is a slight puckering of the pyramidal units parallel to the *a* direction, which results in a minor reduction of the cell parameter in that direction, an effect that becomes more pronounced as the lithium concentration increases. ε-$Li_xV_2O_5$ also shows a steady expansion of the *c* lattice parameter as x increases, due to the increased concentration of lithium between the V_2O_5 layers.

At higher lithium concentrations, $0.70 \leq x \leq 1.0$, the formation of the δ phase occurs. Although visibly similar to the α and ε phases, the powder pattern for δ-$Li_xV_2O_5$ contains a number of extra reflections (Cava 1986), indicating some local structural

rearrangement as well as significant unit cell expansion. The remaining phase that occurs at room temperature, for $x > 1.0$, is γ-$Li_xV_2O_5$, which involves a rearrangement of the VO_5 polyhedra to an alternate up-down configuration.

Higher temperature phases, such as β-$Li_xV_2O_5$, have a square based pyramidal arrangement, which is significantly different from that in V_2O_5 (Galy 1992). β-$Li_xV_2O_5$, which occurs above 400 °C and with $0.22 \leq x \leq 0.49$, is considerably distorted so that the square pyramidal units form tunnels within the lattice. The layered structure of bulk V_2O_5 is totally disrupted and the incorporation of lithium has become irreversible.

Prouzet *et al* (1996) have carried out *in situ* XANES and EXAFS to study the local structure in the $Li_xV_2O_5$ system for $0.0 \leq x \leq 0.78$. They observe that the local coordination of the vanadium centres becomes more symmetric as the degree of lithium intercalation increases, indicating the gradual reduction of V(V) to V(IV). The resulting decrease in the Coulombic repulsion between the metal centres is demonstrated by a reduction in the V-V distance by 0.08Å. The degree of vanadium reduction that accompanies lithium incorporation will be investigated in detail in this chapter.

The unit cell expansion during lithium intercalation has been studied by Murphy *et al* (1979b) by treating solid V_2O_5 with a solution of lithium iodide in acetonitrile at room temperature, to give a series of $Li_xV_2O_5$ bronzes of varying composition. X-ray powder diffraction was used to determine the dependence of the lattice parameters on lithium concentration ($0.0 \leq x \leq 1.0$), which is given in Fig.3.4. It can be seen that the increase in the unit cell volume is due to expansion along the *c* axis, which can be rationalised as an increase in the separation of the V_2O_5 layers, in turn due mainly to steric effects.

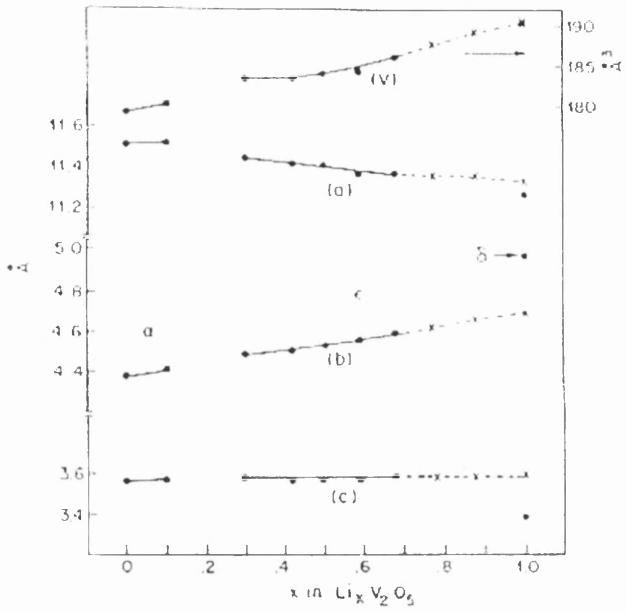

Fig. 3.4. Experimental measurements of V_2O_5 lattice parameters during lithium intercalation (Murphy 1979b).

Our present theoretical study is confined to energy calculations of static structures at zero Kelvin. Therefore, we focus on changes that occur to the dimensions of the unit cell as lithium is introduced into the oxide, which we relate to experiment. The investigation of temperature effects is reserved for further studies.

The changes in electrical conductivity have been investigated by a number of authors (Badot 1992, Shibuya 1995) and it is found that significant changes take place during lithium intercalation (Fig. 3.5). Shibuya *et al* carried out *in situ* and steady state conductivity measurements on a thin film of V_2O_5, into which lithium is introduced using electrochemical methods. The electrical conductivity of the $Li_xV_2O_5$ system peaks at two lithium concentrations, x = 0.25 and x = 0.70, which correspond roughly to the boundaries of the ε phase region. It is assumed that this phase is the reason for the high

conductivity. As the lithium concentration is increased the conductivity falls, and is close to zero above x = 0.9.

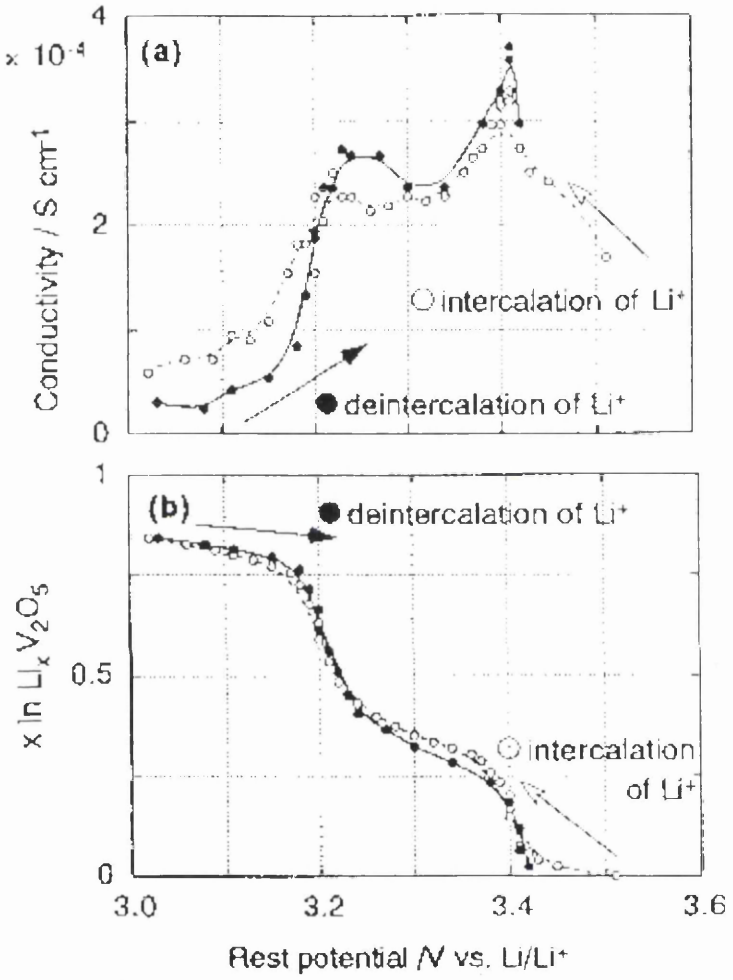

Fig. 3.5 Conductivity (a) and cell composition (b) measured against cell potential (Shibuya 1995).

In pure V_2O_5 the vanadiums are considered to be V(V), d^0 species, and therefore the conduction band (due to the metal *d*-orbitals) is empty. As lithium is introduced into the oxide, the metal centres are reduced and, consequently, the conduction band is populated. It would appear that band conduction cannot be the main contributor to electrical conductivity, since the conductivity falls as the number of mobile electrons appears to be increasing. It seems that a localised electron hopping model is more

appropriate, where the conductivity is determined by the activation energy of the hopping process and not the number of charge carriers.

3.3 Interatomic Potentials

The potential model for V_2O_5 was developed by Dietrich *et al* (1993) by fitting to the experimental crystal structure and physical properties such as elastic constants. They use Buckingham potentials to model most interatomic interactions and a Morse potential to reproduce the short V=O vanadyl bond. This Morse potential and the very repulsive V(V)...O Buckingham potential, which models the weak V.....O ionic bond, reproduce the layered structure of the oxide by significantly distorting the V-O octahedra. Consequently, the set of potentials is specific to this material and it cannot be used to model a different vanadium oxide. The short range forces between O ions were modelled using a Buckingham potential derived by Catlow (1977), while all V-V short range interactions are ignored. They are assumed to be insignificant at the V-V interatomic separations in the crystal and are dominated by the Coulomb interaction.

In the lithium bronzes, Li-O interactions are modelled with a Buckingham potential that has been fitted to the structure of lithium oxide (Binks 1994). We can accurately reproduce the Li_2O structure with the Li-O and O-O interatomic potentials used in this work. A Buckingham potential, derived from empirical fitting to the structure of V_6O_{13} that will discussed in more detail in the next chapter, is used to include V(IV)-O interactions.

The two-body potential parameters are given in Tables 3.1 and 3.2 while details of the ionic charges and shell model parameters can be found in Table 3.3.

Interaction	A / eV	ρ / Å	C / eVÅ^6	r_{min} / Å	r_{max} / Å
V(V)-$O_{equatorial}$	5312.99	0.26797	0.00	0.00	10.00
V(V).....O_{axial}	2549.73	0.34115	0.00	1.99	10.00
V(IV)-O	1290.56	0.34039	0.00	0.00	10.00
O-O	22764.3	0.14900	23.00	0.00	10.00
Li-O	828.01	0.27930	0.00	0.00	10.00

Table 3.1. Buckingham potential parameters and cutoffs used in this study.

Buckingham potential has the form: $\Psi_{ij}(r) = A_{ij}\exp\left(\frac{-r_{ij}}{\rho}\right) - \frac{C_{ij}}{r_{ij}^6}$

Interaction	D_0 / eV	α / Å^{-1}	r_0 / Å	r_{min} / Å	r_{max} / Å
V=O_{axial}	10.00	2.302170	1.584	0.00	1.99

Table 3.2. Morse potential and cutoffs used in this study.

Morse potential has the form: $\Psi_{ij}(r) = D_0\left(\left\{1-\exp\left[\alpha(r-r_0)\right]\right\}^2 - 1\right)$

The shell model is used to model the polarisation of the oxygen ions. The polarisation of all the metal ions is assumed to be negligible, and therefore they are represented simply as point charges.

Species	Charge / |e|	q_{core} / |e|	k / eVÅ^2
V(V)	+5.00	+5.00	∞
V(IV)	+4.00	+4.00	∞
O	-2.00	+0.717	54.952
Li	+1.00	+1.00	∞

Table 3.3. Species charges and shell model parameters used in the potential model of V_2O_5.

3.4 Results And Discussion

Initially, we present results from a series of defect calculations using interatomic potential based methods, which have been used to find the most stable lithium sites in the V_2O_5 lattice. These results are then used to give starting geometries for electronic structure calculations on a range of $Li_xV_2O_5$ phases, giving information on the structural changes induced by lithium intercalation, thermodynamic properties, and the electronic structure of the lithiated phases. Finally, we return to the atomistic calculations to study lithium migration processes in the V_2O_5 lattice.

3.4.1 Low Energy Lithium Sites

Mott-Littleton calculations have been used to identify low energy sites for Li^+ within the V_2O_5 lattice. We note that the calculated energies correspond to the change that occurs when an isolated Li^+ ion is introduced into the infinite V_2O_5 lattice; hence, the effects of Li^+ - Li^+ interactions are not included in this calculation. Such calculations do not model the changes in the unit cell dimensions that will occur when lithium is

intercalated into V_2O_5, but serve as a good guide to the positions that the Li^+ ions will occupy in the oxide, especially at low lithium concentrations and, as such, provide good starting geometries for the lithium ions in the subsequent electronic structure work. The defect energies of fifteen interstitial Li^+ sites have been calculated in this way. Explicit relaxation of the ions closest to the defect, within a region with a radius of 8 Ångstroms, containing around 300 atoms, gives converged defect energies. The dependence of these defect energies on this region size has been investigated and found to converge at around 7-8 Ångstroms. The lowest energy sites identified by the calculations are given in Table 3.4 and shown graphically in Fig.3.6.

Site No.	Lithium position (fractional co-ordinates)	Defect Energy (eV)
1	0.5047 0.0040 0.3976	-8.1945
2	0.5000 0.2588 0.3447	-7.5967
3	0.5049 0.5010 0.4147	-7.3797

Table 3.4. Low energy lithium ion sites in V_2O_5

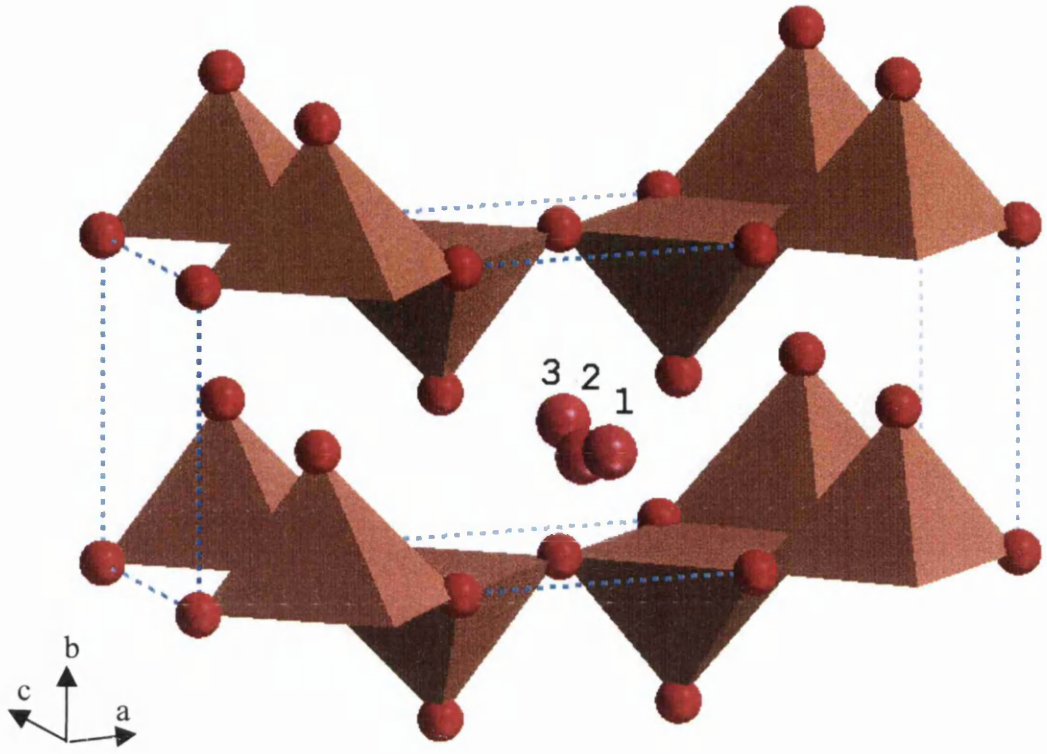

Fig. 3.6. Low energy lithium ion sites within V_2O_5. Reference numbers refer to Table 3.4.

The energy of the defect sites indicates that it is possible for the intercalated lithium to adopt more than one position in the bulk lattice, especially at higher concentrations. Essentially, all the intercalated Li^+ ions are located along the channel that runs through the V_2O_5 structure, parallel to the *b* lattice parameter. The defect calculations indicate that the Li^+ ions experience a flat potential energy surface and, therefore, Li^+ mobility along the [*010*] direction is expected to be high. We investigate this feature in more detail later.

3.4.2 Geometry Optimisation using DFT methods

Electronic structure techniques have been used to carry out full geometry optimisations of a number of $Li_xV_2O_5$ phases with a range of lithium concentrations in V_2O_5, yielding information about structural modifications, charge density distribution and cell voltages.

Initial calculations to check the reliability of our methods and assess the convergence of the optimised energy and structure with the plane wave kinetic energy cutoff were undertaken on pure V_2O_5 and three $Li_xV_2O_5$ phases. The lithium atoms were inserted in the channel that runs along the [*010*] direction at the three most stable sites indicated by the interatomic potential defect calculations (see Table 3.4). These test calculations, carried out on a single V_2O_5 unit cell, showed that the atomistic defect simulations did give a good estimate of the sites adopted by the lithium ions in the V_2O_5 lattice. We then conducted a detailed structural study of six $Li_xV_2O_5$ phases, by simulating supercells of composition x=0.25, 0.5, 0.75, 1.0, 1.5, and 2.0. An accurate value for the total energy of lithium metal has also been calculated by carrying out a geometry optimisation using the same plane wave kinetic energy cutoff. This will be used to make predictions of the cell voltage.

Each $Li_xV_2O_5$ phase has been simulated by varying the number of lithium ions in a supercell which consists of two unit cells of V_2O_5 repeated along the [*010*] direction. Using this supercell instead of a single V_2O_5 unit cell allows more dilute lithium concentrations, and a greater number of compositions, to be simulated. Geometries have been optimised with P1 symmetry and with all unit cell dimensions and angles allowed to vary. For compositions where $x \leq 1.0$, the initial structure for V_2O_5 is that of the optimised host lattice, while the starting co-ordinates of the lithium atoms in the V_2O_5 host have been varied to check that the global minimum has been found.

For phases with higher lithium concentrations, it was necessary to carry out the simulations in two stages. First, the unit cell parameters are optimised with the atomic positions held constant to allow the unit cell to expand in response to the intercalated

lithium. The resulting structure is then used as the starting point for a full geometry optimisation. This two step process avoids carrying out a full optimisation from an initial geometry that may lie far from the energy minimum, and therefore reduces the number of variables until the geometry is close to the energy minimum.

The most stable structures for a selection of the $Li_xV_2O_5$ phases are given in Fig. 3.7.

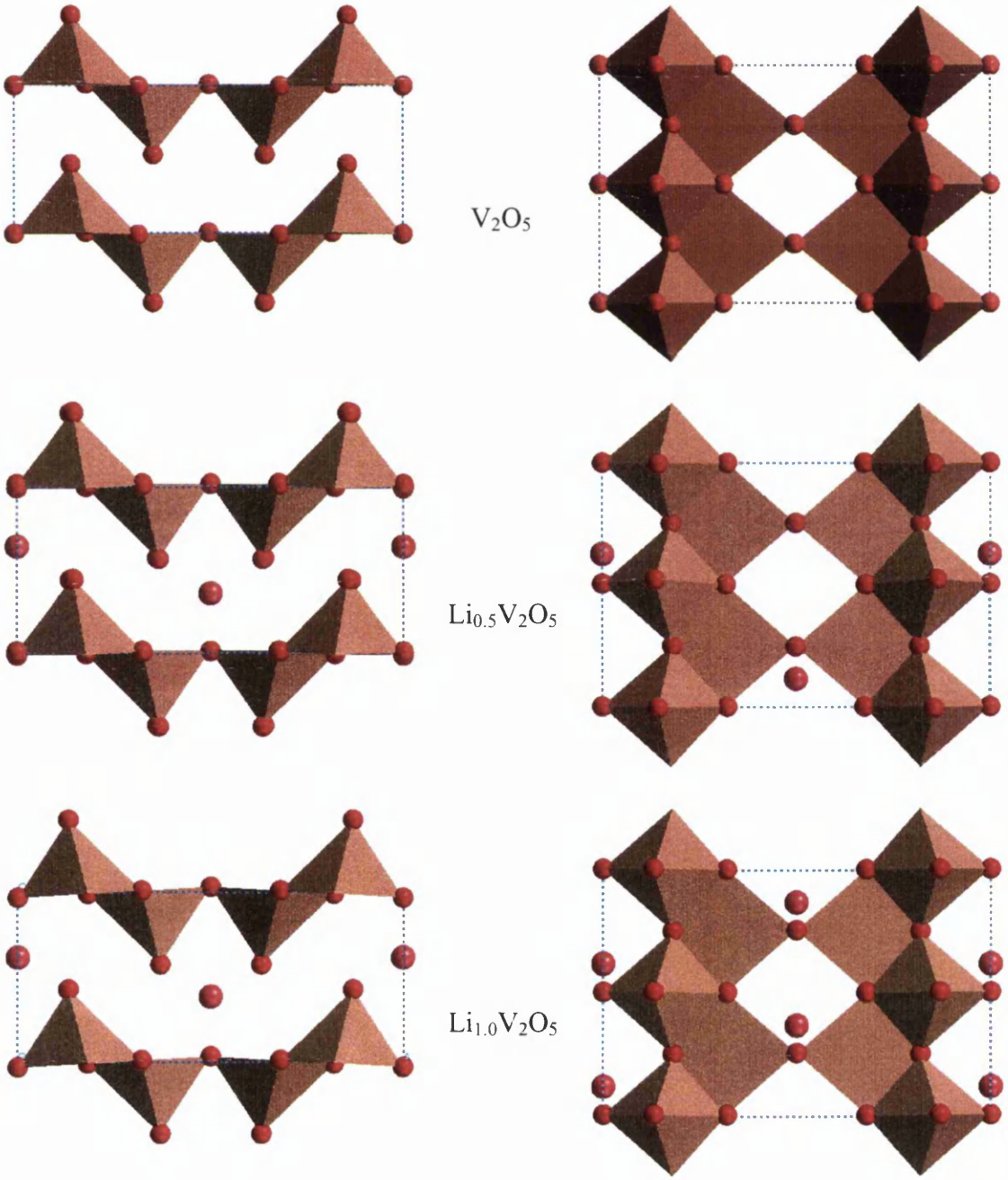

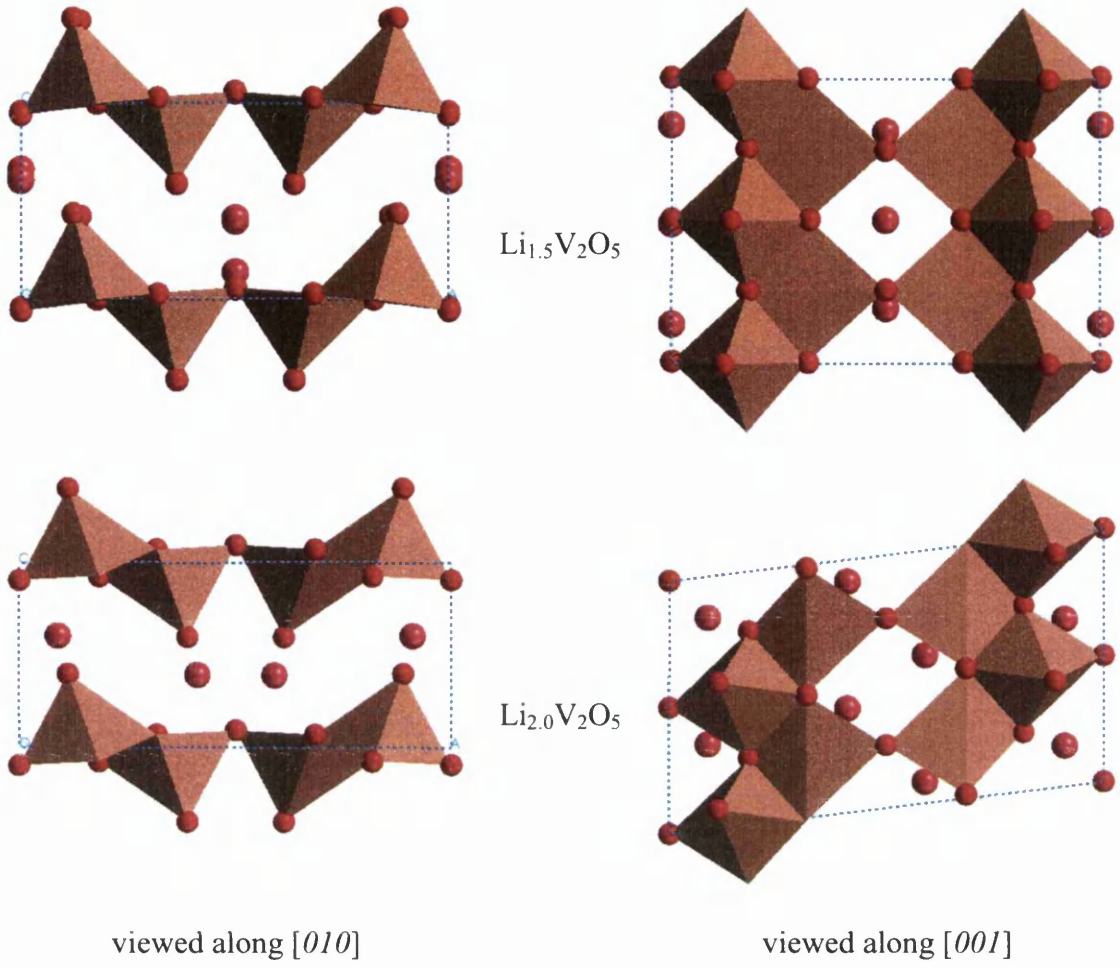

Fig. 3.7. Optimised geometries of a) V_2O_5, b) $Li_{0.5}V_2O_5$, c) LiV_2O_5, d) $Li_{1.5}V_2O_5$ and e) $Li_2V_2O_5$

Oxygen atoms are shown in red while lithium atoms are in pink.

Vanadium co-ordination polyhedra are shown.

The changes to the lattice parameters, as the lithium content is increased, are given in Fig. 3.8.

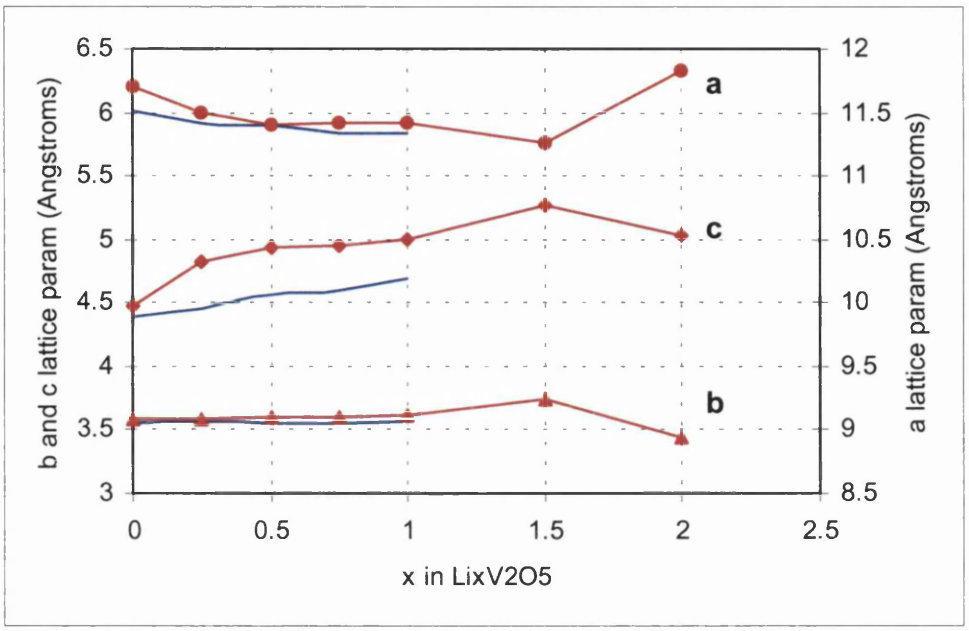

Fig. 3.8. Experimental (Murphy 1979b) and calculated unit cell dimension changes during lithium intercalation. Experimental data is in blue while calculated points are shown in red.

The calculated data reproduces the general trends seen in experiment (shown in Fig. 3.8), for $0 \leq x \leq 1$. The increase in the *c* lattice parameter, as the lithium content increases, is reproduced by the calculations although this effect is somewhat overestimated, while the changes in *a* and *b* are accurately modelled by the simulations. The overestimation of the expansion along the *c* axis may be a result of the periodic boundary conditions in the calculation, as the relatively short repeat distance along [*001*] restricts the possible arrangements of the lithium ions. Even so, it is clear from the present calculations that, on the whole, the DFT technique employed is able to reproduce well the structural changes accompanying the intercalation reaction.

The optimised $Li_xV_2O_5$ structures for $x \leq 1.0$ are all very similar, and there is a clear evolution of the structure as the lithium content is increased, as seen in experiment. The

calculated structures for $Li_{1.5}V_2O_5$ and $Li_{2.0}V_2O_5$ are quite different and a greater degree of rearrangement is required as the lithium concentration is increased between 1.0 and 2.0. This is also evident in Fig. 3.8, where, above x=1.0, there is an end to the smooth changes in the unit cell parameters. In $Li_{1.5}V_2O_5$ the intercalated lithium ions are arranged along the [*010*] direction in two rows, with an offset along the *c* axis. The monoclinic distortion of the cell in $Li_{2.0}V_2O_5$ is produced by the staggered arrangement of the Li^+ ions, as these ions are no longer positioned at y = 0.0 or y = 0.5. Moving from one structure to the other would require considerable structural reorganisation.

The relative stabilities of different atomic arrangements for these phases have been investigated in detail to ensure that the correct minimum energy structures have been found. For example, addition of two more Li atoms to the $Li_{1.5}V_2O_5$ phase does not lead to a more stable configuration for $Li_{2.0}V_2O_5$.

The lithium positions that are predicted by the electronic structure calculations, shown in Table 3.5, can be compared to the results from the atomistic defect calculations in Table 3.4. Good agreement is found along the *a* and *c* axis, while the difference along *b* will be explained by the flatness of the potential energy profile for lithium in that direction.

Phase	Lithium position (fractional)
$Li_{0.5}V_2O_5$	0.5046 0.1714 0.3591
LiV_2O_5	0.4999 0.1761 0.3619

Table 3.5. Optimised lithium atom positions in $Li_xV_2O_5$ phases.

Atomistic calculations are clearly useful tools for finding initial starting configurations for more costly quantum mechanical studies, especially when dealing with complex systems, for which identification of the global energy minimum of the system is more difficult. Substantial savings in computational cost can be made, as some configurations of the system can be rejected quickly using atomistic techniques.

3.4.3 Electron Density Distributions

As we have already noted, the intercalation of lithium must be accompanied by reduction of the host lattice, as the guest species is usually thought to be Li^+. We have investigated this problem by studying the calculated valence electron density distributions. By subtracting the electron density distribution of the bulk oxide from the electron density distribution of the intercalated system, it is possible to calculate the distribution of the electrons due only to the intercalation reaction; i.e. the charge density difference distribution. This subtraction requires us to perform a simulation of the host V_2O_5 distribution for each $Li_xV_2O_5$ configuration using the same atomic positions and unit cell dimensions as the lithiated phases. This is done by removing the lithium ions from the optimised $Li_xV_2O_5$ systems and then carrying out a single point calculation on the distorted host lattice.

To facilitate the following discussion, the vanadium atoms in the V_2O_5 supercell will be divided into two types, V(1) and V(2), as shown in Fig. 3.9.

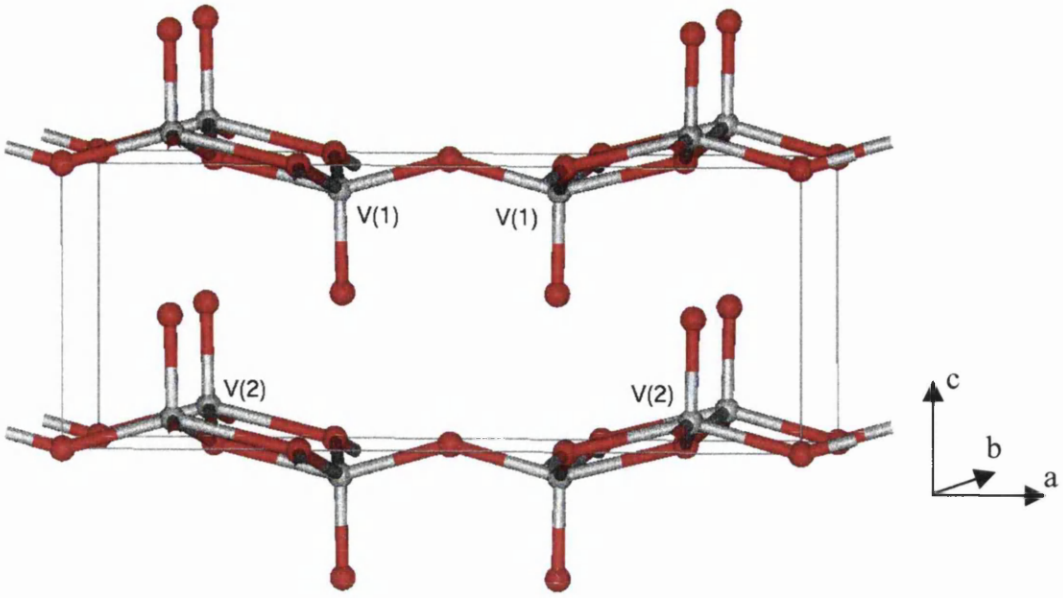

Fig. 3.9. Key to vanadium atom numbering for charge distribution plots (Figs 3.10-3.14).

A number of charge density difference distributions are given as contour plots in Figs. 3.10-3.13, where blue areas represent zero density while green, red, and yellow contours show increasing positive density. Contours occur every $0.1e/Å^3$. Where the slice cuts through atom positions, these are indicated by the element symbol.

Firstly, as expected, we note from Fig. 3.10 that the intercalated lithium is fully ionised so the guest species is Li^+. It occupies a region of zero density in these difference plots, indicating that there is no difference between the electron density in the lithiated and pure host density distributions.

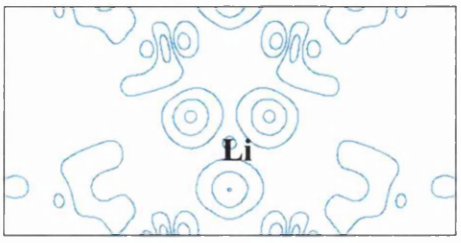

Fig. 3.10. Charge density difference in LiV_2O_5 along the [*010*] direction, through a lithium (Li) atom.

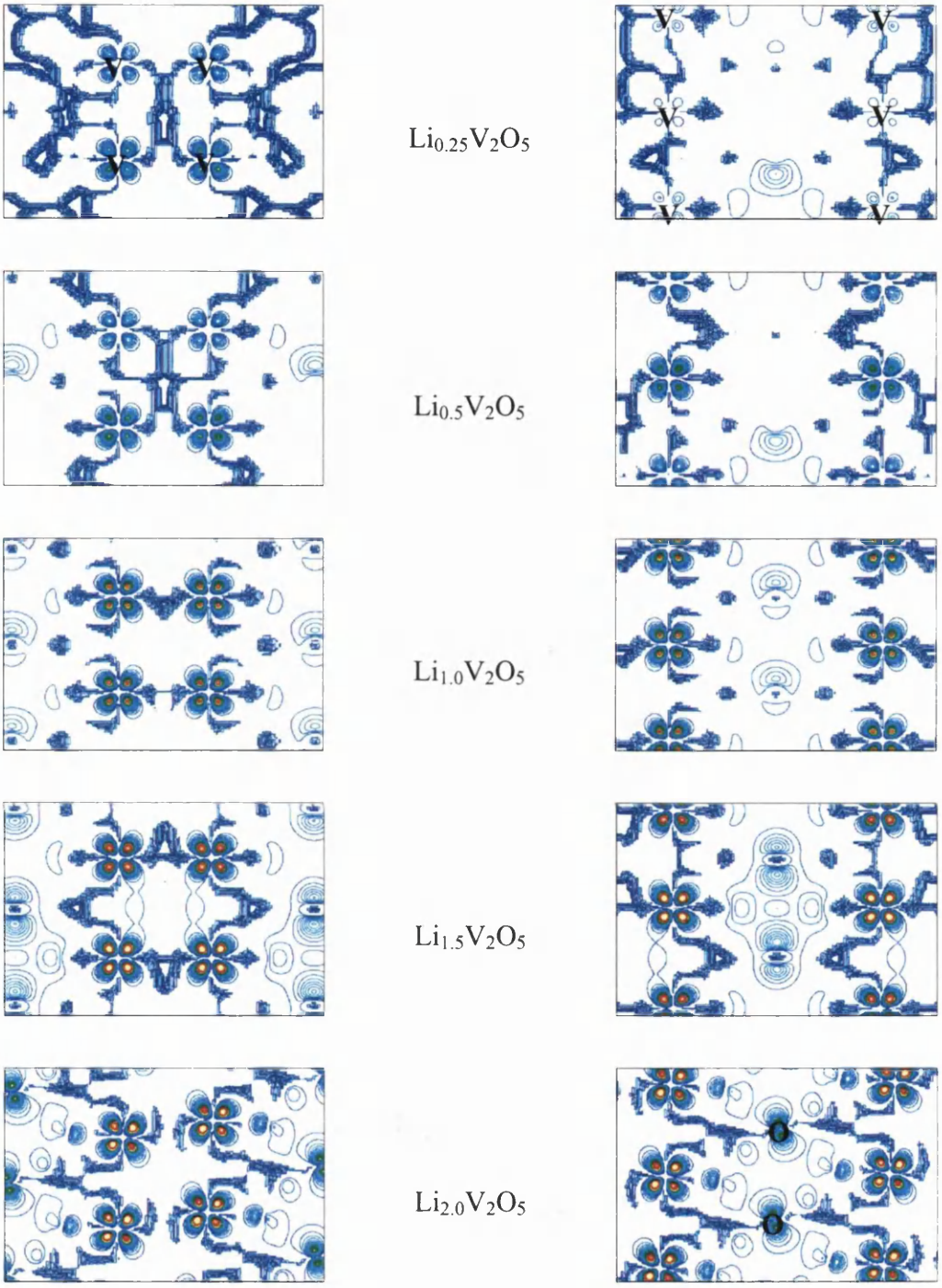

Fig. 3.11. Charge density difference along the [*001*] direction, sliced through both sets of vanadium atoms. Only the positive component of the density is plotted. The positions of the vanadium atoms (V) are shown for the $Li_{0.25}V_2O_5$ slice and two oxygen positions (O) are shown on the $Li_{2.0}V_2O_5$ slice.

From Fig. 3.11 it is clear that the electrons that originated from the intercalated lithium are almost exclusively localised on the vanadium centres in orbitals of π-*d* character. This population of the vanadium *d*-states is also localised to certain atoms, an effect that is most clearly seen at low lithium concentrations. In the $Li_{0.25}V_2O_5$ phase, where only one lithium is incorporated into the simulation supercell to produces a vanadium to lithium ratio of 8:1, we can see that half the vanadium atoms, labelled V(1), have gained electron density while the V(2) centres appear invisible and are unchanged. Closer inspection also reveals that the V(1) centres are not identical, and are split into two groups with varying degrees of reduction. These observations can be rationalised in terms of the distance between the intercalated lithium ion and the vanadium atoms, where the V(1)-Li distances are 2.04 and 2.99Å while the shortest V(2)-Li distance is over 4Å. Therefore, the selective reduction of the vanadium ions occurs as a direct result of the interatomic separations and no filling of delocalised bands, due to the vanadium *d*-orbitals, is seen.

When another lithium is added to the simulation cell the pattern of reduction seen for the V(1) centres is repeated for the V(2) vanadiums. As the lithium concentration is increased still further the electron density continues to populate vanadium π-*d* orbitals and, particularly in the case of $Li_{2.0}V_2O_5$, some density is seen around certain oxygen atoms.

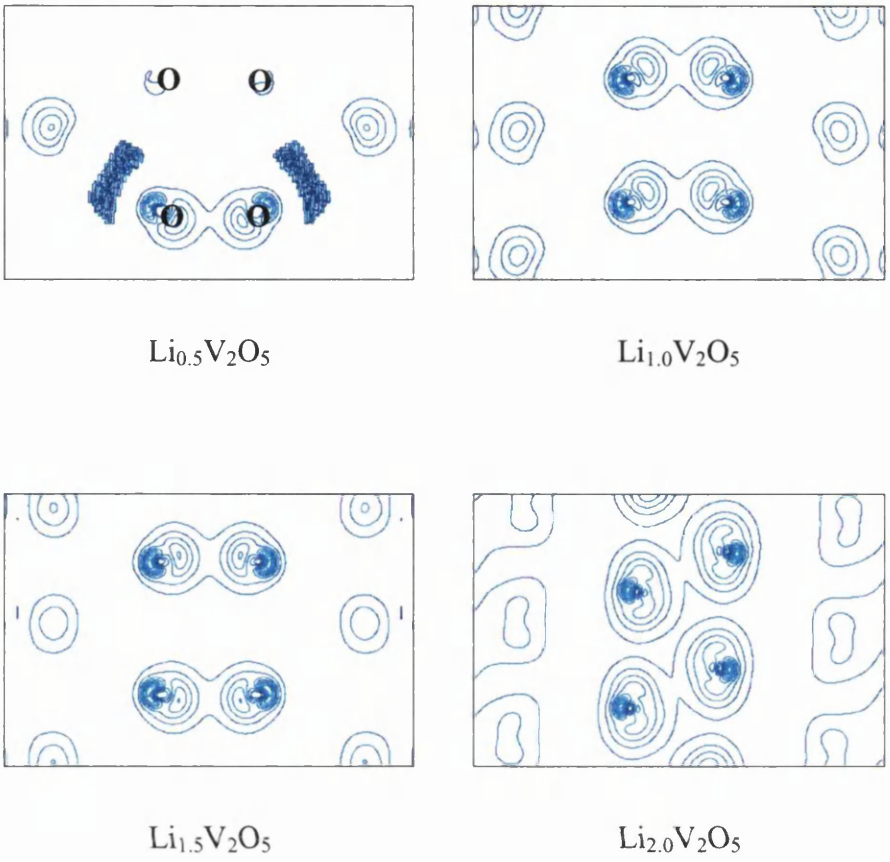

Fig. 3.12. Charge density difference along the [*001*] direction, sliced through the vanadyl O atoms. Only the positive component of the density is shown.

The positions of the oxygen atoms (O) are shown in the $Li_{0.5}V_2O_5$ slice.

From Fig. 3.12 it can be seen that the electron density around the vanadyl oxygens increases slightly during lithium intercalation, although this effect is much smaller than the simultaneous population of the vanadium *d*-states. The additional electron density occupies orbital lobes that point away from the lithium ions in space.

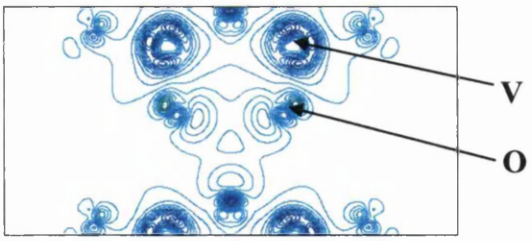

Fig. 3.13. Charge density difference in $Li_{1.0}V_2O_5$ along the [*010*] direction, showing the loss of electron density, shown in dark blue, along the vanadyl bonds.

The reduction of the vanadium centres is accompanied by a reduction in the electron density between the metal and the vanadyl oxygen, which is apparent as areas of negative density on the density difference maps when viewed along the *b* axis (Fig. 3.13). The effect of this loss of density is to steadily weaken and lengthen the vanadyl bond as the lithium concentration increases, which manifests itself in the optimised geometries (see Table 3.6).

Phase	V(1)=O(vanadyl) (Å)	V(2)=O(vanadyl) (Å)
V_2O_5	1.607	1.607
$Li_{0.25}V_2O_5$	1.629, 1.610	1.604
$Li_{0.5}V_2O_5$	1.629, 1.609	1.630, 1.608
$Li_{1.0}V_2O_5$	1.641	1.642
$Li_{1.5}V_2O_5$	1.644, 1.643	1.644, 1.642
$Li_{2.0}V_2O_5$	1.691	1.693

Table 3.6. Optimised vanadyl V-O bond lengths in $Li_xV_2O_5$.

Three vanadyl bond lengths are observed in $Li_{0.25}V_2O_5$, which corresponds to the three vanadium charge states, discussed above, which exist in this phase. The weakening of the short vanadyl bonds as the concentration of intercalated lithium increases is also

seen with IR spectroscopy as the V=O stretch at $1015cm^{-1}$ in V_2O_5 is shifted to lower wavenumbers in the γ phase (Murphy 1979b).

3.4.4 Geometry Optimisation using Atomistic Methods

We attempted to use interatomic potential techniques to model a number of $Li_xV_2O_5$ phases and to make predictions of the cell voltage using Hess's Law. These calculations were carried out by introducing lithium ion into the unit cell at the most stable sites already indicated by the Mott-Littleton results. Clearly, to balance the charges within the unit cell, it was also necessary to reduce an equivalent number of V(V) ions to V(IV), which was simulated in two ways.

Firstly, we changed the formal charges of the required number of vanadium ions from +5 to +4 and used a new V(IV)-O potential to model all the short-range interactions of this new species. This proved to be unsuccessful as the optimised geometries were badly distorted, with the VO_5 polyhedra twisting with respect to each other, which resulted in lattice energies that could not be used to predict insertion energies correctly.

Subsequently, we have attempted to use partial occupancies to model the reduction of the vanadium centres, so that the ionic charge distribution resembles, as far as is possible, the electronic density distribution from the DFT calculations. It has been shown previously that in $Li_{0.5}V_2O_5$, the electron due the intercalated lithium ion is localised over two vanadium atoms. Again in $Li_{1.5}V_2O_5$, a pair of vanadiums is reduced to a greater degree than the other two. Therefore, we use a mixture of V(V) and V(IV)

ions, both with occupancies of 0.5, to represent this situation where a single electronic charge is spread over two metal sites.

The calculated lattice parameters for a number of $Li_xV_2O_5$ phases, optimised using partial occupancies, are given in Table 3.7. We note that V_2O_5 and $Li_{2.0}V_2O_5$ do not contain partial occupancies, as all vanadium species are V(V) or V(IV) respectively, but they are included for completeness.

Phase	a / Å	b / Å	c / Å
V_2O_5	11.37	3.56	4.36
$Li_{0.5}V_2O_5$	10.98	3.55	4.74
$Li_{1.0}V_2O_5$	10.74	3.59	5.18
$Li_{1.5}V_2O_5$	10.29	3.64	5.21
$Li_{2.0}V_2O_5$	11.59	3.54	4.82

Table 3.7. Calculated lattice parameters for $Li_xV_2O_5$ phases using atomistic methods with partial occupancies for the vanadium atoms.

The use of partial occupancies improves the calculated structures for $0.0 < x < 2.0$, although some distortion of the unit cell does occur with α changing by 10-20° during the optimisation of some phases. Still, there is a relatively smooth evolution of the lattice parameters as the lithium concentration increases, with contraction of the unit cell along [*100*] and slight expansion of *b* and *c*, trends that are identical to those seen in the DFT simulations. This pattern does not hold true for the final structure, $Li_{2.0}V_2O_5$, which could be due to the changes in the interatomic model potential as the V(V) species are no longer present, although a similar break in the trends seen at lower lithium concentrations also occurred in the DFT calculations. The similarity in the

atomistic and electronic structure results could indicate a phase change between x = 1.5 and x = 2.0.

3.4.5 Electrochemical Data

Many electrochemical studies have been carried out on test cells containing various phases of $Li_xV_2O_5$. West *et al* (1995) have found that, at 100°C, it is possible to intercalate Li^+ electrochemically into the α and ε phases over a lithium composition range which is far wider than the thermodynamically stable ranges given above. The test cell cycles reversibly for $0.0 \leq x \leq 1.0$, which corresponds to a cell voltage change from 3.5V to 2.75V relative to a cell anode of solid lithium. The voltage curve, shown in Fig.3.14, exhibits two distinct plateaux at 3.4V and 3.2V, an indication of two separate Li sites in the host V_2O_5 lattice. The sharp differential capacity peak at 3.4V accompanies the phase change from α to ε, a minor structural rearrangement.

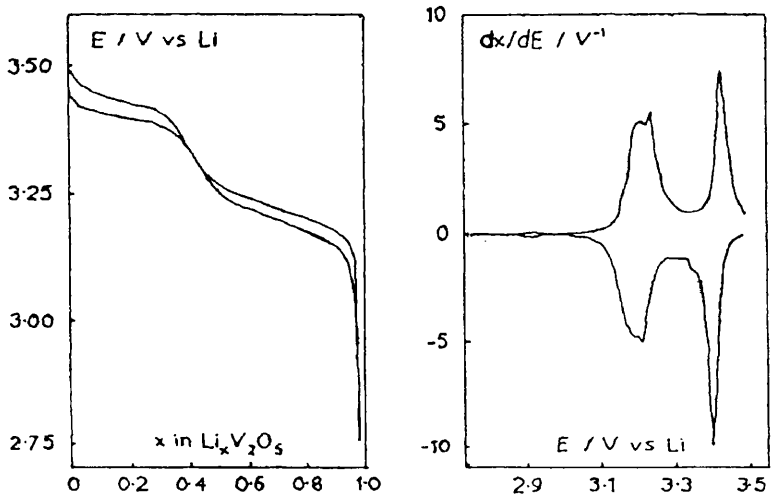

Fig. 3.14. Experimental electrode potential and differential capacity for constant current cycling down to 2.75V for a Li/V_2O_5 test cell (West 1995).

It is possible to discharge the test cell down to 2.2V, which corresponds to x=1.8, and still reversibly remove the lithium when recharging (Fig. 3.15A). There is little change between the first, second, and subsequent cycles. Some broadening of the differential capacity peaks, due to a gradual loss of crystallinity, occurs but no new peaks are observed. Further discharge past 2.2V results in an irreversible structural transformation to the ω-phase where some of the intercalated lithium is strongly bonded to the host oxide and cannot be electrochemically removed (Fig. 3.15B). They find that it is possible to incorporate up to just under three lithium atoms per V_2O_5 formula unit.

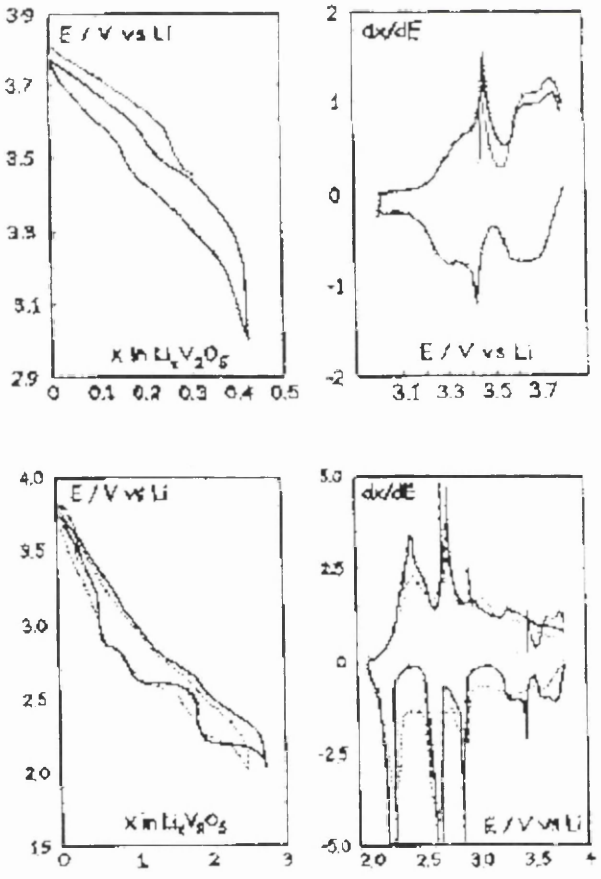

Fig. 3.15. Electrode potential and differential capacity for constant current cycling down to 2.2V (A) and 1.75V (B) (West 1995).

3.4.5.1 Calculated Cell Potentials

The calculation of cell potentials and the reproduction of the experimental cell discharge curve are important aims of this work. We present initial results that show the validity of our simulations, as applied to the problem.

In this study, as in previous work by other authors (Aydinol 1997a, Deiss 1997), the average cell voltage can be calculated from the well known relationship:

$$\Delta G = -nF\varepsilon$$

where ΔG is the Gibb's free energy change of the reaction, F is the Faraday constant, n is the number of moles and ε is the corresponding cell voltage. In the following reaction:

$$Li_yV_2O_{5(s)} + xLi_{(s)} \leftrightarrow Li_{x+y}V_2O_{5(s)}$$

we approximate the free energy change (ΔG) with the internal energy change per intercalated lithium ion (ΔE), by taking the difference between the total energies of the reactants and the products:

$$\Delta G \approx \Delta E = (E_{PROD} - E_{REACT}) / \text{No. of lithium atoms}$$

This approximation excludes the effects of entropy. However, the contribution of the vibrational and configurational entropy terms to the cell voltage at room temperature is

expected to be small (<0.1V), and there is little change in volume during the intercalation (even so, we appreciate that this is a significant approximation).

We estimate the change in internal energy by calculating the total energy, E(x), of pure V_2O_5, six $Li_xV_2O_5$ phases, where x = 0.25, 0.5, 0.75, 1.0, 1.5 and 2.0, and the total energy of pure lithium metal E(Li). The change in the total energy of the system per intercalated lithium atom is given by:

$$\Delta E(x') = \{E(x_2) - [E(x_1) + (x_2 - x_1)E(Li)]\} / (x_2 - x_1)$$

where E(x) = total energy of $Li_xV_2O_5$, $x_2 > x_1$, and $x' = (x_1 + x_2) / 2$. It should be stressed that $\Delta E(x')$ leads to a predicted cell voltage which is an average value for all $Li_xV_2O_5$ compositions between x_1 and x_2. Also, the number of configurations, and therefore, the resolution of the calculated voltage curve, is limited by the size of the simulation cell that it is possible to use. Ideally, very small changes in composition should be used to calculate ΔG accurately, but this would require a very large cell and make the calculation unfeasible.

The results are summarised in Table 3.8, while calculated and experimental data are compared in Figure 3.16.

Composition	Internal Energy E(x) / eV
$Li_{(s)}$	-1.903
V_8O_{20}	-236.321
$Li_1V_8O_{20}$	-241.359
$Li_2V_8O_{20}$	-246.343
$Li_3V_8O_{20}$	-250.910
$Li_4V_8O_{20}$	-255.446
$Li_6V_8O_{20}$	-261.964
$Li_8V_8O_{20}$	-269.001

Table 3.8. Compositions and calculated internal energies used in the cell voltage calculation. Compositions refer to the formula of the full unit cell used in the simulations.

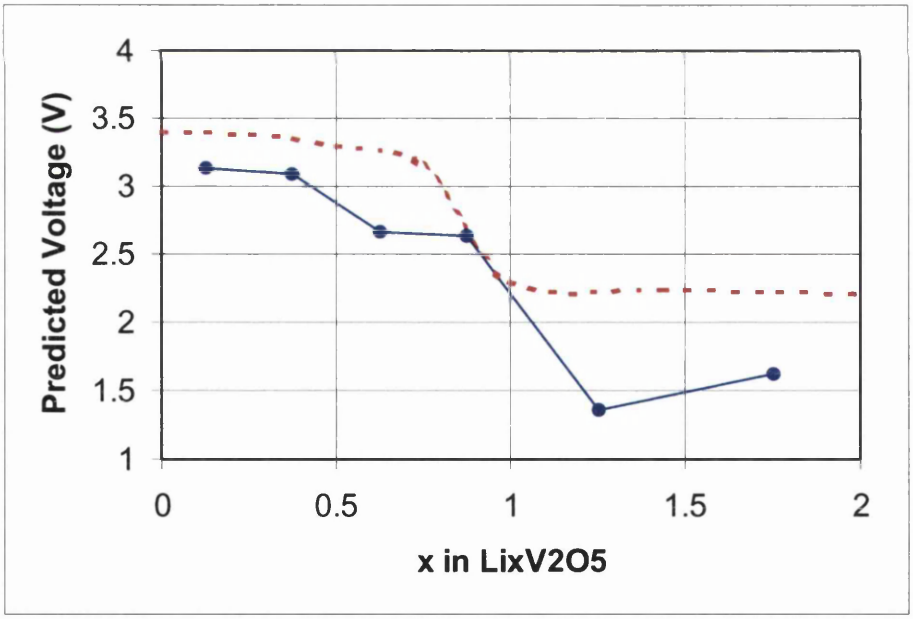

Fig.3.16. Calculated (solid blue) and experimental (West 1995) (dashed red) voltage curves for $Li_xV_2O_5$.

The predicted average cell voltages are in good general agreement with experimental values, although some consistent underestimation is observed. This underestimation of cell discharge voltages by DFT methods is also noted by Aydinol *et al* (1997a), where it

is felt that the main error comes from the overestimation of the binding energy for lithium metal. Aydinol *et al* have shown that, for transition metal oxides, total energies calculated using pseudopotentials to represent the nuclei and core electrons of the system are in good agreement with energies calculated using all electron methods.

We suggest that, in our work, the dominant source of the error between experimental voltages and theoretical values derived using DFT is also likely to be a result of the overbinding of lithium metal. While our simulations employ the gradient corrected local density approximation, which usually underestimates binding energies, we note a contraction of the face-centred unit cell of lithium metal of around 3% during geometry optimisation, while calculated cohesive energies are 0.3eV more than experimental values. When combined with a tendency to underestimate the binding energies of transition metal oxides, this effect accounts for the consistent small underestimation of experimental voltages by Density Functional methods.

Even though the resolution of the predicted curve is relatively low, it is still possible to see two plateaux emerging. The minimum at $x = 1.25$ is an artefact which almost certainly arises from the limited number of compositions which it is possible to simulate, although the structural rearrangement that occurs between $Li_{1.5}V_2O_5$ and $Li_{2.0}V_2O_5$ may be a factor.

Since the variation of the cell voltage with lithium concentration, x, is controlled by a complex interplay of electronic factors, it is gratifying that calculation and experiment are, on the whole, in such close agreement. Our results suggest that this type of

calculation may be used to model accurately the electrochemical properties of cathode materials for use in solid-state batteries.

3.4.6 Lithium Migration Processes

It has been noted in experimental studies that lithium migration takes place parallel to the *b* direction, along channels formed by the vanadyl bonds. This migration route has consequently been investigated using potential based static lattice simulation techniques.

To study the energetics of lithium mobility in V_2O_5, we have undertaken a series of bulk optimisations on intercalated V_2O_5. By constraining the position of the lithium atom by keeping its position in the *b* direction constant throughout the optimisation, it is possible to optimise the position of the ion in the *a-c* plane. By carrying out a series of calculations, with the Li^+ ion at different positions along the *b* cell parameter, it is possible to construct the potential energy path for the lithium ion as it moves along this axis.

One of the vanadium atoms in the bulk lattice must be reduced as the optimisation requires that the total charge on the cell is zero. If one lithium ion is incorporated per unit cell then there are two inequivalent V atoms in the crystal structure (V(1) and V(2) in Fig. 3.9), so an energy profile has been calculated for both choices of reduced cation. We also use partial occupancies to simulate the delocalisation of the electronic charge over both V(1) vanadium atoms. For each optimisation, which is carried out at constant volume, the initial position of the lithium in the *a* and *c* directions, before geometry

optimisation, is identical. Expressed as fractional co-ordinates these are 0.500 along *a* and 0.350 along *c*. It is necessary to constrain some of the vanadium atom positions to stop the whole of the bulk lattice moving relative to the lithium ion along the *b* lattice parameter during the optimisation. This is achieved by holding the position of one V atom constant in all directions, which effectively anchors the system, while all other vanadiums are constrained only along the *b* direction. Although we appreciate that this does prevent a full optimisation of the vanadium positions, we found it was the only way to stop the Li^+ ion from moving back to its most stable position during each optimisation. The predicted energy profiles are shown in Fig. 3.17 and the migration paths are given in Fig. 3.18.

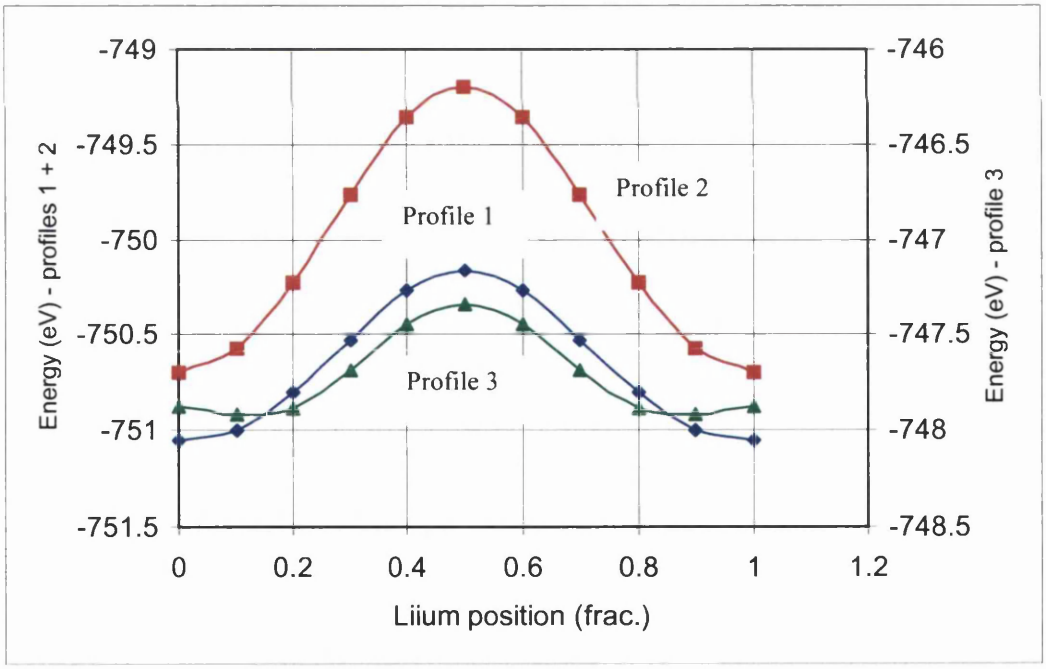

Fig. 3.17. Energy profiles for lithium migration through V_2O_5.

Note that profile 3 relates to a different energy scale, which is given to the right.

Profile 1 in red - reduced V(IV) species is V(1) at 0.351186 0.500000 0.891700

Profile 2 in blue - reduced V(IV) species is V(2) at 0.148812 0.000000 0.108300

Profile 3 in green – both V(1) species are partially reduces using partial occupancies.

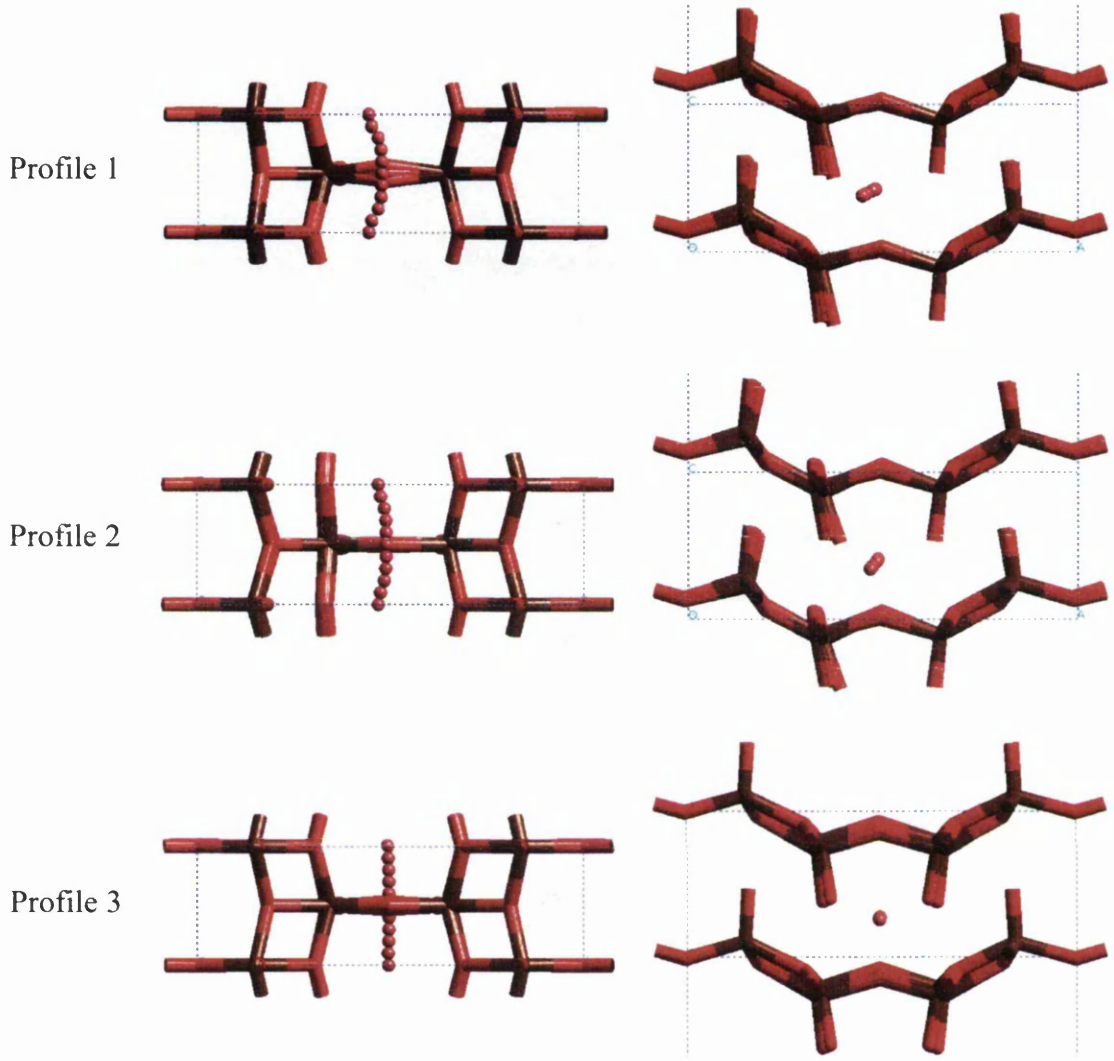

Fig. 3.18. Lithium migration paths through V_2O_5.

Each profile relates to the energy path detailed in Fig. 3.17.

We find that the position of the reduced vanadium centre has a significant effect on the energy profile of the lithium migration and the overall activation energy for the process. A lower activation energy, of 0.89eV compared to 1.49eV, is predicted when the V(IV) species is, on average, closer to the lithium ion, which can also be rationalised in terms of the distance between the Li^+ and the reduced vanadium ions. An even lower

activation energy, of 0.57eV, results if the electron accompanying the inserted lithium ion is delocalised over the two vanadium atoms which lie closest to the migration path.

The calculated activation energies suggest that lithium is highly mobile in V_2O_5, and that electrostatic effects play an important role in determining the size of the activation energy. In every migration path, the transition point occurs as the lithium ion passes between the vanadyl oxygens, while the energy minimum is dependent on the vanadium oxidation-states. When partial charges are used the minimum is shifted along the [*010*] direction, closer to the Li^+ position predicted by DFT than the original site located using the Mott-Littleton method. The actual route taken by the Li^+ ion is similar in all cases, although a curve appears in the migration path for profiles 1 and 2, caused by the V(IV) centre being to one side.

The findings from the atomistic calculations, that the activation energy of lithium migration through V_2O_5 is dependent on the position of the V(IV) centre in the lattice, is supported by the calculated electronic distribution in $Li_{0.5}V_2O_5$ from the DFT simulations. The electronic structure results indicate that there are two vanadium atoms, closest to the lithium path, which are reduced in preference to those further away. The atomistic simulation predicts a lower activation energy and a more accurate energy minimum if this is the case. The migration calculations indicate that charge distributions from high level calculations can be incorporated into an interatomic potential model to increase the accuracy of the atomistic method.

3.5 Summary

The first significant finding of this study is that atomistic defect calculations can be used to successfully locate stable, low energy, sites for intercalated lithium in the V_2O_5 lattice. The resulting lithium co-ordinates may be used to give the initial geometries for the electronic structure studies as we find that they give a good estimate of the lithium positions in the $Li_xV_2O_5$ phases ($x \leq 2$). Interatomic potential based modelling has also been used to show that lithium is mobile along the channel in the [*010*] direction in V_2O_5, with a calculated activation energy of 0.57eV, and that the use of partial charges, to imitate the electron distribution resulting from electronic structure calculations, reduces the activation energy of the migration process.

Our electronic structure calculations of the $Li_xV_2O_5$ system have produced structures that are in good agreement with experiment, and successfully predicted the evolution of the lattice parameters with lithium concentrations. The calculated total energies can be used to predict average cell voltages, which lead to an estimate of the shape of the discharge curve. Although there is only moderate agreement with the experimental voltage curve, we suggest that this is due to a lack of resolution, and does not indicate a failure of the DFT technique.

Our calculated charge density maps show that the vanadium centres are reduced during the intercalation reaction, and that, at low lithium concentrations, the additional electrons are localised on two metal atoms. The population of a delocalised band comprised of all the vanadium π-d orbitals does not occur. The calculated electron

densities suggest that intercalated lithium is fully ionised and that reduction of the vanadium centres leads to a weakening of the vanadyl bond - an effect that is reproduced in the calculated vanadyl bond lengths.

We note the success of combining interatomic potential based simulation with high quality electronic structure calculations when studying complex materials. Atomistic methods can be used to reduce the number of possible configurations of the system in a computationally efficient manner, while *ab initio* simulation allows the key elements of the problem to be studied in greater depth.

Chapter 4.

Lithium Intercalation into V_6O_{13}

4.1 Introduction

In this chapter we look at another vanadium oxide, the mixed valence V_6O_{13} which was first suggested as a possible cathode material by Murphy and co-workers (1979) and has been extensively studied since. Again we will use both electronic structure calculations and interatomic potential based simulation to study the electronic and structural changes that accompany lithium incorporation by the oxide.

4.2 The V_6O_{13} Structure

The crystal structure of V_6O_{13} was first determined by Aebi in 1948, and was refined in 1971 by Wilhelmi *et al* so that V-O bond lengths could be compared to other vanadium oxides with more accuracy. The oxide has a monoclinic unit cell and was found to have the space group *C2/m* (attempts were made to refine the structure with the space groups *Cm* and *C2*, but no significant differences in the structures were found). The V_6O_{13}

structure is made up of three unique vanadium atoms, each surrounded by a distorted octahedron of oxygens.

The VO_6 octahedral arrangement in V_6O_{13} can be related to the structure of V_2O_5, if octahedral co-ordination within the layered oxide is assumed. It is convenient to discuss the structure in terms to two separate elements, the first containing the V(1) atom, while the second element consists of V(2) and V(3). Each element forms a sheet of VO_6 octahedra in the *ab* plane, which form a three dimensional lattice by corner sharing along the [*001*] direction, in an ABAB arrangement.

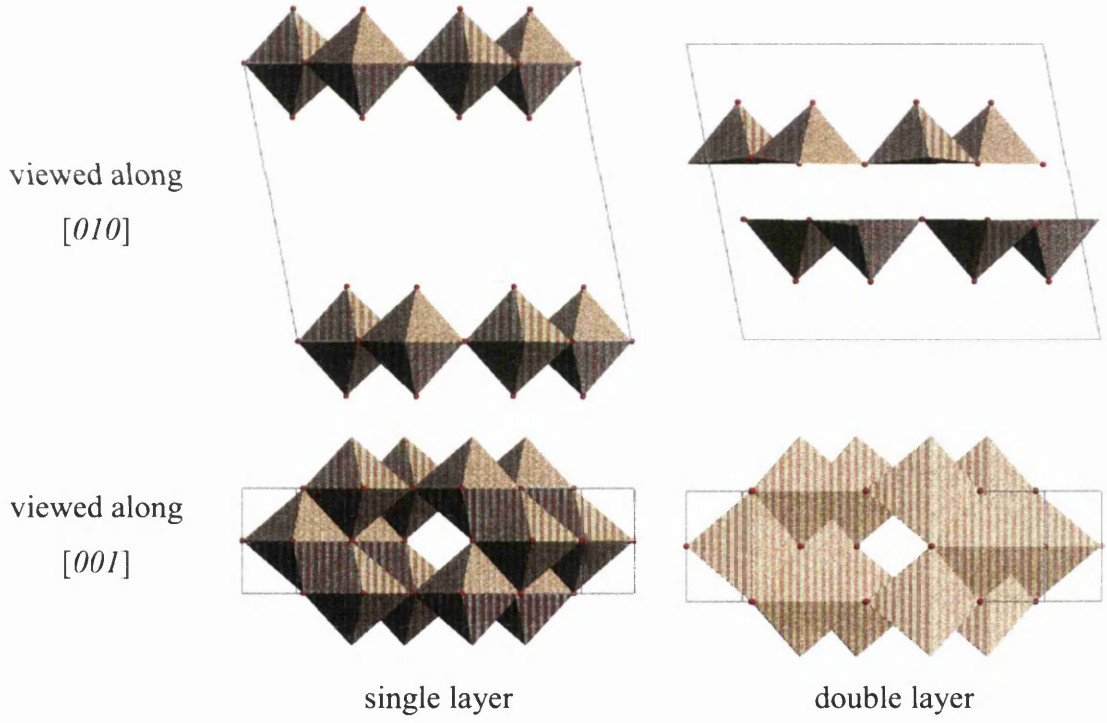

Fig. 4.1. The two structural elements in V_6O_{13}.

The first structural element, containing V(1), is essentially identical to a single layer of the V_2O_5 structure, where octahedra are connected by edge sharing along the *b*-axis and

alternate edge and corner sharing along *a*. V(2) and V(3) also each form a 'V_2O_5-like' layer of octahedra in the second element, but the V(2) and V(3) layers are displaced relative to each other along [*100*], producing a shear structure where the octahedra are joined by edge sharing instead of corner sharing. This double layer contains a V:O ratio of 1 to 2, and therefore resembles the structure of VO_2.

The distortion of the VO_6 octahedra in both elements is caused by electrostatic repulsion between neighbouring vanadium centres, as the movement of the V atoms away from the centre of the oxygen octahedra leads to an increase in the V-V distance. The V_6O_{13} structure gives rise to V-O bond lengths that vary from 1.64 to 2.28Å, an unusually wide range within a single material. The structure cannot be described as layered in the same way as V_2O_5, as the long V-O bond distance in V_6O_{13} is considerably shorter (2.27Å, compared to 2.79Å), which will lead to a bond that is much stronger than the simple ionic interaction in V_2O_5.

V_6O_{13} contains four cavities per unit cell, shown in Fig. 4.2, which lie between the V(1) layer and the V(2) - V(3) double layer. These cavities are joined along the [*010*] direction by sharing a square face, consisting of a four-vanadium ring, through which lithium ions are thought to diffuse (West 1985). Pairs of these cavities are also joined by sharing a square face along the [*001*] direction, although it has been reported that lithium diffusion does not occur along this direction.

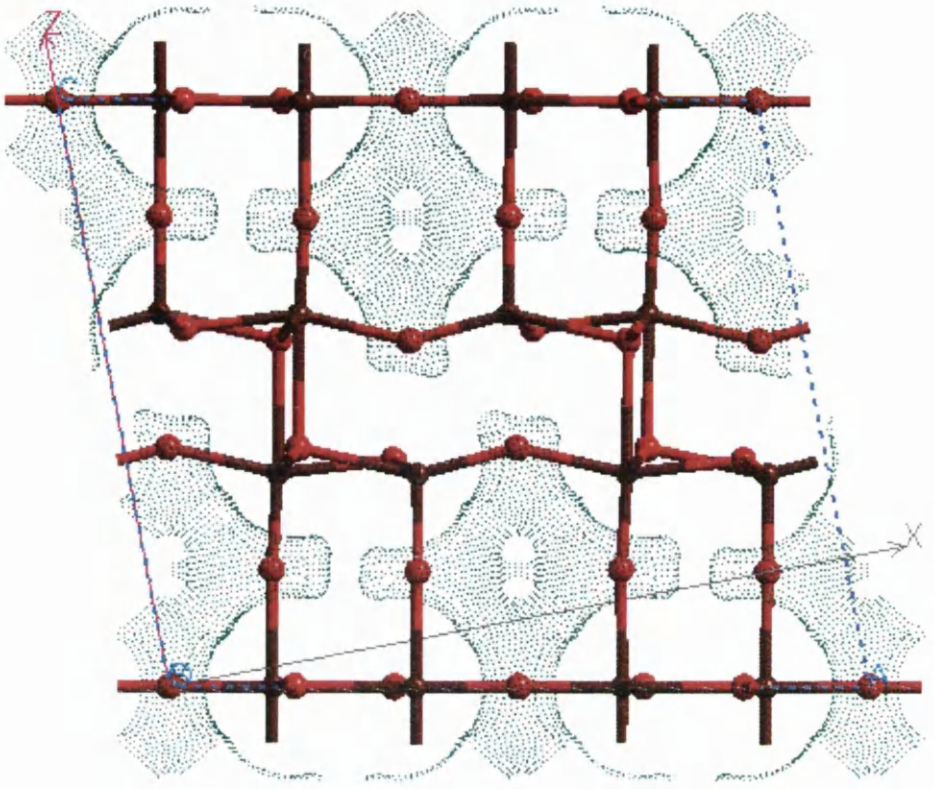

Fig. 4.2. Measuring the 'void space' in V_6O_{13} using covalent radii, indicates the shape of the cavities. Viewed along the [*010*] direction.

4.3 Experimental Background

Murphy *et al* found in 1979 that V_6O_{13}, prepared from the thermal decomposition of NH_4VO_3, has an electrochemical intercalation limit of about 1 Li per V atom, while chemical lithiation with n-BuLi in hexane gave a Li/V ratio of about 1.25. Little change in the properties of the cell was seen after 15 discharge/recharge cycles. The maximum lithium up-take of $Li_8V_6O_{13}$ and the average cell voltage of 2.2 volts were used to calculate a large theoretical energy density of 800Wh/kg although it was accepted that, as the conductivity of $Li_xV_6O_{13}$ was found to decrease rapidly as the lithium content increased (x>4) (see Fig. 4.3), the addition of a suitable conducting material, such as

graphite, to the cathode would reduce this figure. At the time, this energy density compared favourably to other cathode materials (for example, Whittingham in 1976 calculated the corresponding figure for TiS_2 as 490Wh/kg), which helped to create a wider interest in the material.

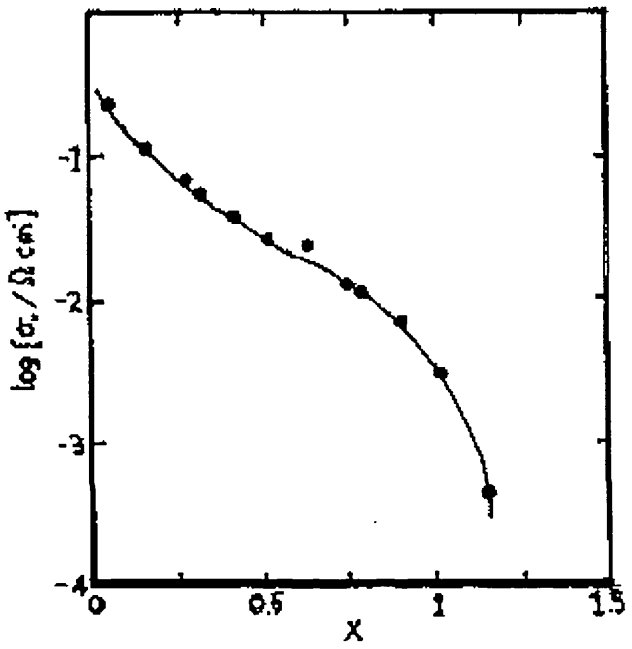

Fig. 4.3. Electronic conductivity of $Li_xVO_{2.144}$ as a function of lithium composition (West 1983)

Based on cyclic voltammetry studies, West *et al* (1985) proposed that lithium insertion into V_6O_{13} occurs in three stages, as there are three plateaux on an e.m.f. versus composition curve. The first at 2.75V corresponds to the insertion of 1 Li atom per V_6O_{13} unit, the second at 2.55V to 3 Li atoms, and the third at 2.15V to 4 Li atoms per V_6O_{13}. This gives a total of 8 intercalated lithium atoms per formula unit in the fully discharged cell.

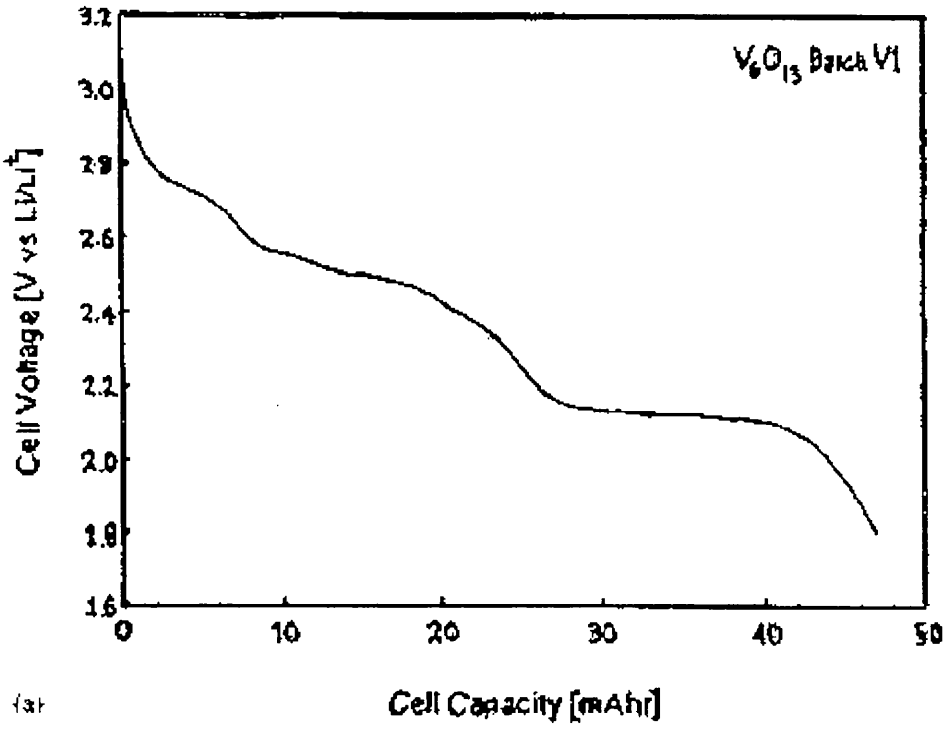

Fig. 4.4. Experimental voltage discharge charge curve for $Li_xV_6O_{13}$ (Barker 1996)

It is suggested that the Li atoms occupy two different types of site in the fully lithiated material. The first is a square pyramidal site that is situated within the cavity described above, close to the double 'VO_2' layer, which leads to the highest possible oxygen to lithium co-ordination of 5. The other proposed site is the square face that joins the cavities to each other, which allows co-ordination to 4 oxygens. Square pyramidal co-ordination of lithium has been shown to be present in $Li_2V_6O_{13}$ from a recent single crystal X-ray diffraction study by Bergström *et al* (1997). They find that, for $Li_2V_6O_{13}$, all the lithium ions occupy symmetry-equivalent sites within the lattice. A comprehensive study of the cycling properties of the Li/V_6O_{13} cell was also carried out, where it was found that cell capacity dropped rapidly during the first ten cycles (from 7.2 e^- per V_6O_{13} to 3.6 e^- per V_6O_{13}) but then only small amounts of capacity were lost in subsequent cycles up to 100.

More recent studies have shown that the intercalation process may be more complex than the three plateaux relationship given above. One reports at least six distinctive peaks in the differential capacity profile (a plot of dQ/dV against cell voltage) of a Li/V_6O_{13} cell, indicating at least six inequivalent Li sites in V_6O_{13} (Barker 1996). Bergström *et al* (1998b) have measured the cell discharge curve in great detail (Fig. 4.5), and show that the curve exhibits a number of smaller steps and plateaux.

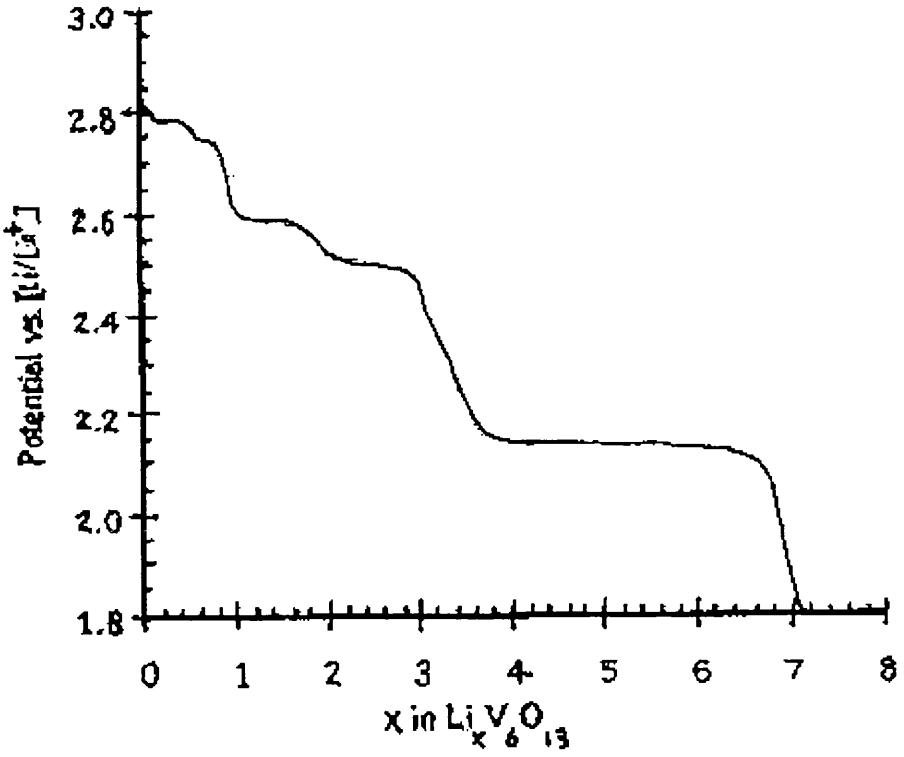

Fig. 4.5. Cell potential against cell capacity curve for V_6O_{13}. (Bergström 1998b)

The capacity loss that is experienced after extensive cycling has been investigated in detail by Barker *et al* (1995). They run a cell through 250 discharge/recharge cycles and then carry out an X-ray powder diffraction experiment on the V_6O_{13} in the used cell. Little change was found in the unit cell parameters, indicating that the vanadium oxide

structure had remained essentially intact even though the unit cell volume changes by about 16% during each cycle (Murphy 1979). The loss in cell capacity of about 25% was blamed on loss of electrical contact between particles in the cathode, possibly caused by the mechanical effects of the repeated changes in cell volume during the cycling.

The exact stoichiometry of the vanadium oxide has an important effect on the performance of a Li/V_6O_{13} cell. West *et al* (1983) have carried out intercalation reactions with a range of oxide with slightly different V:O ratios. They found that the maximum Li uptake in each sample corresponded to a complete reduction of all vanadium to V(III). This indicates that the amount of lithium that is incorporated into the oxide is limited by the number of electronic states, and not by the number of lithium sites available. Therefore, the capacity of the cell is determined by the stoichiometry of the cathode material used.

We make use of interatomic potential based modelling and electronic structure techniques to investigate the positions adopted by intercalated lithium ions, the effects that lithium incorporation has on the atomic and electronic structure of V_6O_{13}, and theoretical predictions of the resulting cell voltage.

4.4 Potential Model Of V_6O_{13}

As V_6O_{13} is a mixed valence transition metal oxide, with an average vanadium oxidation-state of 26/6 or $4\frac{1}{3}$, then an atomistic model needs to include both V(V) and V(IV) species in the ratio 1:2, respectively. If the use of partial charges on the vanadium

atoms is to be avoided then an assignment of the vanadium oxidation-states has to be made on the basis of the V_6O_{13} structure. Although there are three unique vanadium positions in the lattice, the two structural elements described earlier divide the vanadium atoms into two groups, in the ratio of 1:2. The single chain element has a higher oxygen to vanadium ratio, and is therefore best assigned as containing the V(V) centres. The double chain element, which contains twice as many metal atoms, is, as a result, represented as V(IV). This model agrees with the structural description by West *et al* (1985), of V_6O_{13} as alternate 'VO_2' and 'V_2O_5' like layers.

It should also be possible to assign the vanadium oxidation-states by studying the local co-ordination around each metal centre. Due to the effect of the crystal field around each vanadium atom, it is expected that the V(V) centre should have a more asymmetric local co-ordination sphere, with an unusually short V-O bond, as in V_2O_5. In fact, both V(2) and V(3) have more uneven VO_6 octahedra than V(1), although all three vanadium atoms have a range of V-O bond lengths. As this makes it difficult to assign a single V atom as V(V), we have proceeded by using the model described in the previous paragraph, where the assignment of formal charges is made on general structural grounds.

4.4.1 Fitting A New V(IV)-O Potential

Now that we have decided on a division of the vanadium centres into formal V(IV) and V(V), it is clear that two separate V-O interatomic potentials will be required, one for each vanadium species. Initially, the V(V)-O potential will be taken from the force-field for V_2O_5, while a new V(IV)-O interatomic potential will be derived by empirically fitting to the VO_2 structure.

4.4.1.1 The VO_2 Structure

Two VO_2 phases were used to derive the new V(IV)-O potential: the low temperature monoclinic and the high temperature tetragonal. The phase transition is reported to occur around 68°C (Westman 1961). Both structures were obtained from the Inorganic Crystallographic Structure Data File (ICSD) at Chemical Database Services, based at the Daresbury Laboratory (Fletcher 1996), although the original structures are due to Rogers (1996). The high temperature phase, α-VO_2, was first described by Goldshmidt (1926) as having a rutile like structure with an *a/c* ratio of 1.58 while Andersson reported, in 1956, that at lower temperatures the structure is distorted to monoclinic, β-VO_2. The crystallographic data from these structures has not been used in the fitting procedure because the reported reliability factors, R, of 10-12% were higher than those for the more recent structures available through the Inorganic Crystal Systems Database (ICSD) (3.80% and 3.60% for the α and β phases respectively). The crystal structures of both phases are shown in Fig. 4.6.

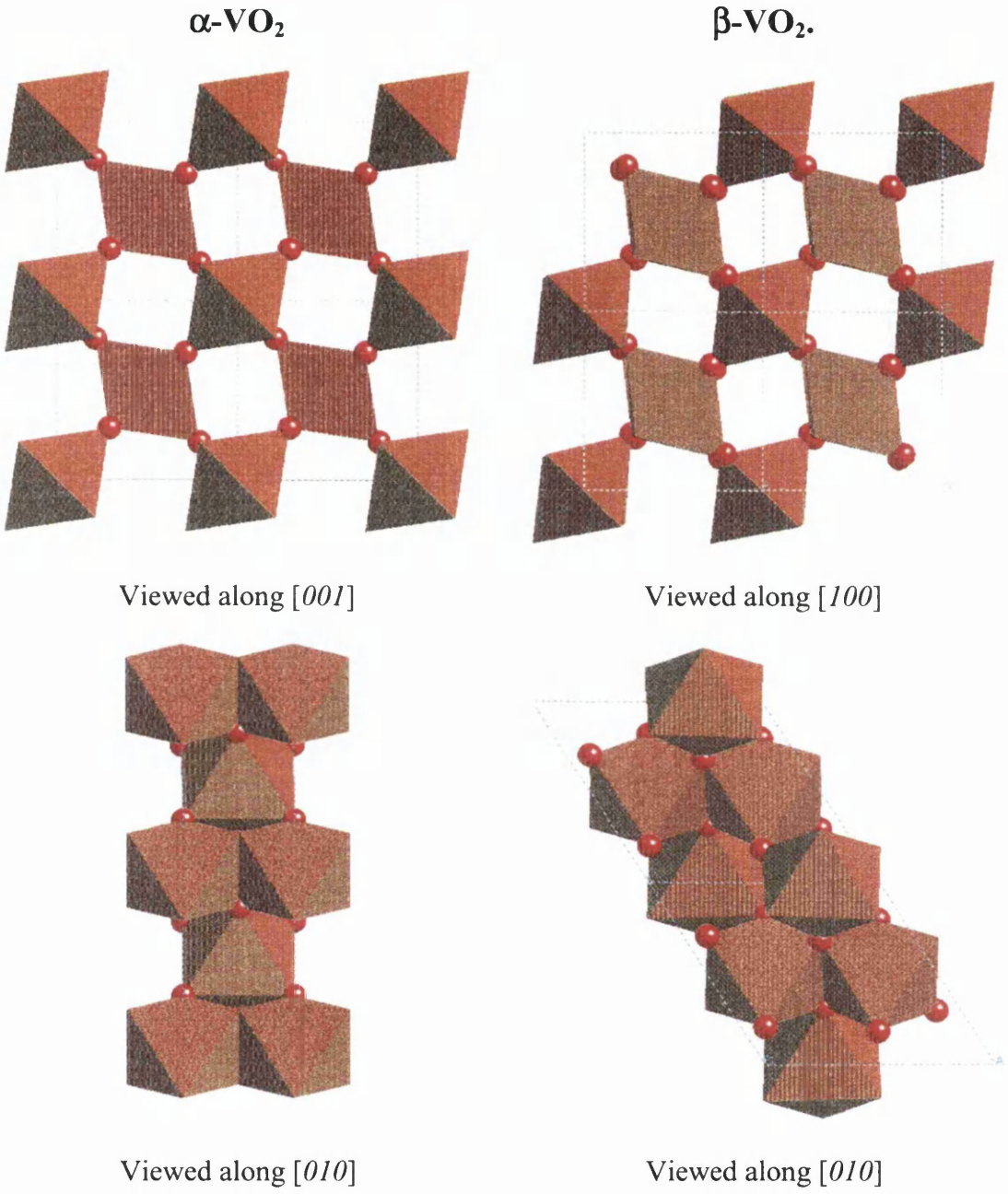

Fig. 4.6. Crystal structure of α-VO_2 and β-VO_2.

Dielectric constants were found for both phases and are given in Table 4.1. The high frequency data is unusually high for transition metal oxides.

	Dielectric Constants	
	High freq.,ε_∞	Static,ε_0
α-VO_2 $\parallel$ to c	9.0	35
β-VO_2 $\parallel$ to a	9.7	25.9
β-VO_2 $\perp$ to a	10.0	40.6

Table 4.1. Dielectric constants for VO_2 (Mansingh 1984 and Baker 1966).

4.4.1.2 Empirical fitting to the α-VO_2 structure.

The vanadium atoms are represented as point charges. There is no attempt to represent their polarisability in the lattice as this will be small due to the small radius and high charge of vanadium ions. The oxygen atoms are represented initially using the shell model with a shell charge of -2.717e and a spring constant of 54.952, values that are taken from a theoretical study of V_2O_5 by Dietrich *et al* (1993). The short-range forces between all oxygen atoms are modelled using a Buckingham potential from a study by Catlow on UO_2 (1977), which has also been used in a atomistic study of V_2O_5 (Dietrich 1993). Although it is possible to fit to more than one structure simultaneously, the initial fitting has been carried out separately on each structure.

The rutile structure of TiO_2 cannot be modelled successfully with a simple pair potential shell model, such as the one outlined above. It has proved to be impossible to reproduce accurately the structure and properties simultaneously, although this problem can be overcome by using a three-body term in the potential model.(Tomlinson 1989). Errors of around 10% for the a/c ratio are usually the best that can be obtained. This problem

was encountered during the fitting of the α-VO_2 structure, as it proved impossible to accurately reproduce the *a* and *c* parameters simultaneously. While it is possible to derive potential models that will reproduce either cell parameter correctly at the expense of the other, we consider that the best fit is given by a potential that shares the error between all the unit cell dimensions. This results in the cell volume, if not the cell shape, being calculated correctly.

Initially, the unit cell would often collapse during the fitting procedure, and it proved impossible to produce an acceptable fit until the C parameter of the O-O Buckingham potential was reduced to zero, which stopped the overestimation of the attractive forces within the crystal. Removing all the symmetry constraints from the model does not effect the quality of the fit or the stability of the optimised structure. The final potential model for α-VO_2 is given in Table 4.2 and the optimised structure and properties are shown in Table 4.3 and 4.4.

Interaction	A / eV	ρ / Å	C / eVÅ^6	Y / e	k / eVÅ^{-2}
αV(IV)-O	949.26	0.35668	0.00	-	-
O-O	22764.30	0.14900	0.00	-2.72	46.67

Table 4.2. Final Buckingham potential and shell model parameters for α-VO_2

Parameter	Experimental	Calculated	Error (%)
Cell Volume / Å^3	59.22	59.51	0.49
a / Å	4.554	4.418	-3.00
b / Å	4.554	4.418	-3.00
c / Å	2.856	3.050	6.79
O position	0.2883	0.3099	-

Table 4.3. Calculated structural parameters for α-VO_2.

Lattice Energy / eV	-235.16
$\varepsilon_0 \parallel$ to *a*	37.9
$\varepsilon_0 \parallel$ to *c*	16.1 (35)
$\varepsilon_\infty \parallel$ to *a*	3.49
$\varepsilon_\infty \parallel$ to *c*	3.50 (9)
C_{11} / dyne cm^{-2}	28.1
C_{66} / dyne cm^{-2}	23.7

Table 4.4. Calculated physical data for α-VO_2. Experiment data appears in brackets.

Within the limits of the model, the structure is reproduced acceptably, while the physical properties of the lattice are not so successful. The high frequency static dielectric constants that have been measured experimentally are unusually large, a result of electronic effects that cannot be modelled at this level of theory. The static dielectric values are disappointing, as better agreement should be expected, even with this type of simple potential model.

4.4.1.3 Empirical fitting to the β-VO_2 structure.

To test the transferability of the α-V(IV)-O potential, we attempted to optimise the structure of the low temperature VO_2 phase, β-VO_2, using the α-VO_2 potential force-field, detailed in Table 4.2. The resulting structure and properties are given in Tables 4.5 and 4.6.

Parameter	Experimental	Calculated	Error (%)
Cell Volume / Å^3	118.07	119.03	0.81
a / Å	5.753	6.099	6.02
b / Å	4.526	4.417	-2.40
c / Å	5.383	5.368	-0.27

Table 4.5. Calculated structural parameters for β-VO_2.

Lattice Energy / eV	-470.32
$\varepsilon_0 \parallel$ to *a*	16.1 (25.9)
$\varepsilon_0 \perp$ to *a*	37.9 (40.6)
$\varepsilon_\infty \parallel$ to *a*	3.50 (9.7)
$\varepsilon_\infty \perp$ to *a*	3.49 (10.0)
C_{11} / dyne cm^{-2}	63.9
C_{66} / dyne cm^{-2}	7.9

Table 4.6. Calculated physical properties for β-VO_2. Experimental data appears in brackets.

Although the *a* lattice parameter is overestimated, we find that the optimised structure is stable and relatively accurate, while the calculated properties are reasonable and, although only experimental values are available for the static dielectric constant, agreement, in this case, is good. Further fitting of the potential model resulted in small improvements in the optimised structure.

Finally, we attempted to generate a more transferable potential by simultaneously fitting to the structures of both phases. It was found that reasonable reproduction of both structures with the same V(IV)-O potential was possible (Table 4.7), although calculated properties tended to be worse. The resulting potential parameters are given in Table 4.8.

	Parameter	Experimental	Calculated	Error (%)
α-VO_2	Cell Vol. / $Å^3$	59.22	57.14	-3.51
	a / Å	4.554	4.389	-3.63
	c / Å	2.856	2.967	3.89
β-VO_2	Cell Vol. / $Å^3$	118.07	114.29	-3.21
	a / Å	5.753	5.934	3.14
	b / Å	4.526	4.389	-3.04
	c / Å	5.383	5.297	-1.58
	β / °	122.6	124.1	1.19

Table 4.7. Comparison of optimised and experimental structures for both phases of VO_2, when interatomic potentials were fitted simultaneously.

Interaction	A / eV	ρ / Å	C / eVÅ^6	Y / e	k / eVÅ^{-2}
V(IV)-O	828.256	0.36282	0.00	-	-
O-O	22764.30	0.14900	0.00	-2.717	56.669

Table 4.8. Potential force-field derived from the simultaneous fitting of both VO_2 phases.

4.4.2 Transfer Of V(IV)-O Potential To V_6O_{13}

The potential model for V_6O_{13} was constructed from the V(IV)-O potential fitted simultaneously to both phases, described in the previous section, and the V(V)-$O_{equatorial}$ potential from Dietrich *et al.*[7] The O-O potential, oxygen core-shell charges and spring constant were the same as those used in α-VO_2. The initial attempt at optimisation of V_6O_{13} failed as the unit cell appeared to collapse during the calculation. The interatomic potentials used were too attractive. The Buckingham potential that models the short range forces between the V(V) and O ions decays very rapidly (as ρ is small) and could lead to V-O bonds that are too short. The transferability of this potential was questioned by the authors (Dietrich 1993) as it is part of a specific model that is set up to reproduce the layered structure of V_2O_5, and may not be suitable to use in models of other vanadium oxide systems. This appears to be the case for V_6O_{13}.

Although reasonable structural data was found for V_6O_{13}, which has been discussed earlier, physical properties such as dielectric constants could not be found, which means that the empirical fitting carried out on V_6O_{13}, has been undertaken using structural information only, although the situation is improved since V_6O_{13} has a relatively complex structure with a wide range of V-O distances.

4.4.3 Empirical Fitting To The V_6O_{13} Structure

To obtain a reasonable model, a new V(V)-O potential was empirically derived by fitting to the experimental structure of V_6O_{13}. However, with failed to produce a stable structure that accurately reproduced the experimental data. All three lattice parameters were in error by approximately 8% for the most successful optimised structure that could be obtained. This left few options but to fit both V-O potentials simultaneously, using the old potentials as starting values. During the fitting process, the O-O potential C parameter and the oxygen core-shell spring constant were both adjusted to improve the cell parameters, especially along the *b* direction. The final potential model for V_6O_{13} is given in Table 4.9 and the resulting optimised structure and properties are shown in Tables 4.10 and 4.11.

Interaction	A (eV)	ρ (Å)	C (eVÅ^6)	q_{core} (e)	k (eVÅ^{-2})
V(V)-O	6870.52	0.24327	0.0	-	-
V(IV)-O	1290.56	0.34039	0.0	-	-
O-O	22764.30	0.14900	0.0	+0.717	67.30

Table 4.9. Final interatomic potential parameters for V_6O_{13}.

	Experimental	Calculated	Error (%)
Cell Volume ($Å^3$)	436.80	425.18	-2.66
a(Å)	11.922	11.991	0.58
b (Å)	3.680	3.547	-3.63
c (Å)	10.138	10.110	-0.28
β (°)	100.87	98.54	-2.31

Table 4.10. Calculated structure parameters for V_6O_{13}.

Lattice Energy(eV)	-1689.99
$\varepsilon_0 \parallel$ to *a*	18.3
$\varepsilon_0 \parallel$ to *b*	8.27
$\varepsilon_0 \parallel$ to *c*	5.73
$\varepsilon_8 \parallel$ to *a*	2.18
$\varepsilon_8 \parallel$ to *b*	2.23
$\varepsilon_8 \parallel$ to *c*	2.04
C_{11}(dyne cm^{-2})	68.62
C_{66}(dyne cm^{-2})	4.932

Table 4.11. Calculated physical properties of V_6O_{13}.

The calculated structure is in good agreement with the experimental data apart from the unit cell dimension along the *b* axis, which was consistently the most difficult parameter to fit to. Although the error could be reduced by increasing the Buckingham A parameter of the O-O potential, which effectively increases the O-O repulsion and

expands the unit cell, this change led to an increasingly bad fit along the *a* and *c* directions. The physical properties could not be compared to literature values as none were found, but all calculated dielectric and elastic constants give physically sensible values.

The calculated and experimental bond lengths are compared in Table 4.12, which shows that they are in moderate agreement. The range of different V-O bond lengths for each vanadium centre is well reproduced apart from the long bonds that are considerably greater then 2 Å. The V-O potentials seem to overestimate the attractive forces at this distance. The local co-ordination around V(V) is not as well reproduced as it is around the V(IV) centres. Considering the simplicity of the model, where only two potentials are used to represent all the V-O short-range interactions, the general agreement is acceptable and sufficient for the purposes of this study.

Bond	Experiment / Å	Calculated / Å	Difference / Å
V_{11}-V_{11}	3.047 (2)	3.057	-0.010
V_{21}-V_{31}	3.009 (1)	3.145	-0.136
V_{11}-O_{41}	1.766 (1)	1.753	0.013
V_{11}-O_{14} (x2)	1.876 (1)	1.866	0.010
V_{11}-O_{51}	1.964 (5)	1.709	0.255
V_{11}-O_{61}	1.993 (4)	1.714	0.279
V_{11}-O_{11}	2.064 (4)	1.909	0.155
V_{21}-O_{51}	1.655 (5)	1.784	-0.129
V_{21}-O_{71}	1.761 (4)	1.818	-0.057
V_{21}-O_{23} (x2)	1.902 (1)	1.870	0.032
V_{21}-O_{32}	2.084 (4)	2.155	-0.071
V_{21}-O_{72}	2.277 (5)	2.380	-0.103
V_{31}-O_{61}	1.641 (4)	1.775	-0.134
V_{31}-O_{33} (x2)	1.919 (1)	1.901	0.018
V_{31}-O_{72}	1.928 (4)	1.830	0.098
V_{31}-O_{22}	1.981 (4)	2.037	-0.056
V_{31}-O_{32}	2.261 (4)	2.583	-0.322

Table 4.12. Comparison of bond lengths in V_6O_{13}.

When a comparison is made between the V-O potentials that resulted from the simultaneous fitting of the VO_2 structures and the empirical fitting of the V_6O_{13} structure, the reasons for the lack of transferability of the potential between the oxides is clear. Figure 4.7 shows that they have a significantly different profile and, consequently, give quite different values for the short-range forces at typical V-O distances. The initial collapse of the V_6O_{13} structure when optimised with the VO_2 and V_2O_5 potentials

clearly results from an underestimation of the V-O repulsion, which is corrected in the potential set fitted to V_6O_{13}.

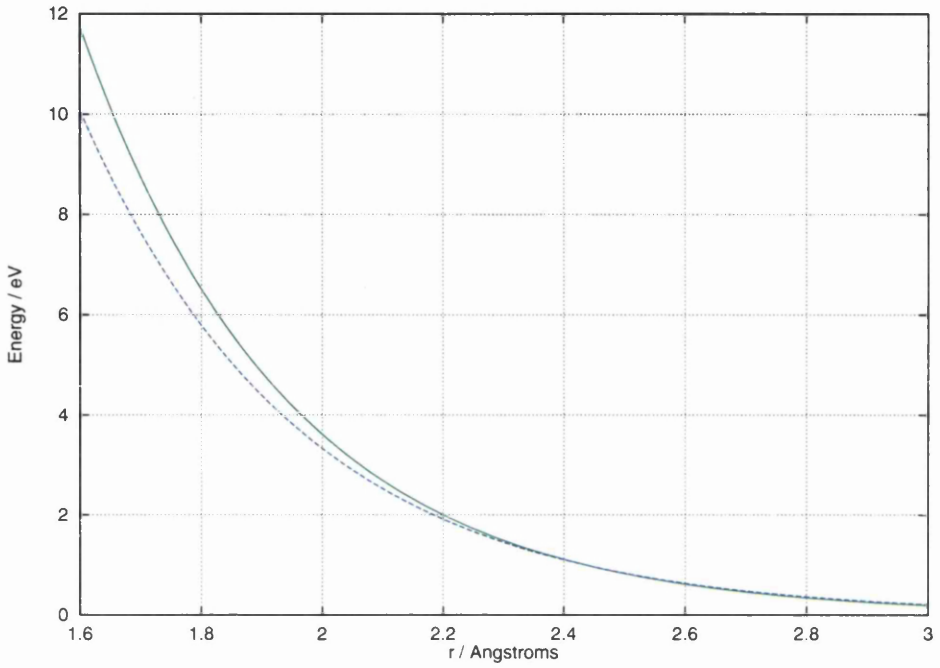

Fig. 4.7. V(IV)-O potentials, fitted to the VO_2 structures (blue) and fitted to the V_6O_{13} structure (green).

4.5 Results and Discussion

4.5.1 Lithium Defects In V_6O_{13}

A series of Mott-Littleton calculations has been carried out to establish the most stable sites for Li^+ ions in the V_6O_{13} lattice. The calculations employ standard techniques that have already been discussed in previous chapters and have been shown to provide useful information on the location of lithium ions in V_2O_5. The radius of the explicitly relaxed region I has been chosen as 8.0Å, which contains over 300 atoms, and is large enough to ensure the convergence of the defect energy with region size.

A number of stable sites have been found within the host lattice, which are shown graphically in Fig. 4.8, while their co-ordinates and defect energies are given in Table 4.13.

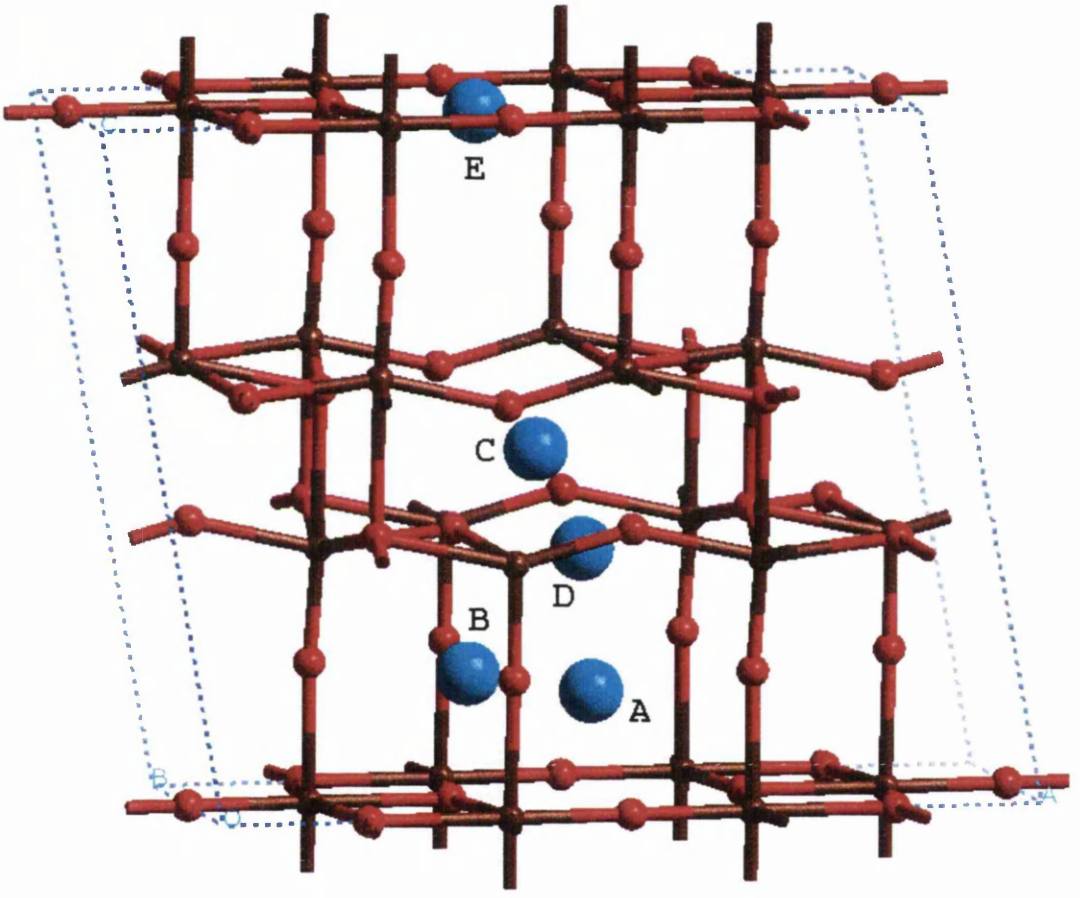

Fig. 4.8. Optimised Li^+ defect positions in V_6O_{13}. Labels relate to Table 4.13.

Defect Site	Fractional Co-ordinates	Defect Energy / eV
A	0.5158 0.5000 0.1484	-7.4779
B	0.3689 0.5000 0.1784	-5.7332
C	0.5008 0.5000 0.04979	-5.6321
D	0.5648 0.5000 0.3532	-4.7621
E	0.4980 0.5000 0.9998	-4.9668

Table 4.13. Calculated lithium ion defect energies and co-ordinates in the V_6O_{13} lattice.

Although there are several sites for intercalated Li^+ ions within the V_6O_{13} lattice, site A is found to be significantly lower in energy than the others, and is expected to be the favoured site for Li^+ insertion until fully occupied. The remaining sites all have defect energies that are within 1eV of each other. Therefore, it is not easy to predict which site will be occupied next. It is likely that other factors, such as the distance between neighbouring Li^+ ions, and the proximity of V(IV) centres, will play an important role in determining which of these sites are occupied at higher lithium concentrations.

4.5.2 Atomistic Geometry Optimisation of $Li_xV_6O_{13}$

4.5.2.1 Structure Prediction

In the previous chapter we described the difficulties encountered when trying to model the reduction of V(V) to V(IV) during the simulation of a number of $Li_xV_2O_5$ phases. The reduction of the host lattice did not present the same kind of problem in $Li_xV_6O_{13}$, as V(IV) centres are already present within the formal charge model that was used, and the V(IV)-O potential has already been fitted to the oxide structure. This made reducing

the V(V) centres to V(IV) a relatively simple process. A 1 x 2 x 1 supercell was used as the simulation cell, which allows us to study compositions with very low lithium concentrations and facilitates an even distribution of lithium ions along each crystallographic axis.

The initial geometries of the lithiated phases are constructed from our knowledge of the stable sites occupied by the intercalated lithium ions, provided by the Mott-Littleton calculations described earlier. As the most stable Li^+ site is eight-fold degenerate, a number of different lithium ion arrangements exist for intermediate levels of intercalation. The number of configurations of the system is further increased when the positions of the reduced vanadium centres are considered. A number of geometry optimisations were carried out for each $Li_xV_6O_{13}$ phase, to establish the most stable arrangement of Li^+, V(V), and V(IV) ions. The optimised lattice energy for the most stable configuration for each $Li_xV_6O_{13}$ phase is shown in Table 4.14, while the optimised geometries are compared to experiment in Table 4.15.

Phase	Lattice Energy (eV)
V_6O_{13}	-3379.98
$Li_{0.25}V_6O_{13}$	-3323.73
$Li_{0.5}V_6O_{13}$	-3268.75
$Li_{1.0}V_6O_{13}$	-3153.90
$Li_{1.5}V_6O_{13}$	-3037.52
$Li_{2.0}V_6O_{13}$	-2919.20

Table 4.14. Lattice energies of a series of geometry optimised $Li_xV_6O_{13}$ phases using a 1x2x1 supercell.

The arrangement of intercalated lithium ions was much as expected, with the most stable arrangement maximising the distance between the ions. We also expected that the reduction of vanadium centres close to the intercalated lithium ions would lead to the most stable configuration for a given Li^+ concentration, which proved to be incorrect in $Li_{0.25}V_6O_{13}$, where the newly formed V(IV) ion was as far as possible from the Li^+ ion in the most stable arrangement. In the more lithium rich phases, the most stable ionic arrangement occurred when the ring of four vanadium atoms that separates the lithium sites, consisted of alternate V(V) and V(IV) species, an arrangement that maximises the distance between neighbouring V(V) atoms.

x in $Li_xV_6O_{13}$	Calculated				Experiment			
	a / Å	*b* / Å	*c* / Å	β / °	*a* / Å	*b* / Å	*c* / Å	β / °
0.00	11.99	7.09	10.11	98.5	11.92	7.36	10.14	100.9
0.25	12.14	7.13	10.09	99.3	-	-	-	-
0.50	12.33	7.16	10.07	100.2	11.89	7.37	10.4	101.1
1.00	12.46	7.27	10.06	101.0	11.85	7.38	10.48	101.2
1.50	12.61	7.29	10.13	101.2	-	-	-	-
2.00	12.69	7.31	10.26	101.1	11.86	7.33	10.89	100.4

Table 4.15. Calculated and experimental (Bergström 1997, 1998b) structures for $Li_xV_6O_{13}$.

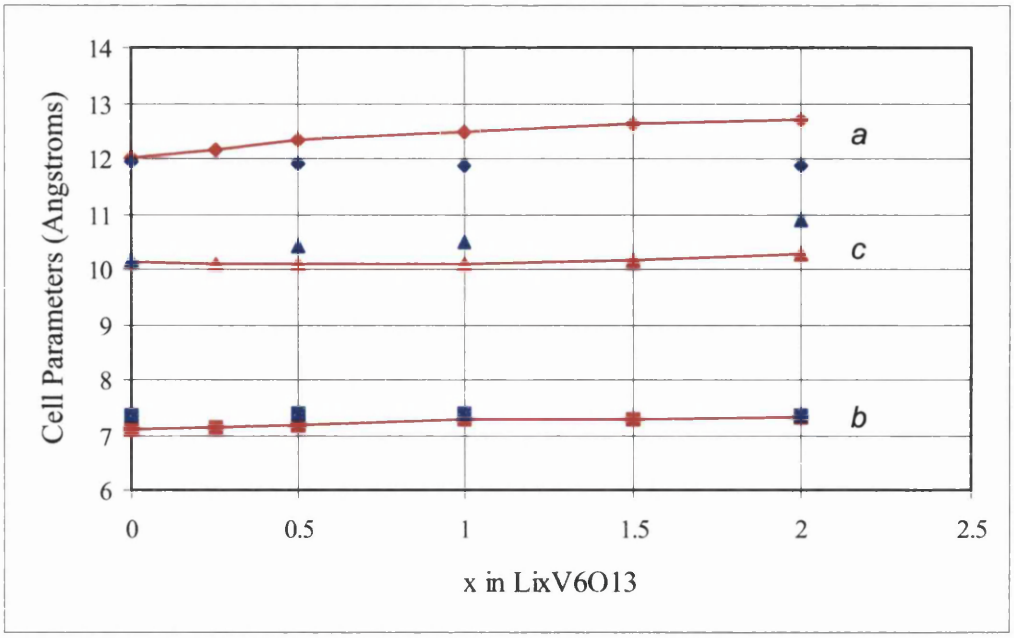

Fig. 4.9. Calculated (red) and experimental (blue) (Bergström 1997, 1998b) unit cell parameters versus lithium content.

We note that during the geometry optimisation, the Li^+ ions remain in the interstitial sites that were predicted by the Mott-Littleton calculations, while there is relatively little disruption to the host oxide structure. A comparison of the calculated and experimental unit cell dimensions in Fig.4.9 shows that there is general agreement between the two. The potential model is unable to reproduce exactly the effect that lithium intercalation has on the cell shape, particularly along the *a* parameter, although, at such low lithium concentrations, the magnitude of these changes is small.

4.5.2.2 Calculated Cell Potentials

The energy changes that occur as the concentration of intercalated lithium is increased can be calculated by using the simple Born-Haber cycle shown in Fig 4.10, which leads directly to an estimate of the cell voltage versus metallic lithium.

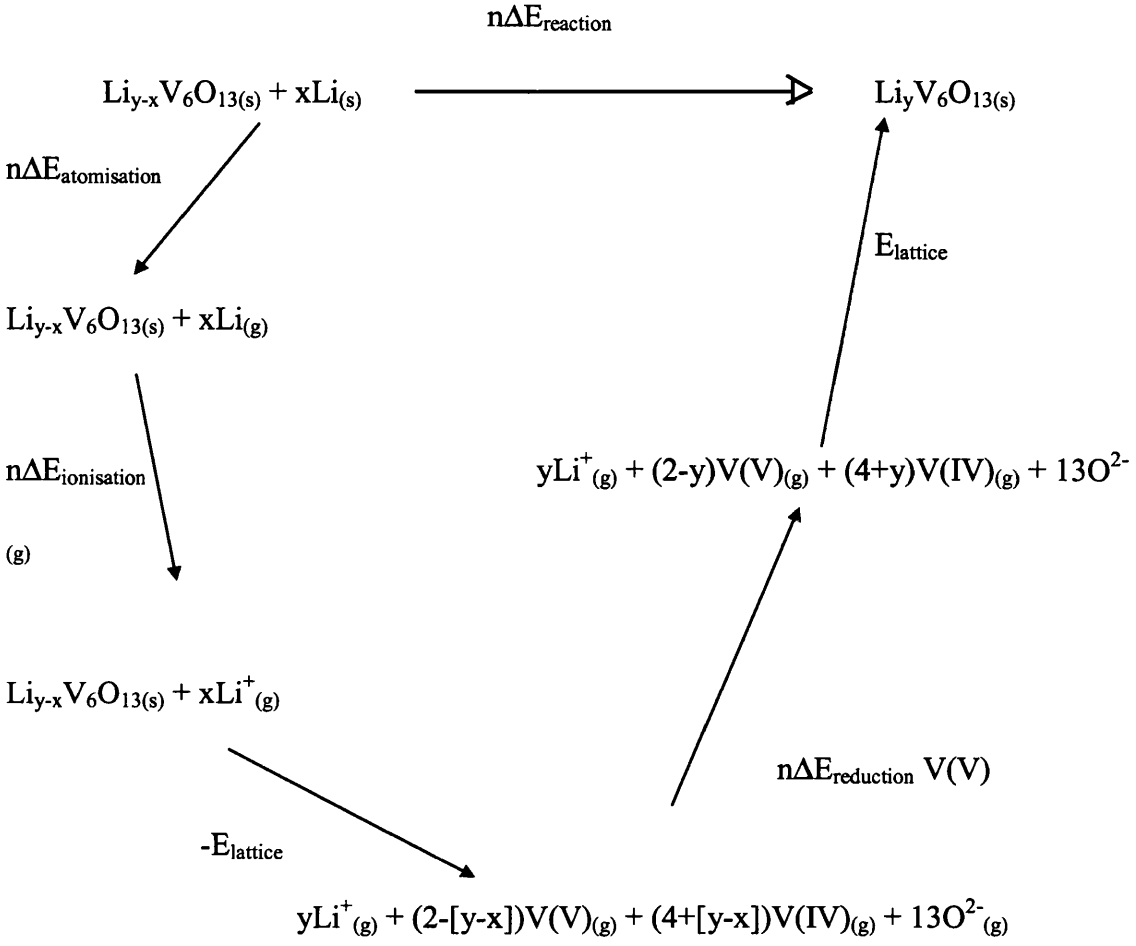

Fig. 4.10. General Born-Haber cycle for the intercalation of lithium in V_6O_{13}.

The required thermodynamic data is given below:

$Li_{(s)} \rightarrow Li_{(g)}$ $\Delta E_{atomisation}$ at 0 K. = +1.63eV

$Li_{(g)} \rightarrow Li^+_{(g)} + e^-$ $\Delta E_{ionisation}$ = +5.26eV

$V(V)_{(g)} + e^- \rightarrow V(IV)_{(g)}$ $\Delta E_{reduction}$ = -65.28eV

The remaining energy terms correspond to the optimised lattice energy of the relevant $Li_xV_6O_{13}$ phases, which have been given previously in Table 4.14.

The energy change, ΔE, for a range of intercalation reactions, equivalent to the emf of the cell, is given in Table 4.16, where $V_{24}O_{52}$ corresponds to the atomic formula of the supercell used.

x in $Li_xV_6O_{13}$	Average cell voltage (V)
0.125	2.15
0.375	3.40
0.75	0.97
1.25	0.20
1.75	-0.77

Table 4.16. Predicted voltages for the $Li_xV_6O_{13}$ system from interatomic potential based simulations.

These results suggest that this level of theory is inadequate for this type of prediction, when complex electronic factors become important. There may be some inconsistency between the calculated lattice energies and the experimental ionisation energy caused by differences between the formal charge distribution, imposed in the calculation, and the real electronic distribution in the material, where some covalent bonding is expected to be present.

4.5.3 Electronic Structure Calculations

Although the interatomic potential based calculations are useful, it is clear that they are often limited by their simplicity. Therefore, a series of electronic structure calculations have been carried out on the $Li_xV_6O_{13}$ system using Density Functional Theory. Again, we have used the stable lithium positions derived from the Mott-Littleton defect calculations to construct initial atomic geometries for a limited number of $Li_xV_6O_{13}$

phases, where x = 0.5, 1.0, 2.0, and 4.0. The simulation cell consists of a single V_6O_{13} unit cell, in which full atomic and electronic relaxation can take place. The planewave kinetic energy cutoff that was used for the V_2O_5 calculations has also been used to model this system, as the atomic species, and therefore, the pseudopotentials used, are the same in both cases. A standard Monkhorst-Pack scheme is employed to generate the k-points on a 2 x 5 x 4 grid.

Optimised geometries are show in Fig. 4.11 and Fig. 4.12, while unit cell parameters are compared to powder X-ray diffraction data in Table 4.17 and Fig. 4.13.

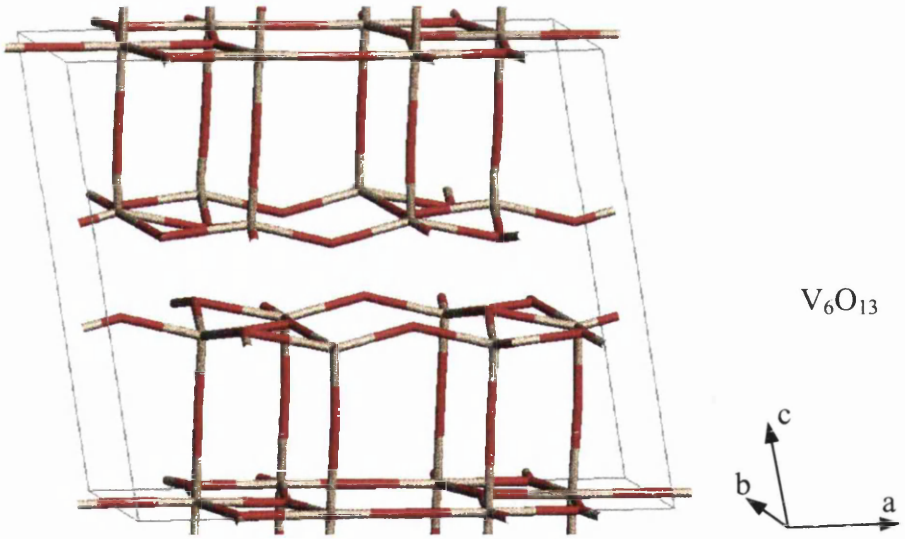

Fig. 4.11. Optimised geometries for V_6O_{13}.

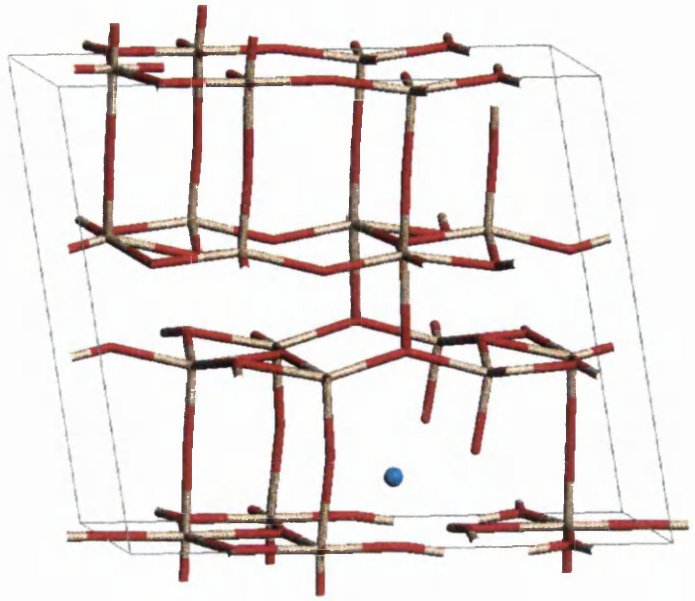

$Li_{0.5}V_6O_{13}$

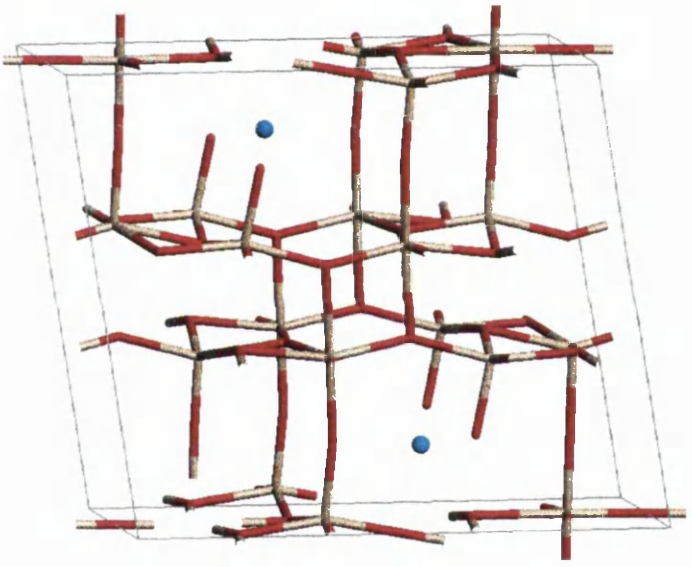

$Li_{1.0}V_6O_{13}$

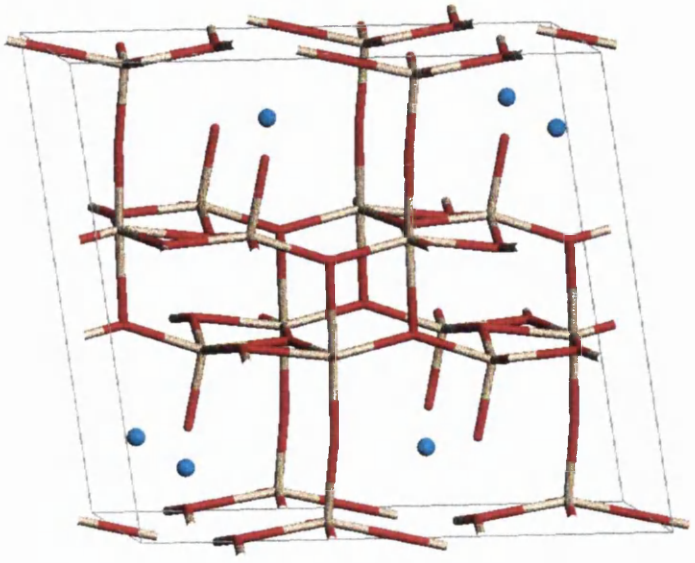

$Li_{2.0}V_6O_{13}$

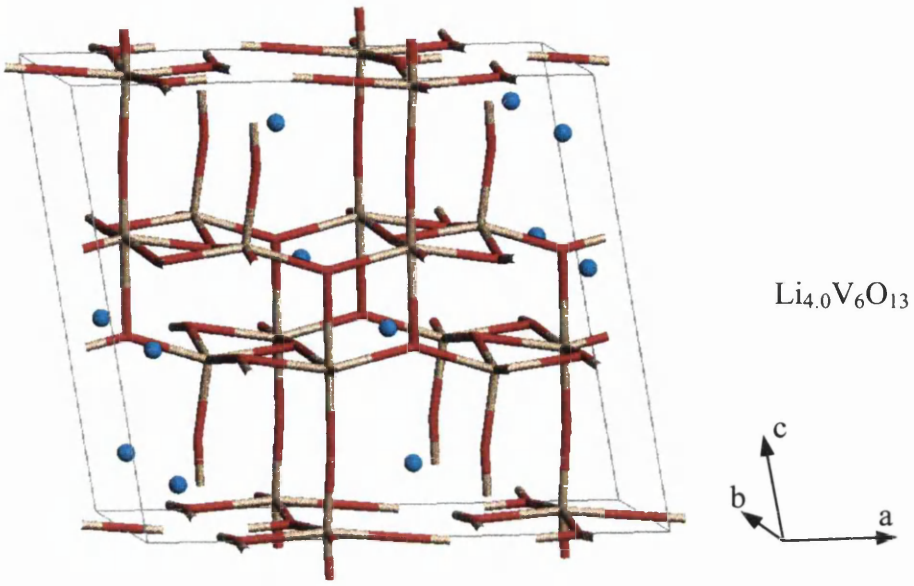

Fig. 4.12. Optimised geometries for $Li_{0.5}V_6O_{13}$, $Li_{1.0}V_6O_{13}$, $Li_{2.0}V_6O_{13}$, and $Li_{4.0}V_6O_{13}$, phases.

x in $Li_xV_6O_{13}$	Calculated				Experiment			
	a / Å	*b* / Å	*c* / Å	β / °	*a* / Å	*b* / Å	*c* / Å	β / °
0.0	12.00	3.71	10.22	100.6	11.92	3.68	10.14	100.9
0.5	12.01	3.73	10.26	100.8	11.89	3.69	10.40	101.1
1.0	11.99	3.73	10.45	100.7	11.85	3.69	10.48	101.2
2.0	11.95	3.74	10.71	100.6	11.86	3.66	10.89	100.4
4.0	11.91	3.94	10.37	101.4	-	-	-	-

Table 4.17. Calculated and experimental (Bergström 1997, 1998b) lattice parameters for $Li_xV_6O_{13}$

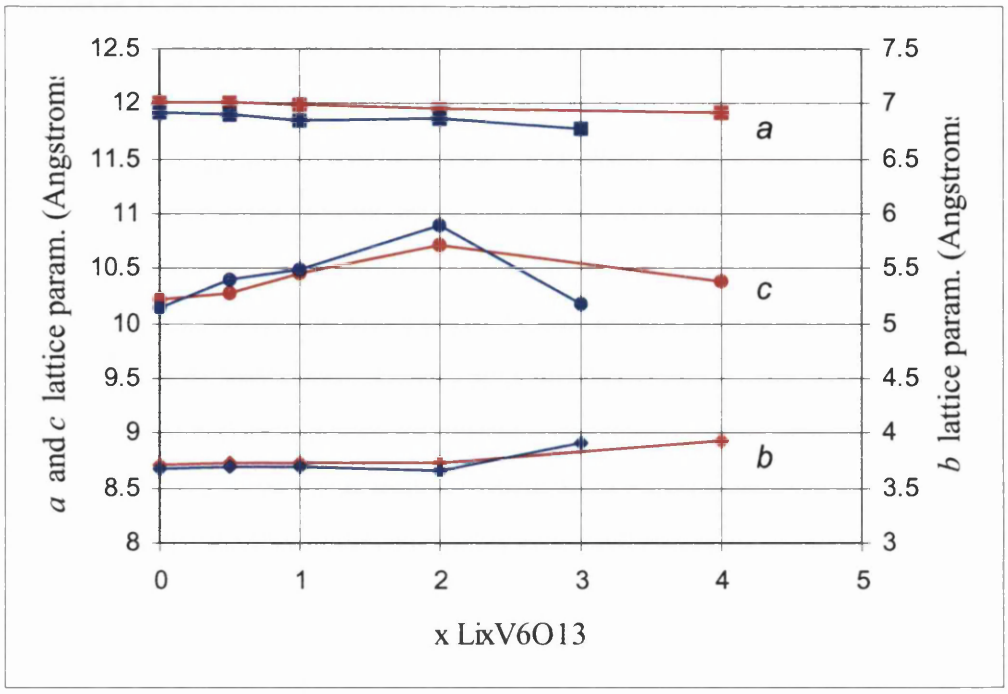

Fig. 4.13. Calculated (red) and experimental (blue) (Bergström 1997, 1998b) lattice parameters for $Li_xV_6O_{13}$

It can be seen from Figure 4.13 that the electronic structure calculations can accurately describe the dependence of the lattice parameters on the concentration of intercalated lithium. Comparison of the calculated $Li_2V_6O_{13}$ structure with single crystal X-ray diffraction data (Bergström 1997) in Table 4.17, demonstrates the close agreement between theory and experiment. The positions of the intercalated lithium ions within the V_6O_{13} cavities are well reproduced, as shown in Table 4.18, and represent a refinement of the positions predicted by the Mott-Littleton calculations.

	Calculation			Experiment		
Atom	x	y	Z	x	y	z
Li	0.0768	0.0	0.1264	0.0855	0.0	0.1369
V1	0.3464	0.0	0.0159	0.3544	0.0	0.0468
V2	0.4022	0.0	0.3689	0.4092	0.0	0.3946
V3	0.7189	0.0	0.3600	0.7090	0.0	0.3635
O1	0.1741	0.0	0.0008	0.1803	0.0	0.0080
O2	0.8914	0.0	0.3877	0.8794	0.0	0.3747
O3	0.2359	0.0	0.3990	0.2398	0.0	0.4068
O4	0.5	0.0	0.0	0.5	0.0	0.0
O5	0.3804	0.0	0.1958	0.3900	0.0	0.1987
O6	0.6734	0.0	0.1893	0.6578	0.0	0.2135
O7	0.5709	0.0	0.4164	0.5686	0.0	0.4266

Table 4.18. Calculated and experimental (Bergström 1997) atomic co-ordinates for $Li_2V_6O_{13}$

The optimised $Li_4V_6O_{13}$ structure shows that the lithium ions now occupy a new site within the lattice with five-fold coordination in a pyramidal arrangement. This site corresponds to defect site D, one of the sites found by the interatomic potential based Mott-Littleton defect calculations described earlier – refer to Table 4.13 and Fig. 4.8. This site was predicted to be less favourable than other possible Li^+ positions, but it is likely that electrostatic interactions between neighbouring lithium ions, at this level of loading, will affect the relative stabilities of these sites. Although experimental structural data is not available for the $Li_4V_6O_{13}$ phase, single crystal X-ray studies on $Li_3V_6O_{13}$ have shown that this pyramidal site is occupied in this phase (Bergström 1998a).

4.5.3.1 Prediction of cell voltages

As has already been described for the $Li_xV_2O_5$ system, we can use the total energies from the series of geometry optimisations on $Li_xV_6O_{13}$ to calculate average cell voltages for a number of lithium concentrations. The calculated cell voltages are defined for a composition that is an average of the two compositions simulated, while the voltage itself is an average of all the values between these two limits. The total energies for each phase are given in Table 4.19, and the resulting predictions of the cell voltage for an average composition are shown in Table 4.20.

Phase	Total energy / eV
V_6O_{13}	-329.082
$Li_{0.5}V_6O_{13}$	-333.159
$Li_{1.0}V_6O_{13}$	-337.091
$Li_{2.0}V_6O_{13}$	-344.850
$Li_{4.0}V_6O_{13}$	-357.42

Table 4.19. Optimised total energies for the $Li_xV_6O_{13}$ phases.

Average composition x in $Li_xV_6O_{13}$	Average cell voltage / V	Experiment / V
0.25	2.17	2.80
0.75	2.03	2.75
1.5	1.98	2.58
3.0	1.24	2.35

Table 4.20. Predicted cell voltages for a range of average compositions compared to experimental measurements (Bergström 1998b).

Although the number of points does not allow us to predict the detailed features of the discharge curve, the calculated values are in moderate agreement with experiment, when the underestimation of cell voltages by 0.4 - 0.5V produced with DFT methods, discussed in Chapter 3, is taken into account. The discrepancy between calculation and experiment is not constant, differences of around 0.6 – 1.0V are seen, and this is likely to be due to the changing shape of the experimental curve. Errors tend to be greater when the cell voltage, V, changes rapidly with composition, x, as the predicted voltages are averages. There are rapid changes in the voltage curve around 1V and 3V, and this is likely to adversely affect the calculated voltages at 1.5V and 3V. Ideally, our study would include a greater number of simulated phases which would improve the resolution in regions where the voltage changes rapidly with composition. This is not possible at present as the larger supercells required to simulate intermediate compositions are too computationally expensive.

4.5.3.2 Electronic Structure.

We begin by analysing the calculated electronic distribution in pure V_6O_{13}, for the relaxed geometry from the DFT simulation. Because of the diffuse nature of planewaves, it is not possible to calculate orbital populations directly, instead we intend to use a simple spherical integration of the electron density around each atom. It can be seen from the electron density map in Fig. 4.14 that even this simple analysis should give good charge states for each atomic species as the electron density around each atom is essentially spherical.

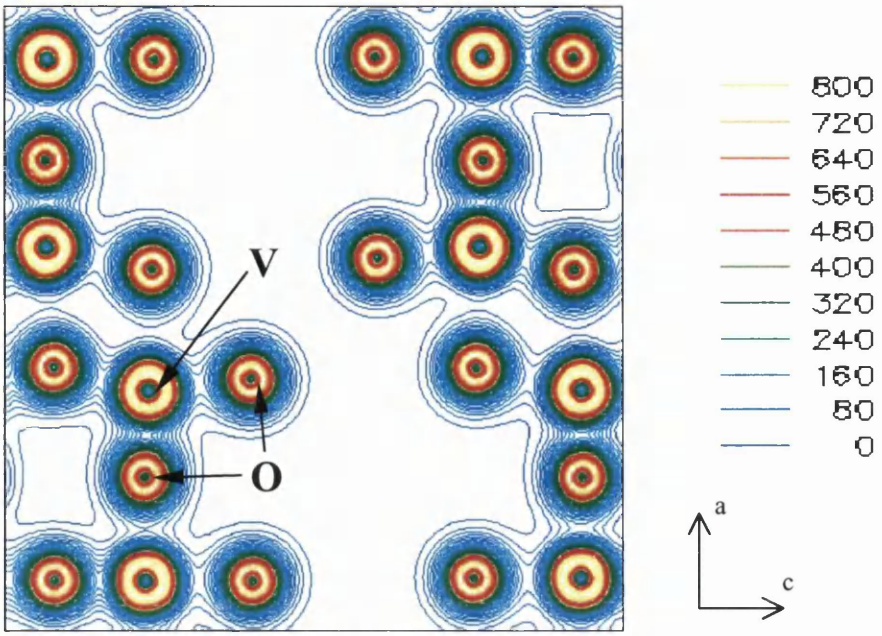

Fig. 4.14. The valence electron density distribution in pure V_6O_{13}, viewed along the [*010*] direction. Contours in $10^2e/Å^2$.

There are significant concentrations of electron density around the vanadium species because, to increase the accuracy of the simulation, the vanadium pseudopotential used in the calculation treats the *3p* electron shell as valence electrons.

The results of integrating the electron density around each atom species in the asymmetrical unit, within spheres of a number of radii, are shown in Figure 4.15.

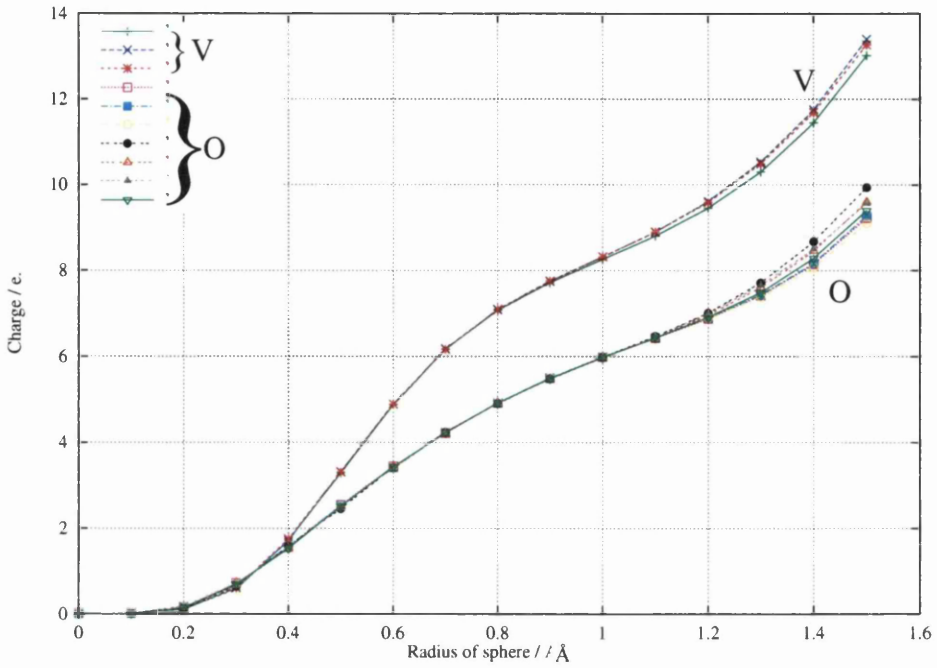

Fig 4.15. Spherical integration of charges around V and O atoms in V_6O_{13}.

It is clear from Fig. 4.15 that all the vanadium atoms are similarly charged, and therefore, at least within the DFT simulation, there is no localisation of V(IV) and V(V) species. By studying the way the electron charge changes with distance from the centre of each atom it is possible to estimate the ionic radius - the point of inflection on each curve - and the ionic charge. Doing this for the vanadium species suggests as ionic radius of around 1Å and a valence shell that contains just over 8 electrons, which corresponds to the presence of V^{II} after the six $3p$ electrons have been taken into account. The oxygens appear to be slightly electron deficient, with just under eight electrons in their valence shell. These charges are likely to be a result of a degree of covalent bonding within the material, as there are a number of V-O bonds that are not much more than 1.7Å in length. Bonding with a degree of covalency can be seen in Fig. 4.14, where the electron spheres overlap along the [*001*] direction.

In recent work by Bergström *et al* (1998c) a technique called deformation electron density refinement has been used to extract charge distributions from single crystal X-ray data. For each atom, the deviation of the electron density from that associated with a spherical neutral atom distribution is modelled by a linear combination of deformation functions (Hirshfeld 1971). Using this technique they find that each vanadium has an ionic charge of between 0.6 to 0.8e, which suggests a delocalised electronic arrangement that is in agreement with the DFT result.

The implication of this electron distribution is that the formal charges that were used in the atomistic simulation are likely to be incorrect, as they assumed a localisation of V(IV) and V(V) species. This formal charge distribution may have contributed to the errors in the cell voltages that were calculated using atomistic methods. A potential model that had been derived using partial charges may have been more successful in modelling the structure of V_6O_{13}, but it would have been difficult to use these potentials to study the $Li_xV_6O_{13}$ phases as reducing individual V(V) ions would have been impossible.

The electron density distributions in the lithiated phases, $Li_xV_6O_{13}$, have been investigated by using electron density difference maps, described previously in chapter 3. These plots, presented in Figs. 4.16 and 4.17, show the changes to the electronic structure as lithium is incorporated into the host and any localisation of the electrons that accompany the intercalated lithium.

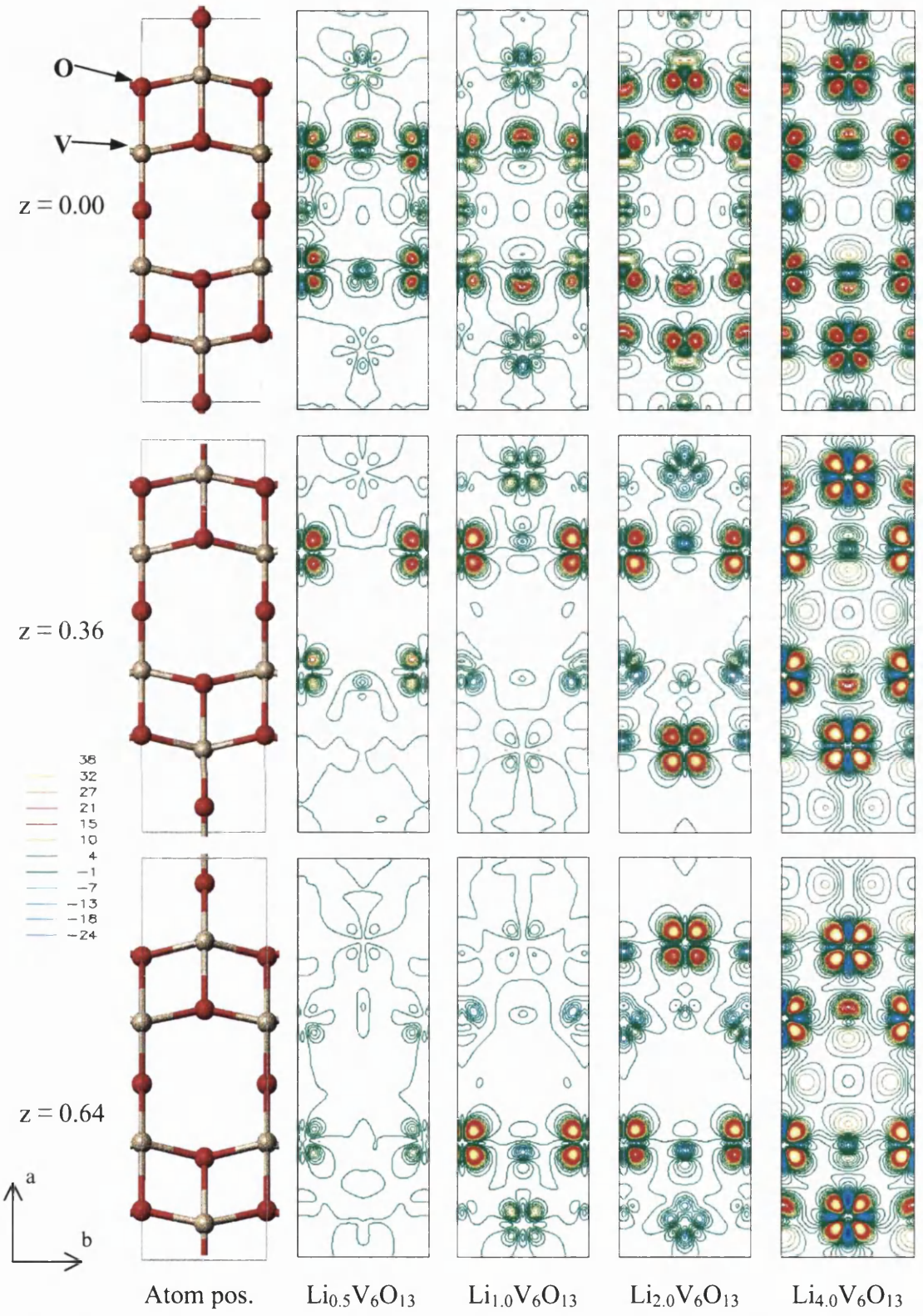

Fig. 4.16. Electron density difference plots for a number of $Li_xV_6O_{13}$ phases, viewed along [*001*]. Blue contours indicates negative electron density, zero density is green, while red and yellow contours show areas of increasing positive density. Contours in $10^2e/Å^2$.

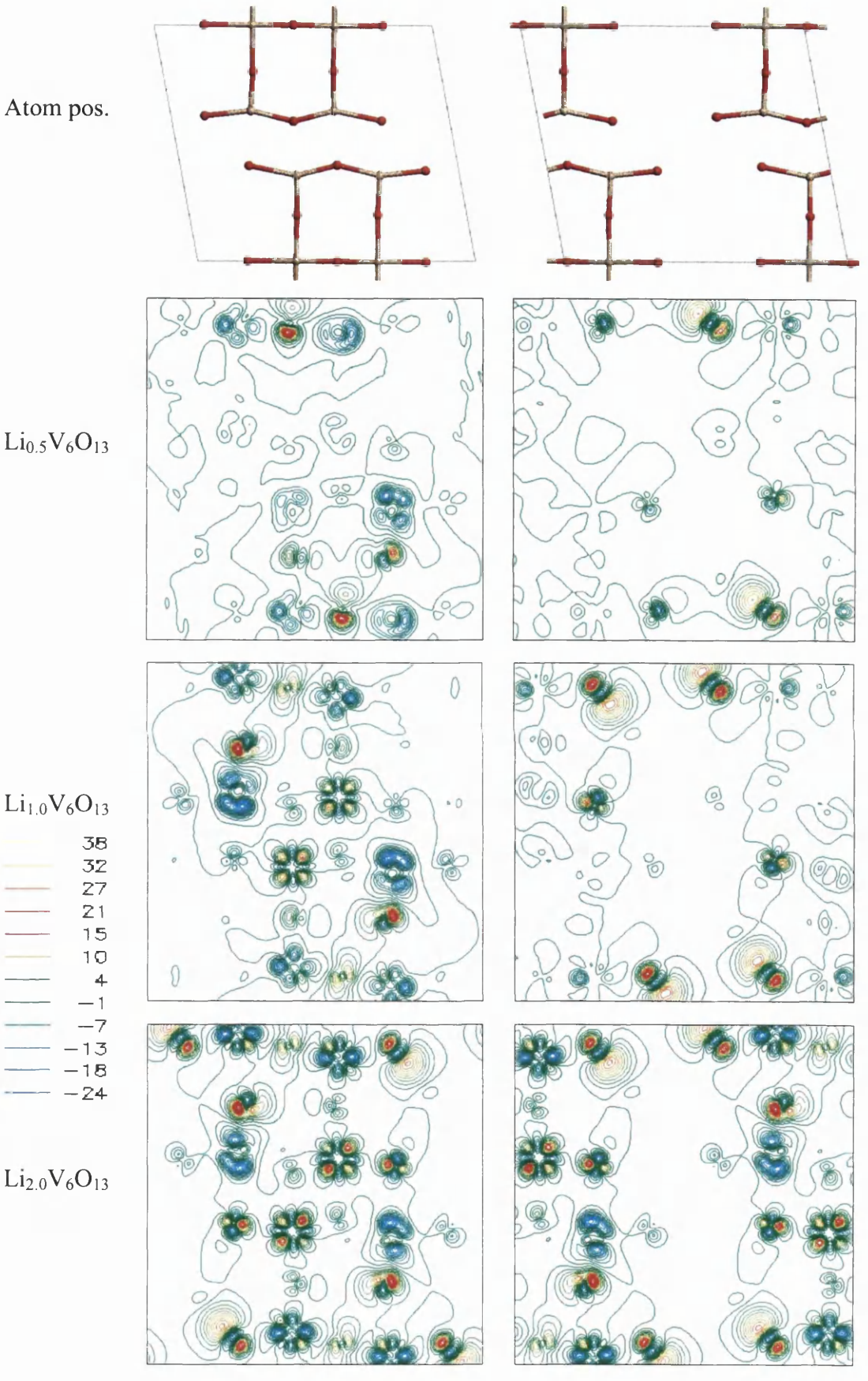
Atom pos.
$Li_{0.5}V_6O_{13}$
$Li_{1.0}V_6O_{13}$
38
32
27
21
15
10
4
−1
−7
−13
−18
−24
$Li_{2.0}V_6O_{13}$

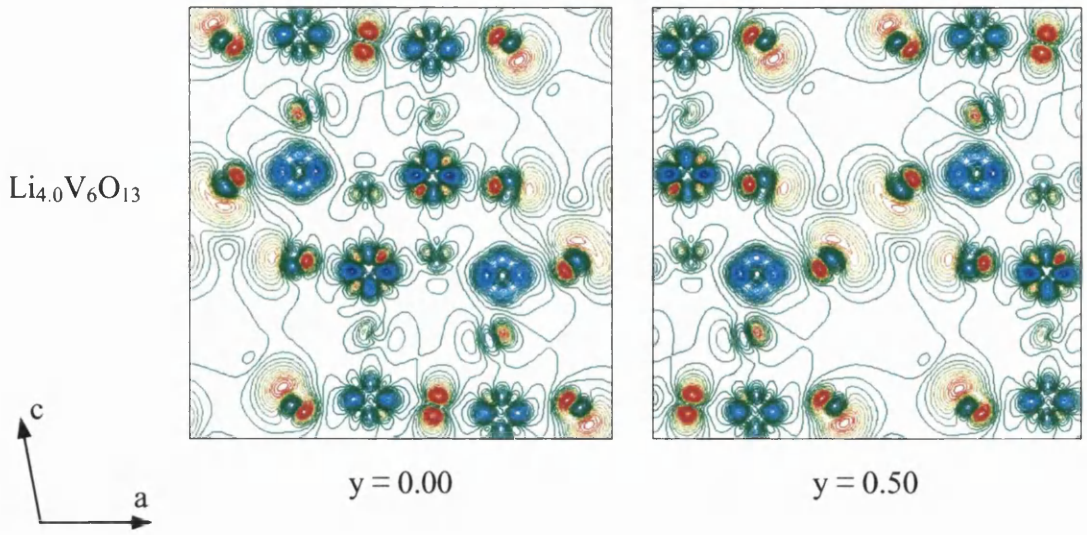

Fig. 4.17. Electron density difference plots for a number of $Li_xV_6O_{13}$ phases, viewed along [*010*]. Blue contours indicates negative electron density, zero density is green, while red and yellow contours show areas of increasing positive density. Contours in $10^2e/Å^2$.

As expected and already seen in the $Li_xV_2O_5$ system, the intercalated lithium ions are fully ionised within V_6O_{13}, as the electron density in the region of the inserted ions is identical to that in the pure host material for all lithium concentrations. From Figs. 4.16 and 4.17, it is clear that the vanadium centres accept the majority of the electrons that accompany lithium insertion, in d-like orbitals orientated in the *ab* plane. Generally, the metal atoms located in the 'double layer' structural element, containing the V(2) and V(3) species, are affected to a greater degree than the single layer vanadiums, V(1).

From Fig. 4.17, it is evident that, at higher lithium concentrations, small amounts of negative density, which correspond to electron density loss, are localised on a number of vanadium atom orbitals, while a degree of electron density gain is also seen on a number of oxygen atoms. This electron rearrangement is possibly caused by a disruption of back donation from oxygen to metal due to the reduction of the vanadium ions.

A detailed examination of the electron density difference maps for the $Li_{0.5}V_6O_{13}$ and $Li_{1.0}V_6O_{13}$ phase indicates that at low lithium concentrations there is some localised reduction of the metal atoms. Figs. 4.16 and 4.17 show that only the vanadium species that border the occupied cavities gain electron density, and that, within this group, certain metals gain more than others. It is only at the higher lithium concentrations in the $Li_4V_6O_{13}$ phase, that all the vanadium atoms are reduced to a significant degree. Strong similarities, therefore, exist between the pattern of vanadium reduction in V_2O_5 and V_6O_{13}, as the degree of reduction is related to the distance between the vanadium centres and the intercalated lithium ions in both materials.

To investigate the overall changes in the vanadium metal oxidation-state, we have carried out a spherical integration of the electron distribution for $Li_{4.0}V_2O_5$, shown in Fig. 4.18.

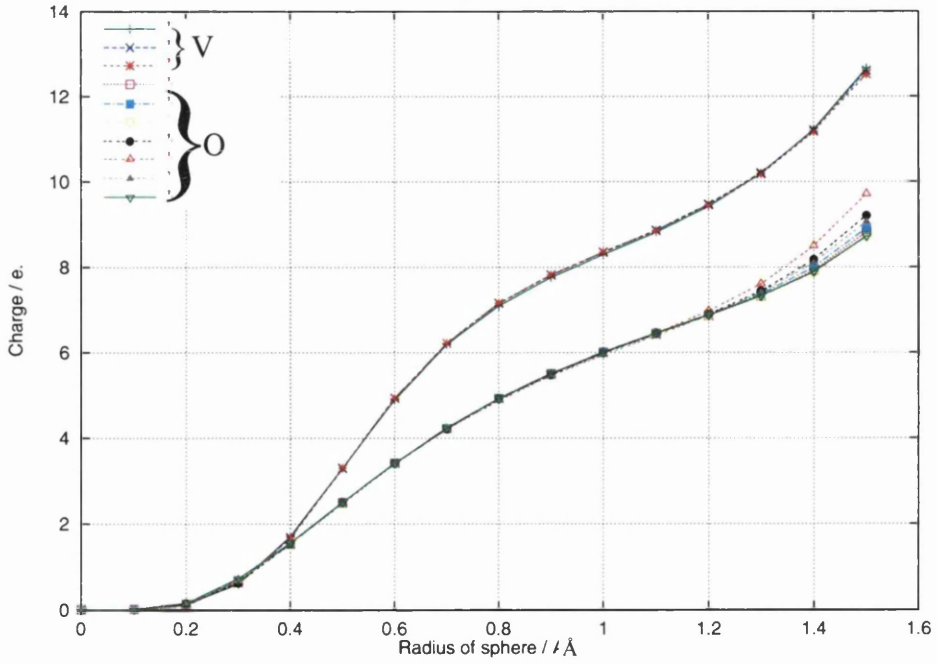

Fig. 4.18. Spherical integration of electron density in $Li_{4.0}V_6O_{13}$.

Unexpectedly, when comparing Fig. 4.18 and the equivalent plots for V_6O_{13} in Fig. 4.15, we see no notable change in the amount of charge that is localised around either the vanadium or the oxygen atoms. It is suggested that the charge due to the lithium ions is lost due to the crudeness of the spherical integration method that has been used.

4.6 Summary

We have used a combination of static lattice simulation and electronic structure techniques to investigate the effects of lithium incorporation in V_6O_{13}, showing that computational techniques can provide useful chemical information about a highly complex system. After using empirical fitting techniques to derive a potential model for V_6O_{13}, we used this model to carry out a series of Mott-Littleton calculations to assess the relative stabilities of a selection of Li^+ sites in the V_6O_{13} lattice.

In addition, we used static lattice techniques to successfully model a number of $Li_xV_6O_{13}$ phases by selectively reducing available V(V) species to V(IV). The evolution of the structure with lithium content compares well with experiment, although calculated lattice energies, combined with a simple Born-Haber cycle, could not be used to predict cell voltages. It is suggested that the formal charge model that is used in the static lattice simulation does not represent the true charge distribution in $Li_xV_6O_{13}$. Therefore, as electrostatic effects are the dominant contribution to the lattice energy, it is unsurprising that a complex thermodynamic property like the cell potential cannot be reproduced correctly.

Density Functional Theory has been used to optimise the geometries of a series of $Li_xV_6O_{13}$ phases, using the information on the Li^+ positions gained from the atomistic calculations to construct initial geometries. Optimised geometries are in good agreement with experimental structures, and the resulting total energies have been used to calculate average cell voltages that continue a trend seen for $Li_xV_2O_5$ of underestimating experimental values by around 0.5V.

An analysis of the calculated valence electron density distributions for each $Li_xV_6O_{13}$ phase indicates that lithium intercalation results in the selective reduction of vanadium atoms that lie on the edges of the occupied cavities. Some loss of electron density from certain vanadium orbitals is seen, suggesting a degree of electronic rearrangement. Oxygen atoms also gain small amounts of electron density during lithium insertion.

Chapter 5

The Spinel $Li_xCo_yMn_{(4-y)}O_8$ as a Cathode Material

In recent years there has been a growing interest in transition metal spinel systems as possible candidates for cathode materials in lithium ion batteries. $LiMn_2O_4$, which can generate cell voltages of over 4V, has been studied extensively over the last ten years (Tarascon 1994, Koksbang 1996). A recent development is the rapidly increasing number of mixed transition metal spinels that have been reported which have been found to give impressive cell voltages. These include $LiNiVO_4$ (Fey 1994) and $LiCr_xMn_{2-x}O_4$ (Sigala 1995), with reported cell voltages of 4.7V, $LiNi_xMn_{2-x}O_8$ (Amine 1996, Zhong 1997) giving 4.8V, mixed Ni-Cu-Mn spinels (EinEli 1999), the $LiCu_xMn_{2-x}O_4$ system (EimEli 1998), and $LiFe_xMn_{2-x}O_4$ (Kawai 1998a).

The system of interest in this chapter is a mixed cobalt-manganese spinel, $LiCo_xMn_{2-x}O_8$, which has been reported by Kawai *et al* to give unusually high cell voltages. In a $Li/LiPF_6$, propylene carbonate/$Li_2CoMn_3O_8$ test cell, voltages over 5V have been recorded for the first time (Kawai 1998b). Although problems are encountered with

electrolyte stability when operating at this kind of potential, the increase in cell voltage brings larger scale applications of lithium ion batteries, such as zero emission vehicles, a step closer.

5.1 Experimental Background

5.1.1 The Spinel Structure Of $Li_2CoMn_3O_8$

The spinel structure is adopted by a wide range of transition metal oxide materials. The cubic unit cell, with space group *Fd3m*, contains two metal sites: the octahedral A site, which is 16-fold degenerate, and the 8-fold degenerate B site, which is tetrahedrally co-ordinated. The transition metal distribution in the $Li_2CoMn_3O_8$ system was determined by comparing powder X-ray diffraction data with theoretically generated patterns for the most likely arrangements (Kawai 1998b). The closest agreement was found when the lithium atoms fully occupied the tetrahedral 8a sites, while the Co and Mn are distributed over the 16d sites in a 1:3 ratio. No evidence of cation ordering over these octahedral sites was found, although the authors did not discount this possibility.

The octahedral sites are joined by edge sharing to form chains of MO_6 octahedra that run along the [*110*], [*101*], and [*011*] directions. The tetrahedral sites are located between these intertwined chains. The oxygen positions are all related by symmetry, and can be described by a single fractional co-ordinate parameter, u, as long as the metal cations are distributed randomly. The octahedral and tetrahedral distribution within the spinel structure is shown in Fig. 5.1.

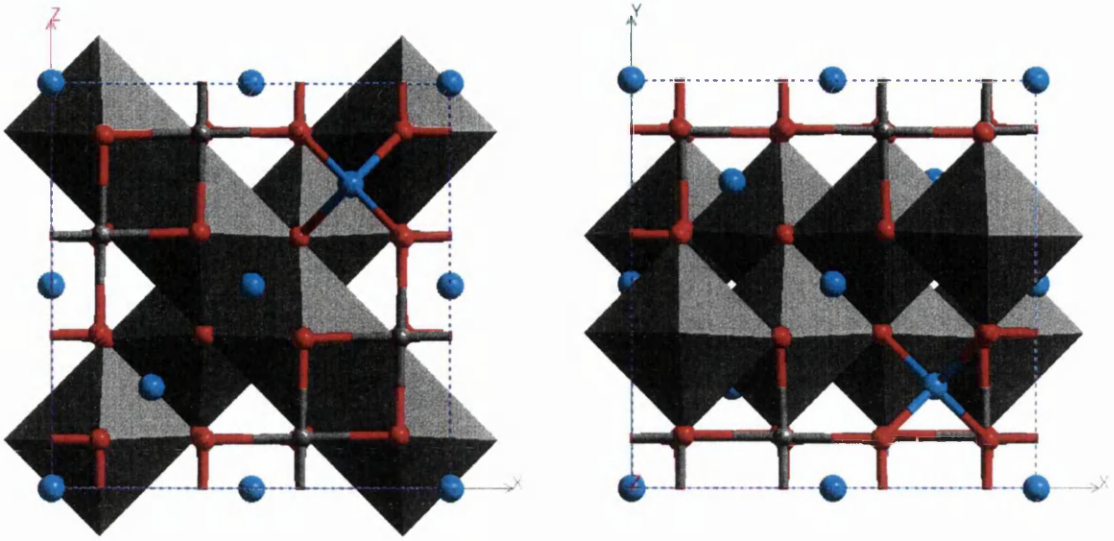

Viewed along [*010*] Viewed along [*001*]

Fig. 5.1. The spinel structure, A_2BO_4, with the A site metals in grey, the B site metals in cyan, and oxygens shown in red. Two chains of octahedra are highlighted as polyhedra, and the tetrahedral co-ordination of a single B site metal is also shown.

5.1.2 Electrochemical Measurements

The discharge curve of the $Li_xCoMn_3O_8$ cathode contains two plateaux, the first at around 5.1V occurs between x = 0.1 to 1.1, while the second plateau, centred around 4.0V, runs from x = 1.1 to 2.0. The experimental curve is shown in Fig. 5.2.

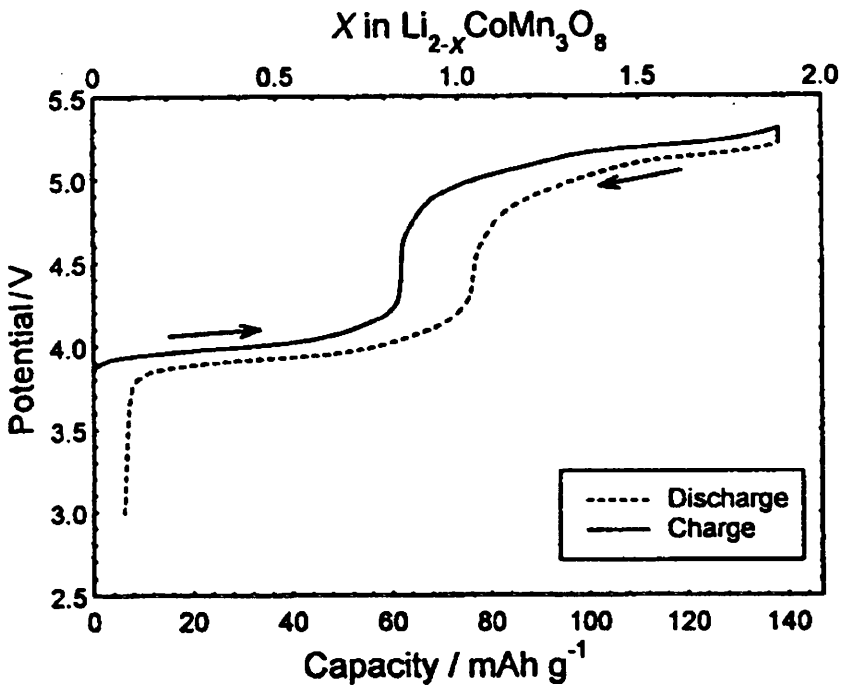

Fig. 5.2. Experimental discharge curve for $Li_xCoMn_3O_8$ (Kawai 1998b).

There are a number of possible redox reactions that could account for the shape of the discharge curve, including Co(II) ↔ Co(III), Co(III) ↔ Co(IV), and Mn(III) ↔ Mn(IV). A classical description of the redox processes within the cell would seem to suggest that the plateau above 5V is the result of the reduction of Co(IV) to Co(III), while the region at a lower potential is due to the equivalent reduction on the Mn(IV). As the ionisation energy of Co^{4+} is higher than Mn^{4+}, this would account for the step in the cell potential at around x = 1, but it does not explain why an apparently identical redox process in $LiCoO_2$ does not produce such a high potential. The presence of Co(II) within the lattice is another factor that will affect the shape of the discharge curve, although the Co(II) ↔ Co(III) redox couple is unlikely to contribute to a cell potential above 5V. The origins of this unusually high voltage will be explored in detail in the following discussion.

5.2 Results and Discussion

While experiment has not resolved the issue of cation ordering in mixed metal spinels, it is impossible to simulate the $Li_2CoMn_3O_8$ phase using electronic structure techniques unless cation ordering is included in the model. Static lattice simulations using interatomic potentials have been employed to find the most stable distribution of transition metal ions in $Li_2CoMn_3O_8$, so that this distribution can be used as a basis for the initial atomic geometries used in the DFT calculations.

5.2.1 Fitting a potential model using empirical methods.

Before comparisons between a number of cation distributions can be made, the potential force-field that is used must reproduce the spinel structure successfully when partial occupancies are used for the A site cations. The Mn(III) – O, Mn(IV) – O, and Li^{tet} - O Buckingham potential parameters were taken from empirical fitting work by Woodley *et al* on $LiFe_xMn_{2-x}O_4$ (Woodley 2000), while the Fe^{III} – O Buckingham potential parameters were used as a starting point for a new Co(III) – O potential, where the parameters were derived by empirical fitting to the structure of $LiCoO_2$.

$LiCoO_2$ has a hexagonal unit cell (Johnston 1958) in which alternate layers of CoO_6 octahedra and Li ions are arranged along the [*001*] direction, as shown in Fig. 5.3. The Co-O bond lengths determine the *a* and *b* unit cell parameters, while *c* is controlled by the bonding between the layers, which is largely dependent on the interactions between the Li^+ and O^{2-} ions.

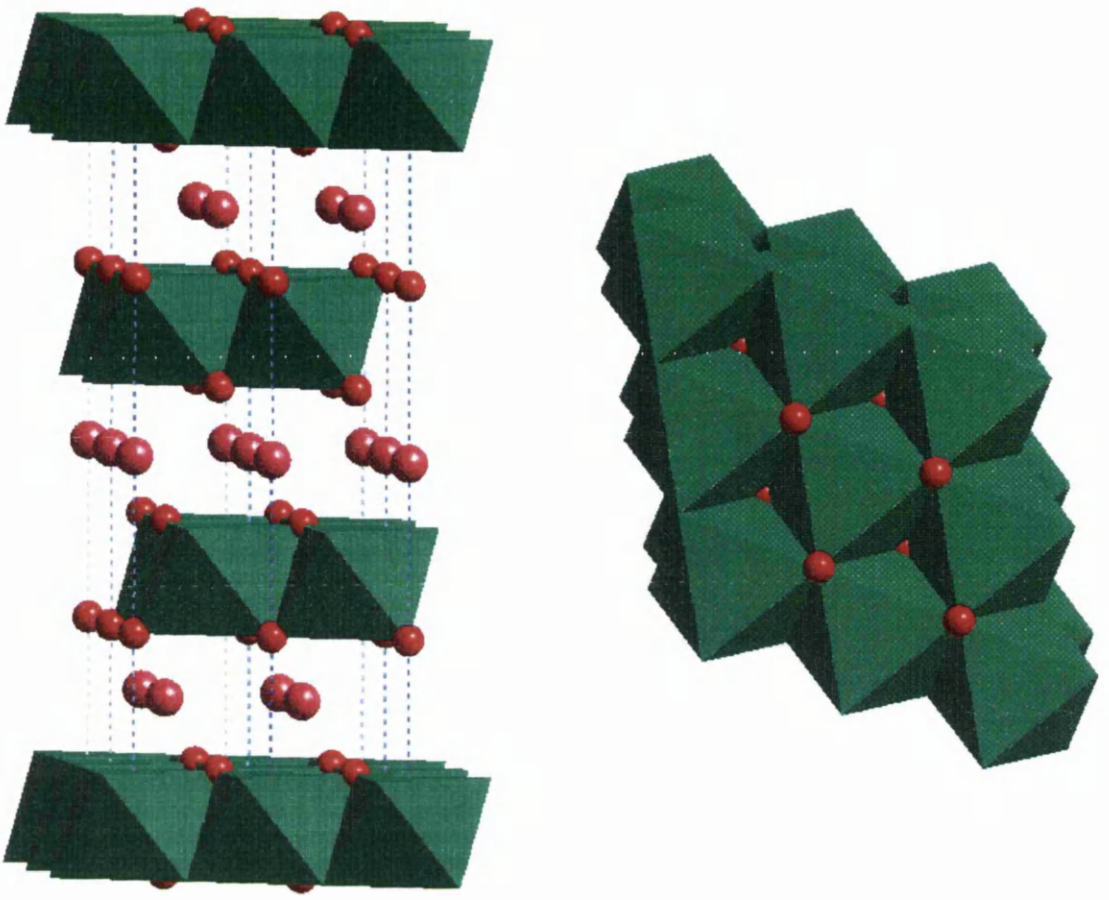

Viewed along [*010*] Viewed along [*001*]

Fig. 5.3. The crystal structure of $LiCoO_2$ (Johnston 1958).

As the lithium ions in $LiCoO_2$ do not occupy tetrahedral sites, it is unlikely that the Li-O potential used in the model will be able to reproduce the interactions between the layers correctly. By biasing the fitting process to reproducing the *a* and *b* lattice parameters correctly, at the expense of the *c* parameter, it is possible to negate this effect. The optimised geometry for $LiCoO_2$ is compared to experiment in Table 5.1.

	Experimental	Calculated	Error (%)
Cell Volume ($Å^3$)	96.54	101.71	5.35
a(Å)	2.8166	2.8175	0.03
c (Å)	14.052	14.794	5.28
O position (frac)	0.2600	0.2625	0.97

Table 5.1. Experimental (Johnston 1958) and optimised geometry of $LiCoO_2$.

It is clear from the optimised geometry of $LiCoO_2$ that the short-range interactions between the CoO_6 and Li layers are not reproduced correctly, which, we believe as noted previously, reflects the use of an inappropriate Li-O potential. There is good agreement with experiment, however, along the *a* and *b* directions, and this results in a Co-O bond length that is within 0.5% of the experimental value of 1.9252Å. The only modification of the Co-O potential, based on the Fe^{III}-O potential from Woodley's model of $LiFe_xMn_{2-x}O_4$, required to achieve this fit was a 25% reduction in the Buckingham A parameter, a result which is consistent with Co^{3+} having a smaller ionic radius than Fe^{3+}.

Details of the force-field, both Buckingham potential and shell model parameters used to model the spinel phase $Li_2CoMn_3O_8$, including the derived Co(III)-O potential, are detailed in Table 5.2.

Interaction	A (eV)	ρ (Å)	C (eVÅ^6)	Y / e	k (eVÅ^{-2})
Li^{tet}-O	426.48	0.30000	0.00	-	-
Co(III)-O	1007.11	0.30690	0.00	+1.029	10082.50
Mn(III)-O	1686.13	0.29620	0.00	+1.029	148.00
Mn(IV)-O	3087.83	0.26420	0.00	-	-
O-O	22.41	0.69370	32.32	-2.513	20.53

Table 5.2. Force-field parameters for $Li_2CoMn_3O_8$.

5.2.2 Atomistic Geometry Optimisation of $Li_2CoMn_3O_8$.

The potential model in Table 5.2 has been used to optimise the structure of $Li_2CoMn_3O_8$ using partial occupancies for the A site cation, so that the Mn(III), Mn(IV), and Co(III) species are all distributed evenly over the octahedral sites, ensuring that the cubic symmetry is maintained. The optimised geometry and bond lengths are compared to experiment in Table 5.3.

	Experiment	Calculated	Error / %
Cell Volume (Å^3)	537.70	542.78	0.94
a / Å	8.157	8.132	0.31
O position (u)	0.3810	0.3863	1.39
M-M / Å	2.875	2.884	0.31
M-O / Å	1.985	1.952	1.66
Li-O / Å	1.845	1.926	4.39

Table 5.3. Optimised geometry of $Li_2CoMn_3O_8$ compared to experiment (Kawai 1998b).

The unit cell dimensions and atomic positions are, in general, reproduced accurately in the optimised structure, giving us confidence that static lattice simulations can be used to study cation ordering in the spinel structure.

5.2.2.1 Cation Ordering in $Li_2CoMn_3O_8$

It is a very complex process to include partial occupancies in electronic structure calculations, therefore, the inclusion of ordering on the A site is unavoidable. We have used the interatomic potential model, described above, to carry out a series of geometry optimisations to compare the stabilities of a number of distributions of Co(III), Mn(III), and Mn(IV) atoms over the octahedral sites. By comparing the calculated lattice energies, we intend to find the most stable configuration, which will be adopted as the initial geometry for the electronic structure calculations.

All symmetry constraints have been removed from the simulations, allowing full relaxation to occur around each metal centre. The optimised lattice energies of all the configurations that were modelled are given in Table 5.4, while the atomic structures of a selected number of geometries are shown in Fig. 5.4.

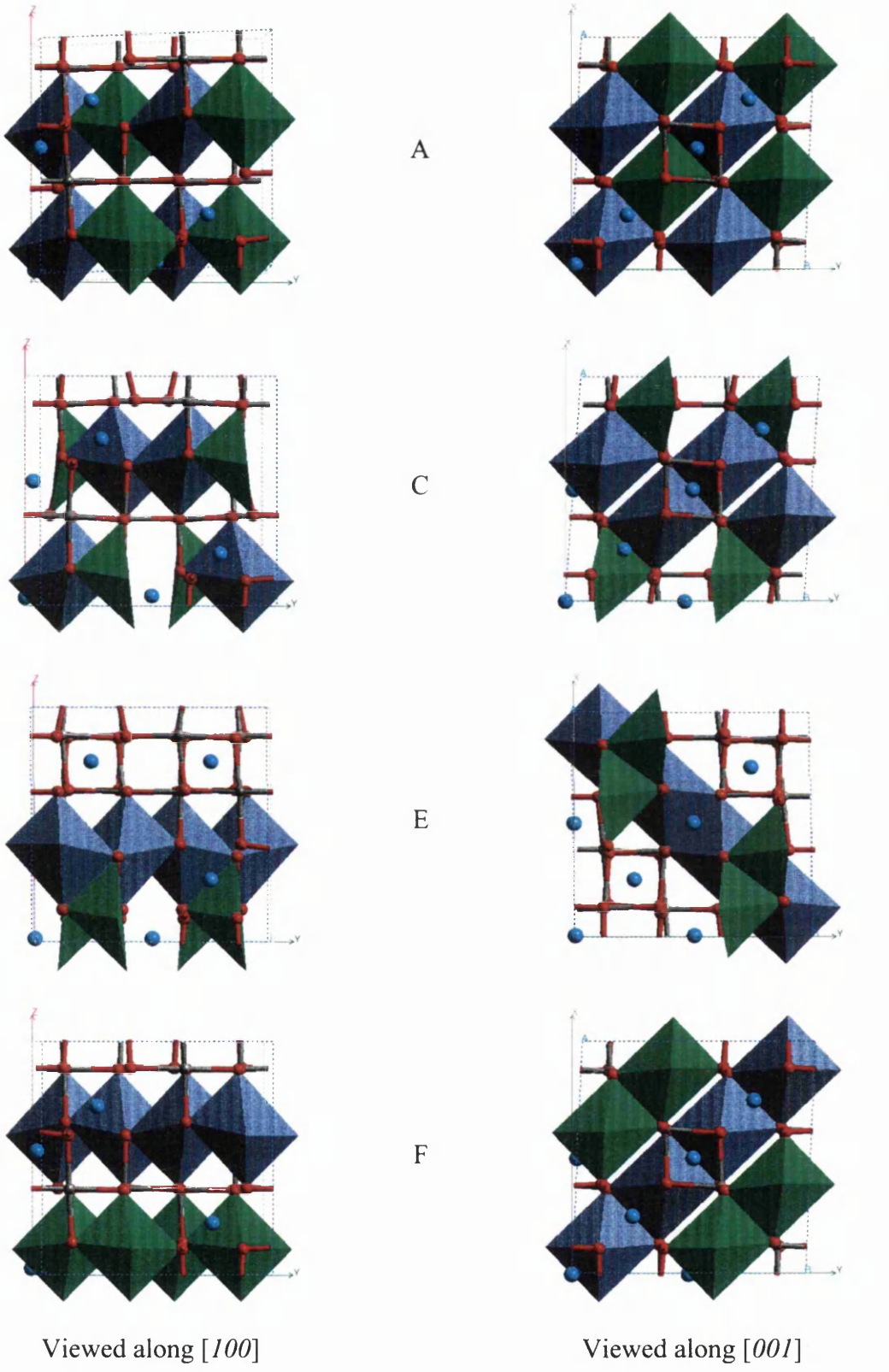

Fig. 5.4. Optimised geometries for spinel phase $Li_2CoMn_3O_8$ with different A site cation distributions. Distributions A, C, E, and F are shown with Co^{3+} octahedra shown in green, Mn^{3+} octahedra in dark blue, Mn^{4+} are grey, and oxygens in red.

Configuration	Lattice energy / eV
A	-1771.25
B	-1768.89
C	-1771.12
D	-1768.86
E	-1769.18
F	-1770.63

Table 5.4. Optimised lattice energies of spinel phase $Li_2CoMn_3O_8$ with different A site cation distributions.

Although there are a number of octahedral site distributions that are very close in energy, the most stable structure is given by configuration A, where the edge sharing between M^{3+} and M^{4+} octahedra is maximised. It is likely that this distribution produces the least electrostatic repulsion between neighbouring transition metal ions, although steric effects may contribute.

Interestingly, the energy differences between the different cation arrangements, of up to 2.2eV, suggests that the standard entropy term associated with the system is unlikely to be large enough to generate a random distribution at room temperature. We therefore propose that cation ordering is likely to occur in the spinel phases, $Li_2CoMn_3O_8$.

5.2.3 Electronic Structure Calculations

A series of electronic structure calculations has been carried out on a number of $Li_xCo_yMn_{4-y}O_8$ phases, where x = 0, 1, 2, and y = 0, 1, 2, and 4. In this way, we can

study the effects that lithium intercalation has on the atomic and electronic structure, and investigate the dependence of the cell voltage on the Co : Mn ratio. We also hope to be able to rationalise the unusually high voltage that is measured experimentally in the $Li_xCoMn_3O_8$ phase, in terms of the changes to the electronic structure that occurs as lithium is incorporated into the spinel structure.

The calculations are carried out using the VASP code, employing the planewave - pseudopotential method that is described in detail in Chapter 2. A single unit cell, containing 16 transition metal atoms, has been used as the simulation cell. A planewave kinetic energy cutoff of 550eV has been shown previously to be adequate for modelling this type of system, while k-point co-ordinates were generated using 2 x 2 x 2 Monkhorst-Pack scheme. Although this means that there is relatively coarse sampling within the Brillouin zone, the $Li_xCo_yMn_{4-y}O_8$ phases are semi-conductors, and consequently, do not require a large number of k-points.

5.2.3.1 Spin states in $Li_xCo_yMn_{4-y}O_8$

Before full geometry optimisation of the spinel structures can be carried out, it is essential to determine the ground-state spin configuration for each phase. This has been achieved by undertaking a series of single point calculations (no geometry relaxation) on a number of possible spin configurations, and comparing the resulting total energies. It is possible, within the VASP program, to define an initial magnetic moment on each atomic species, and the total number of unpaired electrons within the simulation cell. The individual moments are allowed to change during the simulation, but the total number of unpaired electrons is fixed throughout the calculation.

From traditional transition metal chemistry it seems likely that in the spinel $Li_2M_4O_8$, the metal species will be a mixture of M(III) and M(IV), while in the delithiated phase, M_4O_8, there will be only M(IV) present. From their relative positions within the periodic table, it is expected that any cobalt will be reduced before manganese, and therefore, in the mixed metal spinels, the oxidation-states are defined as $Li_2Co(III)Mn(III)Mn(IV)_2O_8$, $LiCo(III)Mn(IV)_3O_8$, $Li_2Co(III)_2Mn(IV)_2O_8$, and $LiCo(III)Co(IV)Mn(IV)_2O_8$. While Mn(III) is d^3 and Mn(IV) is known to favour high-spin d^4, some ambiguity remained over Co(III), thought to be low-spin d^6, and d^5 Co(IV). The preference of Co(III) and Co(IV) for high- or low-spin has also been investigated.

The sixteen metal atoms in the spinel unit cell have divided into four groups of four (M(1) to M(4) in Table 5.5), which allows us to find the low energy spin configuration for each species and the most stable arrangement of these spins within the simulation cell. The results of the single point calculations are detailed in Table 5.5.

Spinel phase	Initial size and direction of spin*				Total spin	Total Energy / eV
	M(1)	M(2)	M(3)	M(4)		
$Li_2CoMn_3O_8$	Co (4↑)	Mn (4↓)	Mn (3↑)	Mn (3↓)	0	-405.72
$Li_2CoMn_3O_8$	Co (0)	Mn (2↑)	Mn (3↑)	Mn (3↓)	8	-403.32
$Li_2CoMn_3O_8$	Co (0)	Mn (4↓)	Mn (3↑)	Mn (3↑)	8	-407.25
$Li_2CoMn_3O_8$	Co (1↓)	Mn (3↓)	Mn (3↑)	Mn (3↑)	8	-407.25
$Li_2CoMn_3O_8$	Co (0)	Mn (2↓)	Mn (3↑)	Mn (3↑)	16	-407.34
$Li_2CoMn_3O_8$	Co (0)	Mn (4↑)	Mn (3↑)	Mn (3↓)	16	-407.34
$Li_2CoMn_3O_8$	Co (4↑)	Mn (4↓)	Mn (3↑)	Mn (3↑)	24	-405.68
$Li_2CoMn_3O_8$	Co (0)	Mn (2↑)	Mn (3↑)	Mn (3↑)	32	-406.92
$Li_2CoMn_3O_8$	Co (0)	Mn (4↑)	Mn (3↑)	Mn (3↑)	40	-407.14
$Li_2CoMn_3O_8$	Co (4↑)	Mn (4↑)	Mn (3↑)	Mn (3↑)	56	-402.40
$CoMn_3O_8$	Co (1↓)	Mn (3↑)	Mn (3↓)	Mn (3↑)	8	-359.42
$CoMn_3O_8$	Co (5↓)	Mn (3↑)	Mn (3↓)	Mn (3↓)	8	-359.42

Table 5.5. Energies of various spin configurations for $Li_xCo_yMn_{4-y}O_8$.

*Species are defined in terms of their unpaired electrons, i.e. Co(0) is low-spin Co(III), Co(4) is high-spin Co(III), Co(1) is either low-spin Co(II) or Co(IV), and Co(5) is high-spin Co(IV). Mn(4) and Mn(2) are high- and low-spin Mn(III) respectively, and Mn(3) is Mn(IV).

The results outlined in Table 5.5 seem to indicate that the total energy is only dependent on the total number of unpaired electrons in the unit cell, and not affected by the initial magnetic moments on the individual metal ions. It is assumed that the optimisation procedure finds the lowest energy configuration for a given number of unpaired electrons, and this is certainly the case for $CoMn_3O_8$, where the final electronic distribution for both calculations was found to be identical.

An analysis of the optimised electron density distribution for $CoMn_3O_8$, using a spherical integration of the spin density around each metal atom, indicates that the Co ions have a spin of –1/2 and the Mn ions are either +3/2 or –3/2, in a ratio of 2:1. This analysis suggests that the Co(IV) ions are low-spin d^5, with a single unpaired electron.

The total energies from the single point calculations of the $Li_2CoMn_3O_8$ phase suggest that low-spin Co(III) is more stable, which is in agreement with general literature on cobalt oxides (Cotton and Wilkinson 1980). It is difficult to differentiate between high- and low-spin Mn(IV), which is a result of the way in which the DFT calculation tends to 'spread' an average spin over all the Mn atoms. By analysing the electronic density distribution of the most stable $Li_2CoMn_3O_8$ configuration, it was found that two groups of Mn ions had spins of over 3/2, and that the spin densities most closely resembled the highlighted configuration in Table 5.5. In summary, these single-point calculations have shown that Co(III) and Co(IV) both favour the low-spin configuration, while Mn(IV) can be treated as high-spin, as expected.

5.2.3.2 Structural Aspects

Optimised total energies for all the simulated $Li_xCo_yMn_{4-y}O_8$ phases are detailed in Table 5.6, while the unit cell parameters are given in Table 5.7. Individual magnetic moments on each species are those outlined in the previous section, while, wherever possible, an anti-parallel arrangement is favoured so that the total number of unpaired electrons within the simulation cell is minimised.

	Total energies / eV		
Spinel phase	x = 0	x = 1	x = 2
$Li_xCo_4O_8$	-311.54	-337.47	-362.09
$Li_xCo_2Mn_2O_8$	-346.24	-372.43	-396.56
$Li_xCoMn_3O_8$	-364.27	-389.93	-410.41
$Li_xMn_4O_8$	-382.51	-404.55	-425.25

Table 5.6. Optimised total energies for $Li_xCo_yMn_{4-y}O_8$ phases.

	x = 0			x = 1			x = 2		
Spinel phase	*a* / Å	*b* / Å	*c* / Å	*a* / Å	*b* / Å	*c* / Å	*a* / Å	*b* / Å	*c* / Å
$Li_xCo_4O_8$	8.008	8.070	8.013	8.061	8.043	8.040	8.055	8.061	8.062
$Li_xCo_2Mn_2O_8$	8.098	8.118	8.026	8.127	8.123	8.076	8.145	8.145	8.103
$Li_xCoMn_3O_8$	8.123	8.106	8.123	8.159	8.133	8.159	8.137	8.230	8.253
$Li_xMn_4O_8$	8.160	8.145	8.160	8.257	8.127	8.257	8.432	8.032	8.431

Table 5.7. Optimised unit cell parameters for $Li_xCo_yMn_{4-y}O_8$ phases.

It can be seen from the calculated cell parameters that the geometry optimisation procedure breaks the cubic symmetry of the spinel lattice, regardless of the A site cation distribution. In the $Li_xCo_4O_8$ and $Li_xMn_4O_8$ phases, the removal of some of the symmetry elements is a result of the way in which the transition metal species are defined, a technical detail of the simulation. We assume that, for these phases where x = 0 and x = 2, the asymmetric lattice parameters are a result of the use of finite convergence criteria in the calculation.

	Unit cell volume / $Å^3$		
Spinel phase	x = 0	x = 1	x = 2
$Li_xCo_4O_8$	517.81	521.23	523.49
$Li_xCo_2Mn_2O_8$	527.55	533.17	537.48 (522.05)
$Li_xCoMn_3O_8$	534.75	541.33	552.59 (537.76)
$Li_xMn_4O_8$	542.38	554.05	570.89 (561.11)

Table 5.8. Optimised cell volumes for $Li_xCo_yMn_{4-y}O_8$ spinel phases with experimental values in brackets (Kawai 1998b, Kawai 1999).

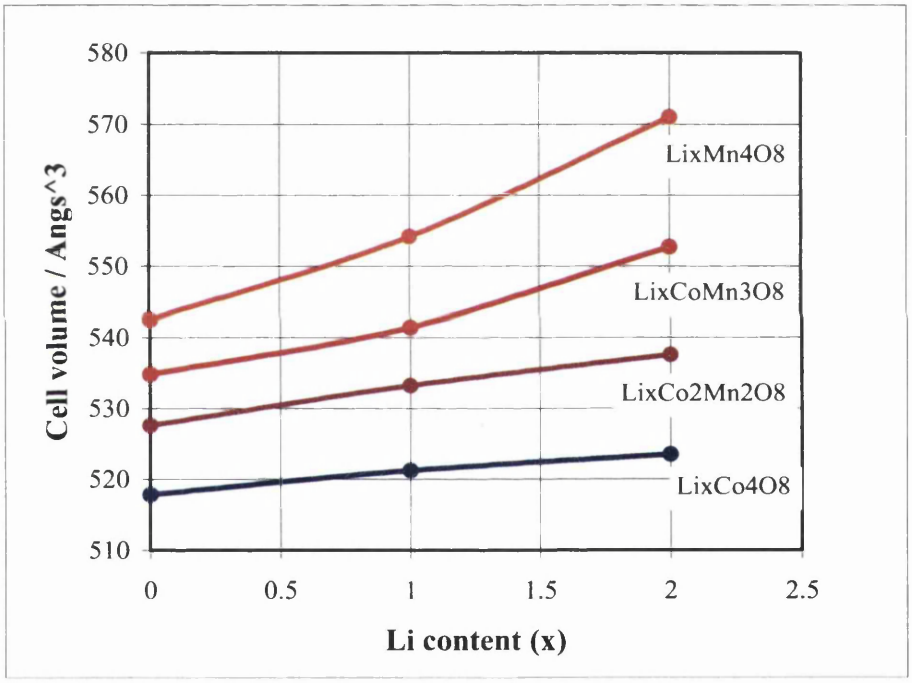

Fig. 5.5. Optimised cell volumes for $Li_xCo_yMn_{4-y}O_8$ spinel phases.

Optimised unit cell volumes are given in Table 5.8 and displayed in Fig 5.5. As expected, the cell volume increases as the concentration of Mn within the lattice increases, a result of Mn ions having larger ionic radii. In general, there is an expansion of the spinel unit cell as lithium is incorporated, although the rate of expansion is dependent on the Co : Mn ratio. At low concentrations of Mn ions, the volume increase

on lithium intercalation is small, which is again believed to be due to the smaller ionic radius of Co, which would result in larger tetrahedral sites for the intercalated lithium ions to occupy. The calculated cell parameters are within 1% of experimental values, although there is a consistent overestimation of the cell volume that is indicative of the DFT technique.

5.2.3.3 Cell voltages

Using the methods described in Chapter 3, we have predicted the average cell voltages between limiting compositions defined by the calculated phases. Using the optimised total energies from Table 5.6, we can predict an average voltage for composition changes between x = 0 to 1, and x = 1 to 2, corresponding to the two plateaux that are seen experimentally in the discharge curve of spinel cathode materials. Calculated average cell voltages are detailed in Table 5.9.

	Average cell voltage / V	
Spinel phase	x = 0.5	x = 1.5
$Li_xCo_4O_8$	4.58	4.25
$Li_xCo_2Mn_2O_8$	4.64 (5.2)	4.13 (4.9)
$Li_xCoMn_3O_8$	4.51 (5.1)	3.22 (3.9)
$Li_xMn_4O_8$	3.61 (4.1)	3.27 (3.9)

Table 5.9. Calculated average cell voltages for the $Li_xCo_yMn_{4-y}O_8$ system with experimental measurements, where available, in brackets (Kawai 1998b, Kawai 1999).
Voltages are calculated for an average composition between the simulated limits.

If we apply the same offset of around 0.5V, which has been seen between calculation and experiment in all our DFT work, then there is good agreement between the predicted voltages for $Li_xCoMn_3O_8$ and the experimentally measured values. This result gives us confidence that the predicted average voltages for the remaining spinel phases can be relied on to give a good estimate of the experimental value. The data in Table 5.9 appear to confirm that it is the presence of cobalt atoms within the cathode material that results in discharge voltages over 5 V, as there is a clear correlation between the composition of the spinel host and the predicted average voltage obtained for each plateau on the discharge curve. Assuming that reduction of Co centres, if present, will take place before Mn, then the results suggest that the Co redox process occurs at potentials around 5 V, while the Mn redox occurs at around 4 V.

To investigate the effect of the cobalt redox processes in more detail, Density Functional Theory has been used to simulate the cathode material $LiCoO_2$, and the delithiated phase, CoO_2. These calculations will allow us to calculate an average cell voltage for this well known cathode material, where there is no doubt that the redox process that is involved is Co(III) $\leftrightarrow$ Co(IV). The structure of $LiCoO_2$ has already been described (Fig. 5.3) as a hexagonal structure, consisting of alternate layers of CoO_6 octahedra and Li atoms. A 2 x 2 x 1 supercell has been used in the calculation, to create a simulation cell with more even dimensions. The optimised structure is compared to experiment in Table 5.10, while Table 5.11 contains the optimised total energies of both $LiCoO_2$ and CoO_2.

	Experiment	Calculated	Error / %
Cell Volume ($Å^3$)	386.17	396.48	2.67
a / Å	5.633	5.713	1.42
c / Å	14.052	14.027	0.18

Table 5.10. Experimental (Johnston 1958) and calculated unit cell dimensions for $LiCoO_2$.

Phase	Total energy / eV
$LiCoO_2$	-299.421
CoO_2	-234.148

Table 5.11. Optimised total energies for $LiCoO_2$ and CoO_2.

The hexagonal structure of $LiCoO_2$ remains intact after the removal of the lithium ions, with a contraction of the *a* and *b* unit cell parameters by 0.75%. There is virtually no change to the *c* parameter. The calculated total energies predict an average cell voltage, between the compositions CoO_2 to $LiCoO_2$ of 3.54 V, which is in good agreement with the experimental value for the $LiCoO_2$ cathode material of 4.0-4.1V (Ohzuku 1994), although we accept that the calculated value covers a large change in composition.

Assuming that the Co(III) ↔ Co(IV) redox is responsible for the cell voltage in both the layered cobalt oxide, Li_xCoO_2, and the spinel phase, $Li_xCoMn_3O_8$, the calculated voltages for each material indicate that the same redox process can generate a wide range of cell voltages. We suggest that it is the band structure, and therefore the local environment of the cobalt atom that must produces the 1V difference between the

materials and that the cell voltage is a function of the structure of a material, not just the metal atoms that are present.

In the next section we will study the optimised electronic distribution from the DFT calculations, which should yield detailed information about the transition metal oxidation-state changes that accompanies lithium intercalation into the spinel structure.

5.2.3.4 Electronic Structure

As described previously for $Li_xV_2O_5$ and $Li_xV_6O_{13}$, we use spherical integration of the charge around selected atoms and contour plots of the difference between two electronic density distributions to investigate the electronic structure of the spinel phases. The electron spin density, the difference between the distributions of up- and down-electrons, has also been analysed. We concentrate on two spinels, $Li_2CoMn_3O_8$ and $Li_2Co_2Mn_2O_8$, where the involvement of both cobalt and manganese is important in the generation of the cell voltage.

Firstly, we look at the electronic populations of symmetry unique atoms in $Li_2CoMn_3O_8$ and $Li_2Co_2Mn_2O_8$ by carrying out a spherical integration of the electronic density around certain Co and Mn species. This integration is also carried out around an oxygen atom so that a comparison can be made. This integration is carried out over a range of radii from the atom centre, and allows us to study the charge, ionic radii, and spin of each atomic species.

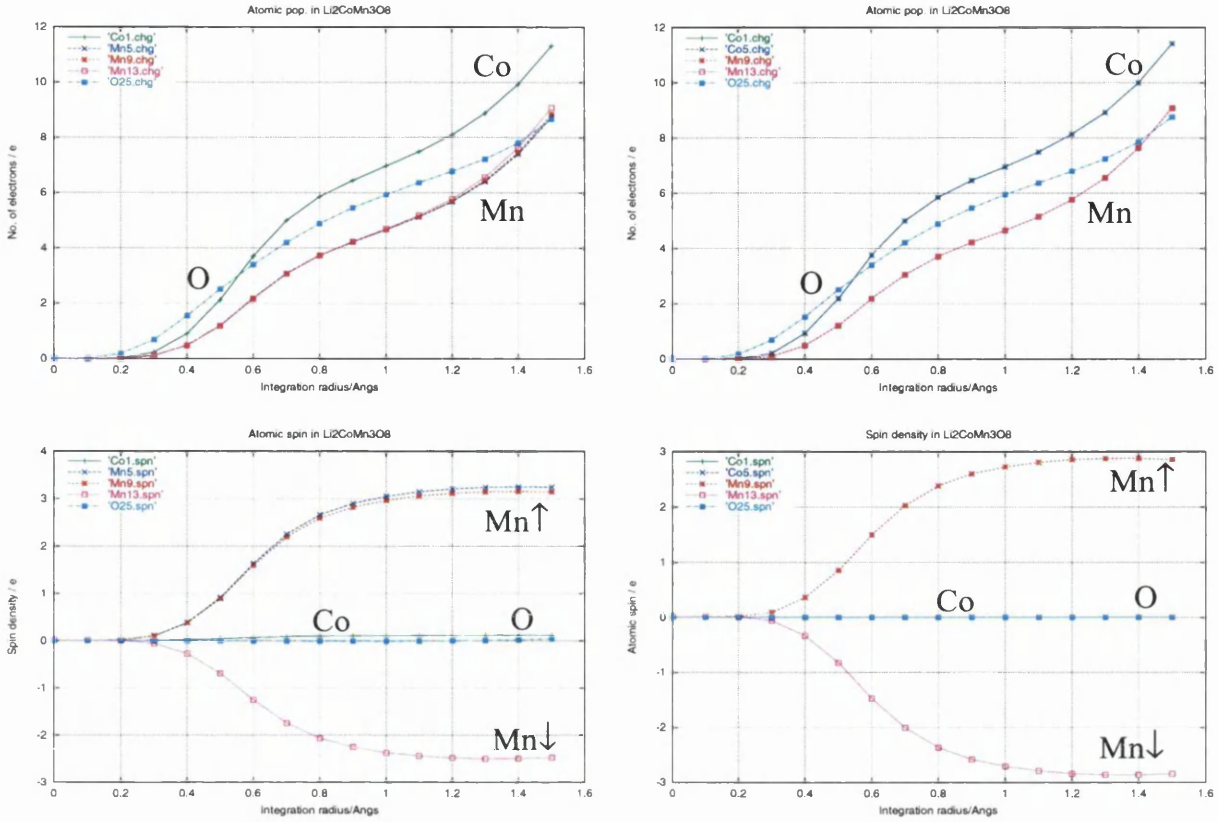

$Li_2CoMn_3O_8$ $Li_2Co_2Mn_2O_8$

Fig. 5.6. Spherical integration of the electronic charge density (top) and spin density (bottom) distribution around the unique atom positions in $Li_2CoMn_3O_8$ and $Li_2Co_2Mn_2O_8$.

From the plots in Fig. 5.6 we can estimate the ionic radii and the oxidation-state of each transition metal species by locating the point of inflection in the plot of charge against integration radius. Although this is a relatively coarse way of analysing the electron density, it has already been shown for vanadium in V_6O_{13} that the electron cloud around the ion is spherical (section 4.2), and the procedure allows a comparison with traditional approaches to transition metal chemistry, which would predict the presence of Co(III) and a mixture of Mn(III) and Mn(IV).

Initially, we note that all the cobalt and manganese atoms are essentially identical, not only within the same phase, but also between phases. There is no division of the manganese into Mn(III) and Mn(IV) in the $Li_2CoMn_3O_8$ phase. Assuming an ionic radius of around 1 Å for both Co and Mn suggests cobalt is a d^7 ion while manganese is d^5, indicating the presence of Co(II) and Mn^{II}. These predicted oxidation-states are lower than expected.

The integration of the density around the oxygen atoms, which are also identically charged in both spinel phases, indicates that an ionic radius of 1.4Å is required before sufficient density is included to give O^{2-}. As all M-O distances in these spinel phases are in the region of 2.0 to 2.1Å, this seems to suggest either a degree of covalent bonding, or that the ionic radii of the metal species have been overestimated. Subtracting the ionic radius of the O^{2-} ion from the average bond length gives an ionic radius of around 0.7Å for the metal ions. The integration of the charge within 0.7Å takes in 5 electrons around the Co atoms and 3 electrons on Mn, which would give Co(IV) and Mn(IV), oxidation-states closer to what is expected.

The integration of the spin density around the metal centres shows that the cobalt in both phases has no magnetic moment, and is likely to be low-spin Co(III). The Mn are split into spin-up and spin-down groups that roughly correspond to Mn(IV). Integration around an oxygen atom confirms that there are no unpaired electrons present on the anions.

We compare the oxidation-state of cobalt in the spinel phases, $Li_2CoMn_3O_8$ and $Li_2Co_2Mn_2O_8$, with that in the hexagonal layered material, $LiCoO_2$, by integrating the electron density around the Co and O atoms. Fig. 5.7 shows the electronic populations of Co and O atoms in $LiCoO_2$ and the delithiated host, CoO_2.

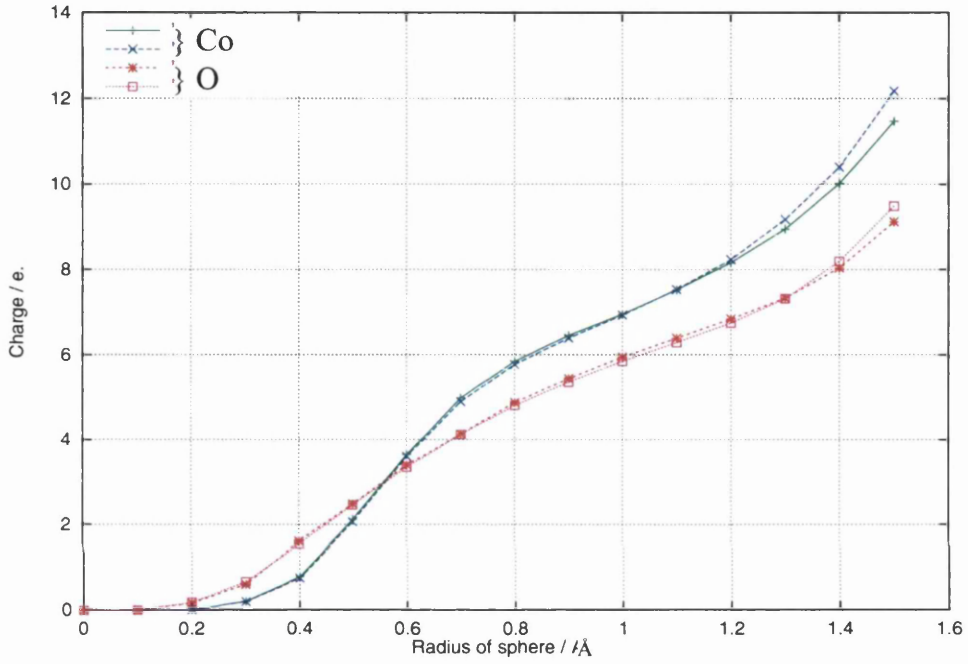

Fig. 5.7. Integrated electron density around Co (green) and O (red) atoms in $LiCoO_2$, and Co (blue) and O (mauve) atoms in CoO_2.

A comparison of the data in Figs. 5.6 and 5.7 shows that the Co atoms, in both the spinel phases and $LiCoO_2$, are in an identical oxidation-state and that little reduction of the Co centres occurs during lithium insertion in $LiCoO_2$.

A more detailed picture of the electronic rearrangement that accompanies lithium insertion into the $Li_2CoMn_3O_8$ phase can be obtained from the difference between the electron density distribution in the lithiated and delithiated phases. This technique has been used in the previous chapters on the $Li_xV_2O_5$ and $Li_xV_6O_{13}$ systems and highlights

the location of the 'new' electrons that accompany the insertion of Li^+ ions. This density difference is integrated in the same way as in the previous section and it was found that the four cobalt ions are identical while the manganese are split into three groups of four identical ions. The 32 oxygen atoms are also split into groups of four, and here again the ions are identical within each group. The plots in Figure 5.8 show an example from each grouping, so that every ion in the unit cell is represented.

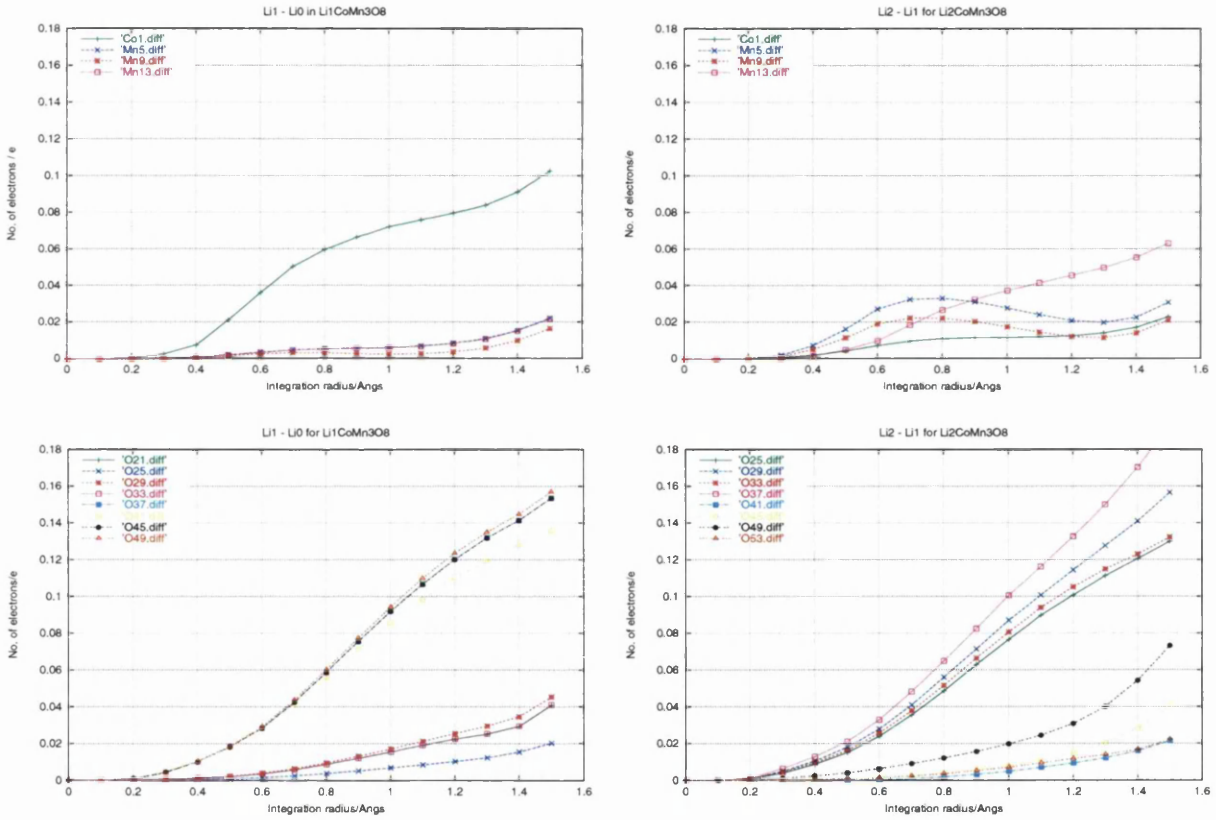

'$Li_2CoMn_3O_8$' – '$LiCoMn_3O_8$' '$LiCoMn_3O_8$' – '$CoMn_3O_8$'

Fig. 5.8. Density difference plots for two stages of lithium intercalation: '$Li_2CoMn_3O_8$' – '$LiCoMn_3O_8$'and '$LiCoMn_3O_8$' – '$CoMn_3O_8$'. Spherical integration around unique Co (green) and Mn (blue, red, and purple) ions (top), and unique oxygen atoms (bottom) are shown.

By generating the difference density distribution for two stages of lithium intercalation, it is possible to study the changes to the electronic structure that produce both plateaux

on the discharge curve. In general, the involvement of the transition metal atoms during the intercalation process is surprisingly low. The cobalt ions gain a small amount of electron density (< 0.1e) during the first insertion stage, from x = 0 to x = 1, while the manganese ions are essentially unaffected. During the second stage of lithium incorporation, from x = 1 to x = 2, the cobalt remain unchanged while a small amount of electronic rearrangement occurs at the manganese centres. It is noted that, during this second stage, some Mn ions gain more electron density than others do.

In contrast, the oxygen atoms all gain electron density during lithium intercalation, and in larger amounts than that seen for the metal ions. Half the oxygens play a more important role in the first stage of lithium insertion, while the remaining anions gain the majority of their electron density between $1 \leq x \leq 2$. As there are 32 oxygens in the unit cell, compared to only 16 metal ions, it is clear that it is the oxygen atoms that accept the majority of the electron density that accompanies lithium insertion into these spinel materials. Indeed, we estimate that approximately 70% of this electron density is found on the oxygen ions, which has important implications, as it runs against the traditional view of the way in which redox process take place in transition metal oxides.

We have also used a series of contour plots, representing 2-dimensional cross-sections of the difference density, for '$Li_2CoMn_3O_8$' – '$LiCoMn_3O_8$' and '$LiCoMn_3O_8$' – '$CoMn_3O_8$', so that detailed changes in the electronic structure can be studied. The most informative of these plots are shown in Fig. 5.9, with details of the positions of the cross-sections and atoms through which they cut.

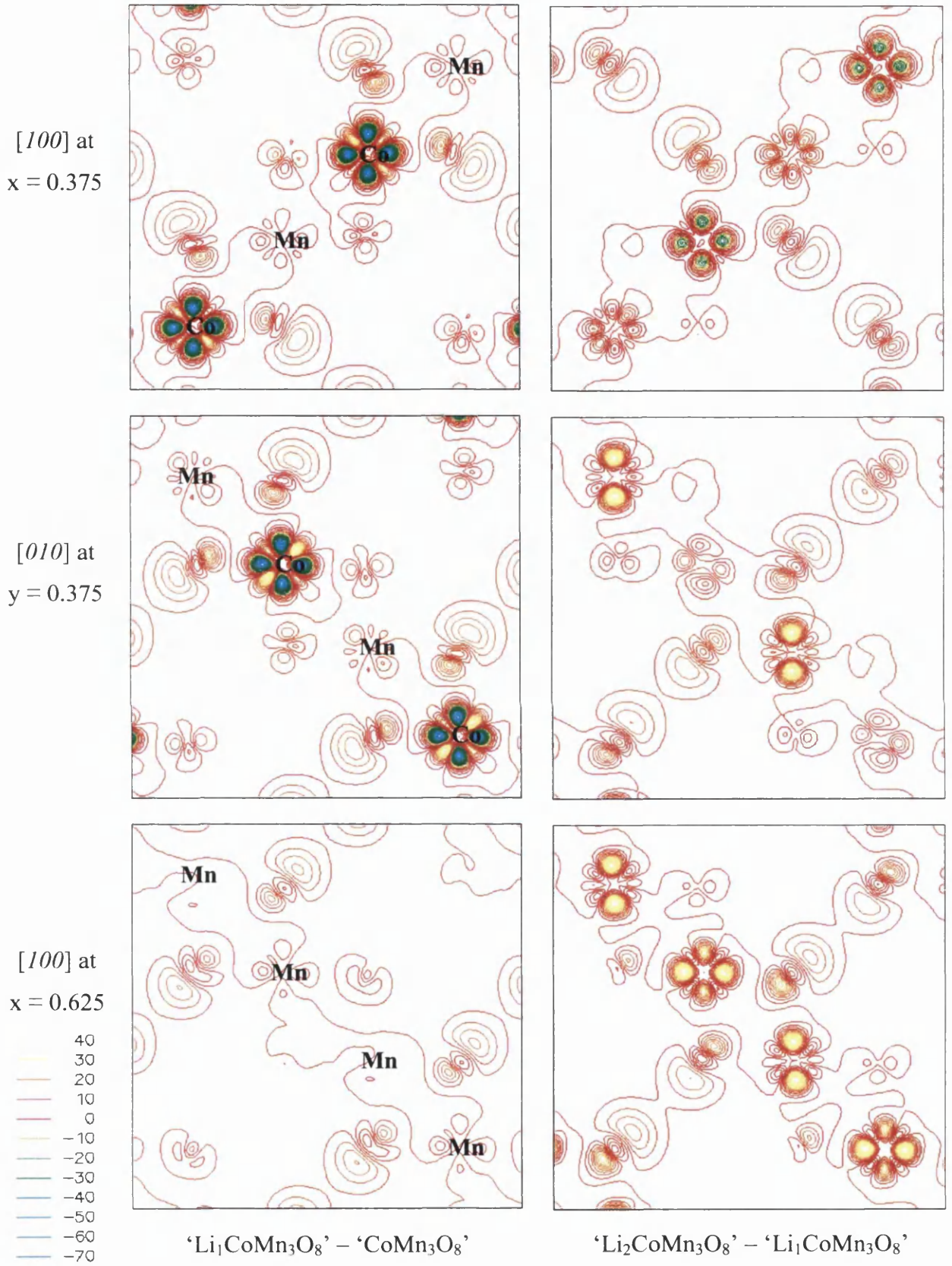

Fig. 5.9. Contour plots, in $10^2 e/Å^2$, of the electron difference density in $Li_xCoMn_3O_8$, with green and blue areas indicating negative density, zero density is light red, and positive density is shown in yellow.

The contour plots in Fig. 5.9 confirm that that only the cobalt atoms are affected during the first stage of lithium intercalation, and that the manganese are the only metal atoms involved in the second stage. There is also evidence of significant amounts of electron loss from certain '*d*-like' orbitals on the cobalt atoms, even though, overall, these atoms gain electron density during lithium insertion. The oxygens atoms that are co-ordinated to the cobalt ions also gain small amounts of electron density, while those around the manganese appear to be unaffected.

The manganese atoms are reduced as the lithium concentration, x, increases from 1 to 2, although not all the Mn centres are identical, certain atoms gain more electron density than others. From the contour plots it also appears as if this density is localised in a number of different Mn orbitals, depending on which atom is reduced, although this may just be a result of the exact position and direction in which the cross-section through the density is taken.

The electron density changes around a single cobalt and manganese atom are investigated in more detail in Fig. 5.10, using the difference density, '$Li_2CoMn_3O_8$' – '$CoMn_3O_8$', which is plotted within the proximity of each atom.

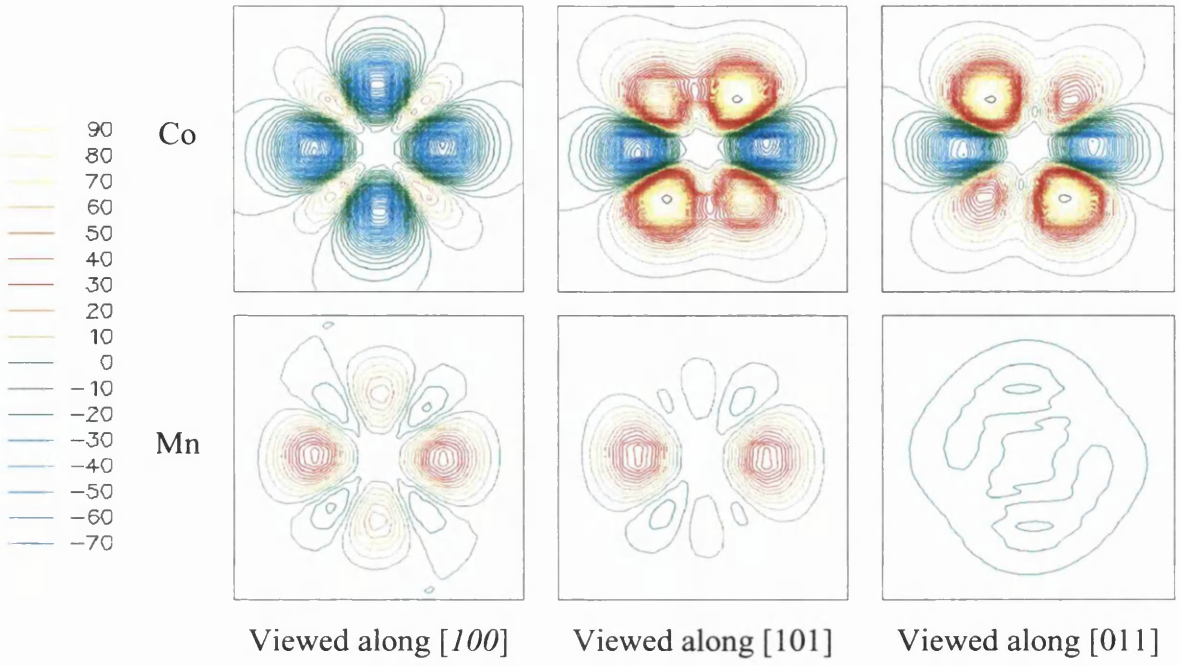

Fig. 5.10. Electron density difference, in $10^2 e/Å^2$, '$Li_2CoMn_3O_8$' – '$CoMn_3O_8$' at a cobalt and a manganese atom.

The contour plots in Fig. 5.10 show that the electrons that accompany lithium intercalation occupy different orbitals on the Co and Mn ions. The electrons localised on the manganese populate a single, four-lobed, '*d*-like' orbital that is orientated in the *bc* plane, which is analogous to an e_g orbital in classic ligand field theory. This is consistent with an oxidation state change from d^3 Mn(IV) to high-spin d^4 Mn(III). The electronic structure around the cobalt ion is considerably more complex: significant electron loss occurs from orbital lobes that are orientated along the crystal axis, while eight lobes, pointing towards the faces of the CoO_6 octahedron, are populated. It is impossible to make a simple comparison with ligand-field theory as some type of complex electronic reorganisation appears to take place. There is a greater degree of

reduction of the cobalt atoms, although this is likely to relate to the relative numbers of the atomic species.

The positions of the populated cobalt orbitals explains why the Co atoms appear to lose electron density in Fig. 5.9, while the integration of the charge around the ions, in Fig. 5.8 shows an overall gain in electron density.

We have used the same method, of subtracting lithiated and delithiated electronic density distributions from each other, to study the effects of lithium intercalation in $Li_2Co_2Mn_2O_8$. The resulting contour plots are shown in Fig. 5.11.

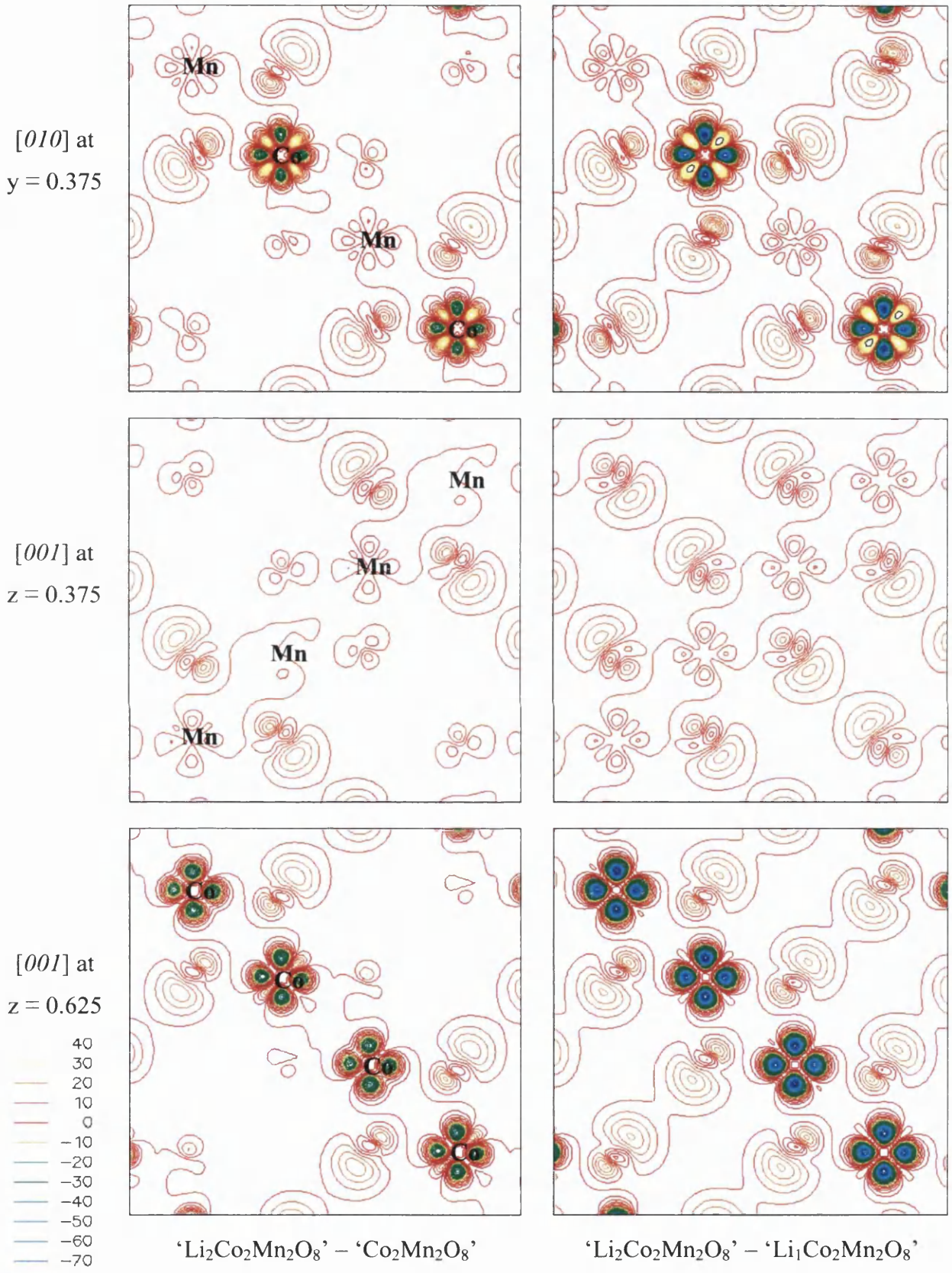

Fig. 5.11. Contour plots, in $10^2 e/Å^2$, of the electron difference density in $Li_xCo_2Mn_2O_8$, with green and blue areas indicating negative density, zero density is light red, and positive density is shown in yellow.

Similar trends to those seen in $Li_2CoMn_3O_8$, are present in the $Li_2Co_2Mn_2O_8$ phase, the significant difference being the involvement of the cobalt atoms during both stages of lithium insertion, while the manganese remain unchanged, even at higher lithium concentrations where x = 2. The loss of electron density from orbital lobes that are orientated along the crystal axis is similar to the electron loss seen in the $Li_xCoMn_3O_8$ phase, although the effect, in this case, is even more pronounced. Another common feature between the $Li_xCoMn_3O_8$ and the $Li_xCo_2Mn_2O_8$ phases is the presence of additional electron density on the oxygens co-ordinated to the cobalt atoms, while those surrounding the manganese atoms are unaffected by the intercalation process.

5.2.3.5 Density of States

The possible involvement of the oxygen atoms in the redox processes that accompany lithium insertion has been proposed in a number of theoretical studies by Mackrodt *et al* (1996, 1998), in which they suggest that electron holes in the oxygen *2p* band are filled by the electrons due to the intercalation reaction. The difference density plots in Figs. 5.9 and 5.11 appear to show that oxygen orbitals are populated during the insertion of lithium into both $Li_xCoMn_3O_8$ and $Li_xCo_2Mn_2O_8$ spinels, although these effects may be a result of electronic rearrangements, such as a reduction in the covalent bonding between oxygen and metal.

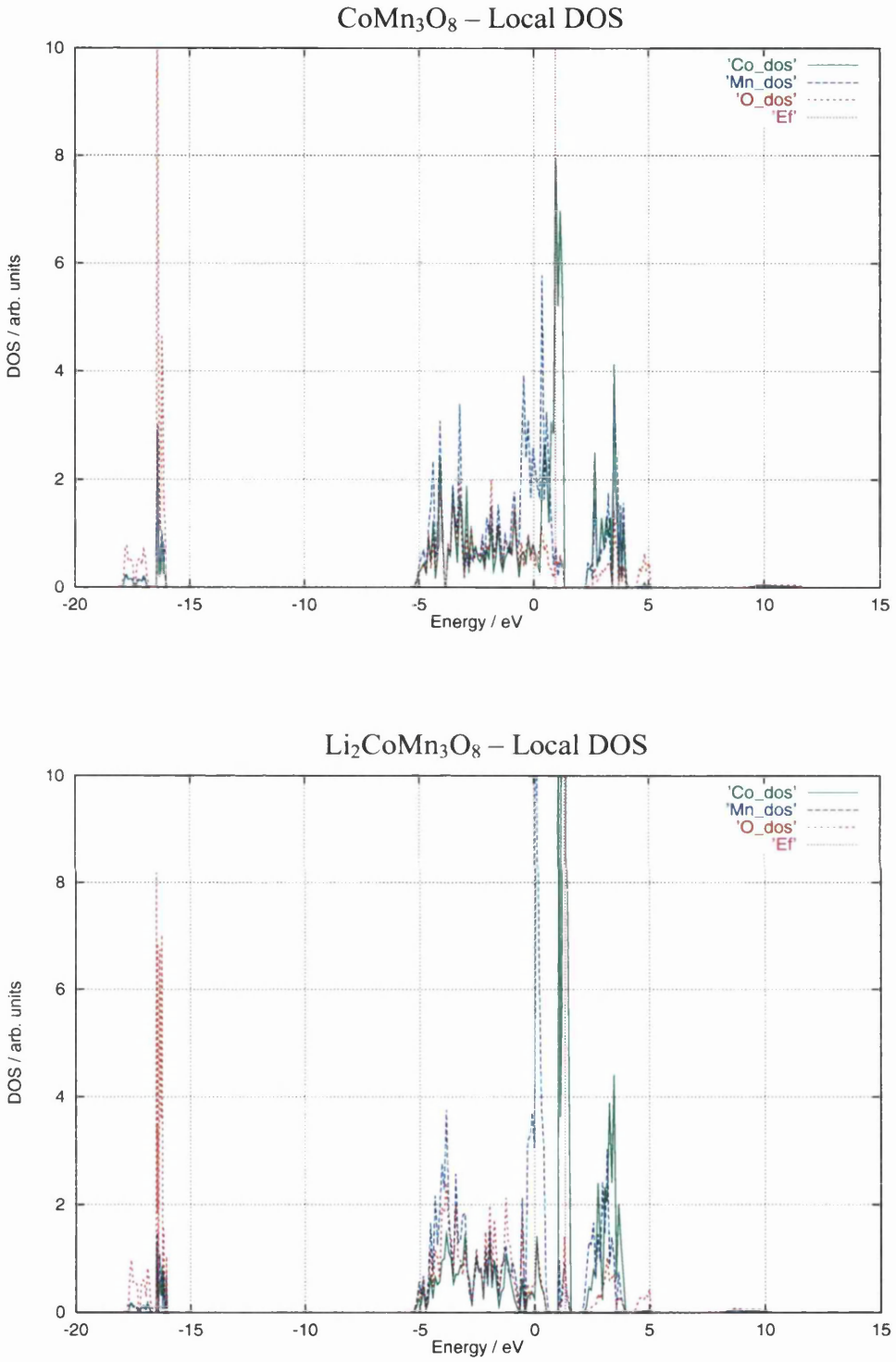

Fig. 5.12. Local valence electron density of states for $CoMn_3O_8$ (top) and $Li_2CoMn_3O_8$ (bottom), for Co (green), Mn (blue), and O (red). The Fermi level is shown in purple.

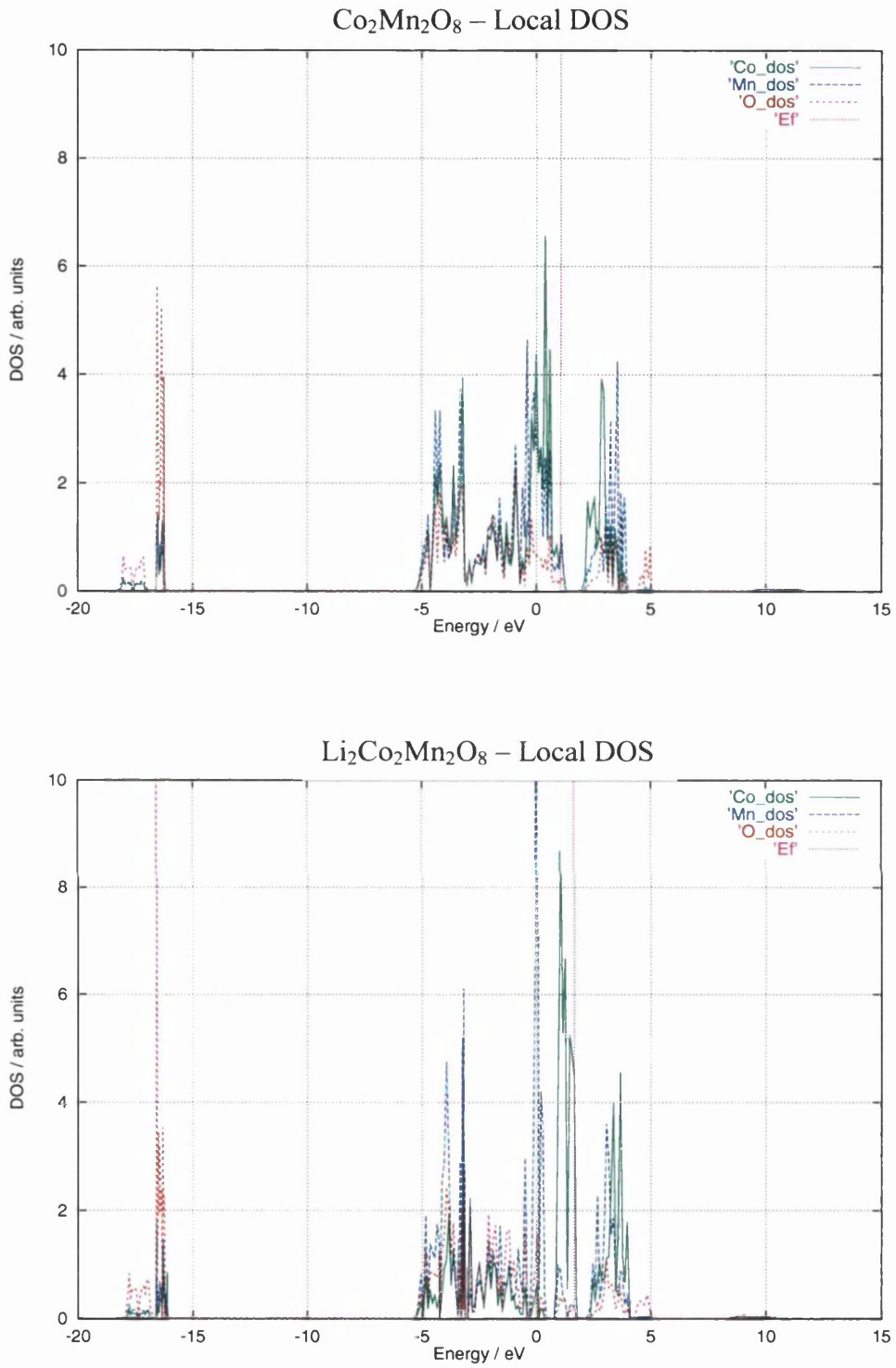

Fig. 5.13. Local valence electron density of states for $Co_2Mn_2O_8$ (top) and $Li_2Co_2Mn_2O_8$ (bottom), for Co (green), Mn (blue), and O (red). The Fermi level is shown in purple.

In an attempt to show conclusively whether there is population of oxygen *2p* orbitals during lithium incorporation we have generated plots of the local density of states

(LDOS) for a single Co, Mn, and O atom in both $Li_xCoMn_3O_8$ and $Li_xCo_2Mn_2O_8$, for x = 0 and x = 2. Due to the pseudopotential method used, only valence electrons are included in the LDOS calculation. The valence electrons included for each species are $d^8\ s^1$ for Co, $d^6\ s^1$ for Mn, $s^1\ p^0$ for Li, and $s^2\ p^4$ for O. These plots are shown in Fig. 5.12 and 5.13.

A number of general trends are evident from Figs. 5.12 and 5.13. Lithium intercalation reduces the band gap, by approximately 0.5eV in both spinel phases, a result of stabilisation of the e_g levels by the inserted Li^+ ions, while the band gap in $Co_2Mn_2O_8$ is smaller than that in $CoMn_3O_8$ due to the increased nuclear charge in the unit cell. As expected, oxygen states are dominant at low energies, while the Co and Mn local density of states are concentrated in two bands around the Fermi level, assumed to be t_{2g} and e_g in character. The sharp peaks seen in all the simulated LDOS plots are likely to be a result of the relatively small k-point grid that was used in the calculation. Unfortunately, the use of a more accurate k-point grid was impractical due to the increased computational cost.

As expected, lithium intercalation shifts the Fermi level up in energy in both spinel phases, although population of the e_g band is not seen in either $Li_2CoMn_3O_8$ or $Li_2Co_2Mn_2O_8$. Some oxygen p states are also present around the Fermi level, which could indicate some population of O $2p$ levels during lithium insertion reactions, although some form of population analysis would be required if the presence of electron holes on the oxygen atoms is to be confirmed. Apart from the slight reduction in the band gap, the concentration of cobalt seems to have little effect on the band structure

around the Fermi level, although the density difference plots indicate that, in $Li_2Co_2Mn_2O_8$, the bands around the Fermi level are dominated by cobalt *d* states.

5.3 Summary

We have shown, using a combination of atomistic and electronic structure modelling techniques, that mixed metal spinels of the general formula, $Li_xCo_yMn_{4-y}O_8$, are promising cathode materials for solid-state lithium-ion batteries. By simulating a number of spinel phases with varying cobalt content, we show that the concentration of cobalt within the structure determines the extent of the 5V plateau in the cell discharge curve, which has later been shown to be the case experimentally (Kawai 1999). The origin of the unusually high voltages generated by these materials is related to the spinel structure, not just the redox process at the metal centres, as the calculated average voltage for the hexagonal Li_xCoO_2 is almost 1V lower, even though the change in the cobalt oxidation-state is identical.

In a detailed study of the changes to the electronic structure that accompanies lithium intercalation in $Li_xCoMn_3O_8$, we show, as expected, that extensive electronic rearrangement takes place around the cobalt atoms during the first stage of lithium insertion, while the manganese atoms are involved as the lithium concentration increases from x = 1 to x = 2. The atomic orbitals that are occupied on the cobalt atoms are different from the occupied orbitals on the manganese atoms. We also note that considerable amounts of electron density, due to the intercalated lithium ions, are localised on the oxygen atoms.

In $Li_xCo_2Mn_2O_8$, an examination of the electronic distributions of the lithiated and delithiated phases shows that only the cobalt atoms gain electron density during lithium insertion. The manganese atoms are unchanged during the intercalation process.

Calculated local density of states has been used to show that lithium intercalation reduces the band gap in spinel phases, $Li_2CoMn_3O_8$ and $Li_2Co_2Mn_2O_8$, while the concentration of cobalt appears to have little influence on the band structure. We note that oxygen *p* states are present around the Fermi level in both $Li_2CoMn_3O_8$ and $Li_2Co_2Mn_2O_8$, indicating that oxygen is likely to be involved in the redox processes accompanying lithium insertion.

Chapter 6

Conclusions

The demand for lithium ion battery technology is steadily increasing as the market for portable electronic devices, such as mobile phones and laptop computers, grows ever larger. As developed countries look to reduce their reliance on fossil fuels, and move towards renewable energy sources, then large industrial scale and small residential scale electrical storage devices will be of increasing importance. Electric vehicles are another huge area for potential growth in battery demand.

We have used a combination of interatomic potential based simulation and electronic structure methods to study the effects of lithium intercalation into three potential cathode materials. The structural effects of lithium insertion in V_2O_5, a layered oxide, and the three-dimensional lattice of V_6O_{13}, can be reproduced correctly using *ab initio* techniques. These results confirm that simulation from first-principles can be used to test the structural response of a wide range of transition metal oxides, with either accessible cavities within the lattice or weakly bonded layers.

Optimised total energies from Density Functional calculations have been used successfully to predict average voltages for the $Li_xV_2O_5$, $Li_xV_6O_{13}$, and $Li_xCo_yMn_{4-y}O_8$ cathode materials using a simple thermodynamic approach. Although calculated voltages underestimate experiment by about 0.5V, the consistency of this error means that DFT methods can still be used as a predictive tool to measure the voltages generated by new transition oxide materials and to investigate the effects of doping with other metal species. As an example of this, we correctly predicted the dependence of the cell voltage on cobalt concentration in the series of spinel structures, $Li_xCo_yMn_{4-y}O_8$.

The changes induced by lithium incorporation to the electronic structure of the host oxide have been studied using calculated electron density distributions and density of states. As expected, we find that lithium is fully ionised when intercalated into a transition metal oxide host. In the vanadium oxides, the electrons that accompany the Li^+ ions are almost totally localised on the vanadium atoms. At low lithium concentrations, there is selective reduction of the vanadium centres that are in the proximity of the intercalated Li^+ ions and therefore there is no population of a delocalised band due to the vanadium *d* orbitals.

In the spinel phases, the intercalation of lithium resulted in the population of orbitals on both the metal and, to a limited degree, the oxygen ions. The generation of discharge voltages over 5V is a result of electronic population of orbitals localised on the cobalt atoms. If the concentration of cobalt was high enough, then the electronic environment of the manganese atoms remained unchanged by the intercalation reaction. Calculated local densities of states indicated that Co, Mn, and O states were all present in the region of the Fermi level, suggesting that oxygen *2p* states may have a role in

determining the size of the discharge voltage. Certainly, the local environment of the metal species has as important an influence on the voltage as the actual identity of the metal species does.

On a technical note, we suggest that using a combination of interatomic potential based simulation with high quality electronic structure methods is an effective approach when studying complex materials of this kind. Atomistic simulation is an efficient way of eliminating possible configurations of the system, and can be used to generate optimised geometries that can be refined using *ab initio* techniques. We also note that electron distributions from first principles calculations can be used, through the application of fitting and partial charges, to make an interatomic potential based description of a material more physically accurate.

In summary, we have shown that computational simulation techniques are a valuable tool for studying the electrochemically active cathode component in lithium ion batteries, although these methods can be equally well applied to either electrode. As computational power increases, we expect these theoretical techniques to become increasingly widely used in this area of solid-state research, and to be an effective way of searching for new, more effective, materials.

References

Aebi, F., *Helv.* (1948) *Chim. Acta* **31** 8

Amine, K., Tukamoto, H., Yasuda, H., Fujita, Y., (1996) *J. Electrochem Soc.*, **143** 1607

Ammundsen, B., Rozière, J., Islam, M.S., (1997a) *J. Phys. Chem.* **101** 8156

Ammundsen, B., Islam, M.S., Jones, D.J., Rozière, J., (1998) *Mol. Liq. Cryst. Liq.*, **311** 109

Andersson, G., (1956) *Acta Chem. Scand.* **10** 623

Armand, M.B., Chabagno, J.M., Duclot, M.J., (1979) *Fast Ion Transport in Solids.* eds. Vashishita, P., Mundy, J.N. and Shenoy, G.K., p. 131. North-Holland, New York.

Aydinol, M.K., Kohan, A.F., Ceder, G., Cho, K., Joannopoulos, J., (1997a) *Phys. Rev. B* **56** 1354

Aydinol, M.K., Ceder, G., (1997b) *J. Electrochem. Soc.*, **144** 3832

Badot, N. Baffier, (1992) *J. Mater. Chem.* **2** 1167

Benco, L., Barras, J-L., Daul, C.A., Deiss, E., (1999) *Inorg. Chem.*, **38** 20

Benedek, R., Thackeray, M.M., Yang, L.H., (1997) *Phys. Rev. B* **56** 10707

Baker, S., (1966) *Phys. Rev. Lett.* **17** 1286

Barker, J., Saidi, M.Y., Koksbang, R., (1996) *Electrochimica Acta* **41** 2639

Barker, J., Saidi, E.S., Saidi, M.Y., (1995) *Electrochimica Acta* **40** 949

Becke, A.D., (1988) *Phys. Rev. A,* **38** 3098

Bergström, Ö., Gustafsson, T., Thomas, J.O., (1997) *Acta Cryst.* **C53** 528

Bergström, Ö., Gustafsson, T., Thomas, J.O., (1998a) *Acta Cryst.* **C54** 1204

Bergström, Ö., Gustafsson, T., Thomas, J.O., (1998b) PhD Thesis, University of Uppsula.

Bergström, Ö., Gustafsson, T., Thomas, J.O., (1998c) *Solid State Ionics* **110** 179

Binks, D.J., (1994), PhD Thesis, Oct 1994. Chemistry Dept., University of Surrey.

Byström, A., Wilhelmi, K.A., Brotzen, O., (1950) *Acta Chem. Scand.*, **4** 1119

Catlow, C.R.A., (1977) *Proc. Roy. Soc.* **A353** 533

Catlow, C.R.A., Mackrodt, W.C., (1982a) (eds), *Computational simulation of solids*, Lecture Notes in Physics, **166**

Catlow, C.R.A., James, R., Mackrodt, W.C., Stewart, R.F., (1982b) *Phys. Rev. B* **25** 1006

Catlow, C.R.A., (1987), 'Computational Techniques and Simulation of Crystal Strutures', Chap7 of 'Solid Stata Chemistry - Techniques', ed. Cheetham and Day, Clarendon Press. P. 141-194.

Catlow, C.R.A., (1997), 'Computer Modelling as a Technique in Materials Chemistry' in 'New Trends in Materials Chemisty', eds. Catlow, C.R.A., and Cheetham, A., Kluwer Academic, Netherlands.

Cava, R.J., Santoro, A., Murphy, D.W., Zahurak, S.M., Fleming, R.M., Marsh, P., Roth, R.S., (1986) *J. Solid State Chem.* **65** 63

Ceder, G., Aydinol, M.K., Kohan, A.F., (1997) *Comput. Mater. Sci.* **8** 161

Ceder, G., Chiang, Y.-M., Sadoway, D.R., Aydinol, M.K., Jang, Y.-I., Huang, B., (1998) *Nature* **392** 694

Ceperley, D.M., Alder, B.J., (1980) *Phys. Rev Lett.* **45** 566

Chadi, D.J., Cohen, M.L., (1973) *Phys. Rev. B*, **8** 5747

Cocciantelli, J.M., Menetrier, M., Demas, C., Doumerc, J.P., Pouchard, M., Broussely, M., Labat, J., (1995) *Solid State Ionics* **76** 143

Cotton, F.A., Wilkinson, G., (1980), 'Advanced Inorganic Chemistry – A Comprehensive Text', Chap. 21-F, page 766. 4th edition. John Wiley and Sons

Courtney, I.A., Dahn, J.R., (1997) *J. Electrochem. Soc.*, **144** 2045

Davidon, W.C., (1959) *A.E.C. Research and Development Report*, ANL-5990

Day, A.N., Sullivan, B.P., (1972) *U.S. Pat. 3* **655** 585

Deiss, E., Wohaun, A., Barras, J.-L., Daul, C., Dufek, P., (1997) *J. Electrochem. Soc.* **144** 3877

Dick, B.G., Overhauser, A.W., (1958) *Phys. Rev* **112** 90

Dietrich, A., Catlow, C.R.A., Maigret, B., (1993) *Molecular Simulation* **11** 251

DOE (1987). *Mission Directed Goals for Electronic Vehicle Battery Research and Developement.* Department of Energy, November 1987. DOE/Ce-0148, Revision 1.

EimEli, Y., Lu, S.H., Rzeznik, M.A., (1998) *J. Electrochem. Soc.* **145** 3383

EimEli, Y., Vaughey, J.T., Thackeray, M.M., Mukerjee, S., Yang, X.Q., McBreen. J., (1999) *J. Electrochem. Soc.*, **146** 908

Endo, M., Kim, C., Nishimura, K., Fujino, T., Miyashita, K., (2000) *Carbon*, **38** 183

Enjalbert, R., Galy, J., (1986) *Acta Cryst.* **C42** 1467

Ewald, R.P., (1921) *Ann. Physik* **64** 253

Fey, G.T-K., Li, W., Dahn. J.R., (1994) *J. Electrochem Soc.*, **141** 2279

Flandrois, S., Simon, B., (1999) *Carbon* **37** 165

Fletcher, R., Powell, M.J.D., (1963) *Computer J.*, **13** 185

Fletcher, D.A., McMeeking, R.F., Perkin, D., (1996) The United Kingdom Chemical Database Service, *J. Chem. Inf. Comput. Sci.* **36** 746-749

Fowler, P.W., Madden, P.A., (1983) *Mol. Phys.*, **49** 913

Gale, J.D., (1996) *Phil. Mag. B*, **73** 3

Gale, J.D., (1997) *JCS Faraday Trans.* **93** 629

Galy, J.D., (1992) *J. Solid State Chem.* **100** 229

Gillan, M.J., (1991), 'Calculating the Properties of Materials from Scratch' in 'Computer Simulation in Materials Science' ed. Meyer and Pontikis, Kluwer Academic Publishers.

Goldsmidt, V.M., (1926), *Skrifter Norske Videnskaps-Akad. Oslo, I. Mat. Naturv. Kl.* No. 1

Gordon, R.G., Kim, Y.S., (1972) *J. Chem.Phys.*, **56** 3122

Grimes, R.W., Catlow, C.R.A., (1990) *J. Am. Ceramic Soc.* **73** 3251

Gschneider Jr., K.A., (1964), *Solid State Physics Vol. 16,* New York: Academic, p.276

Gunnarsson, O., Lundquist, I., (1976) *Phys. Rev. B* **13** 4274

Hamann, D.R., Schlüter, M., Chiang, C., (1979) *Phys. Rev. Lett.* **43** 1494

Harding, J.H., (1989) *J. Chem. Soc. - Faraday Trans. II* **85** 351

Hedin, L., Lundqvist, S.J., (1972) *J. Phys. (France),* **33** C3-73

Hirshfeld, F.L., *Acta Cryst.* 1971 **B27** 769

Hohenberg, P., Kohn, W., (1964) *Phys. Rev. A* **136** 864

Islam, M.S., Catlow, C.R.A., (1988) *J. Phys. Chem. Solids,* **49** 119

Islam, M.S., (1993) *Phil. Mag. B* **68** 667

Johnston, W.D., Heikes, R.R., Sestrich, D., (1958) *J. Phys. Chem. Solids,* **7** 1

Kawai, H., Nagata, M., Tabuchi, M., Tukamoto, H., West, A.R., (1998a) *Chem. Mater.*, **10** 3266

Kawai, H., Nagata, M., Tukamoto, H., West, A.R., (1998b) *J. Mater. Chem.*, **8** 837

Kawai, H., Nagata, M., Kageyama, H., Tukamoto, H., West, A.R., (1999) *Electrochimica Acta,* **45** 315

Kempf, J.Y., Silvi, B., Dietrich, A., Catlow, C.R.A., Maigret, B., (1993) *Chem. Mater.* **5** 641

Ketelaar, J.A.A., (1936) *Nature* **137** 316

Kohn, W., Sham, L., (1965) *Phys. Rev. A* **140** 1133

Koksbang, R., Baker, J., Shi, H., Saidi, M.Y., (1996) *Solid Sate Ionics*, **84** 1

Kresse, G., Furthmuller, J., (1996a) *Phys. Rev. B* **54** 169

Kresse, G., Furthmuller, J., (1996b) *Comput. Mater. Sci.* **6** 15

Lidiard, A.B., Norgett, M.J., (1972), *'Computational Solid State Physics'*, eds. F. Hermann, Dalton, N.W., Koehler, T.R., Plenum, New York, pp 385

Mackrodt, W.C., Harrison, N.M., Saunders, V.R., Allan, N.L., Towler, M.D., (1996) *Chem. Phys. Lett.*, **250** 66

Mackrodt, W.C., Williamson, E.A., (1998) *Phil. Mag. B*, **77** 1077

Mansingh, A., Singh, R., Sayer, M., *J. of Phy. and Chem of Solids* (1984) **45** 79

Monkhorst, H.J., Pack, J.D., (1976) *Phys. Rev. B*, **13** 5188

Mott, N.F., Littleton, M.J., (1938) *Trans Faraday Soc.* **34** 485

Murphy, D.W., Christian, P.A., DiSalvo, F.J., Carides, J.N., (1979a) *J. Electrochem. Soc.* **126** 497

Murphy, D.W., Christian, P.A., DiSalvo, F.J., Waszczak, J.V., (1979b) *Inorg. Chem.* **18** 2800

Nelder, J.A., Mead, R., (1965) *Computer Journal* **7** 308

Ohzuku, T., Ueda, A., (1994) *J. Electrochem. Soc.* **141** 2972

Pavlides, P., Catlow, C.R.A., (1994) *Molecular Physics* **81** 1269

Perdew, J.P., Zunger, A., (1981) *Phys. Rev. B* **23** 5048

Perdew, J.P., (1986) *Phys. Rev. B*, **33** 8822

Perdew, J.P., Wang, Y., (1992) *Phys. Rev. B* **46** 6671

Press, W.H., Teukolsky, S.A., Vetterling, W.T., Flannery, B.P., (1992), Numerical Recipes. Cambridge University Press, Cambridge. 2nd edition,

Prouzet, E., Cartier, C., Villain, F., Tranchant, A., (1996) *J. Chem. Soc., Faraday Trans.* **92** 103

Rogers, K.D., (1996) *Powder Diffraction,* **8** 240

Sayle, D.C., Catlow, C.R.A., Perrin, M.A., Nortier, P., (1996a) *Cat. Let.* **38** 203

Sayle, D.C., Catlow, C.R.A., Perrin, M.A., Nortier, P., (1996b) *J. Phys. Chem.*, **100** 8940

Sayle, D.C., Gay, D.H., Rohl, A.L., Catlow, C.R.A., Harding, J.H., Perrin, M.A., Nortier, P., (1996c) *J. Mater. Chem.*, **6** 653

Shibuya, M., Yamamura, S., Matsue, T., Uchia, I., (1995) *Chem. Let.* **8** 749

Sigala, C., Guyomard, D., Verbaere, A., Piffard, Y., Tournoux, M., (1995) *Solid State Ionics*, **81** 167

Stone, A.J., Alderton, M., (1985) *Molecular Physics* **56** 1047

Sutton, A.P., (1993), 'Electronic Structure of Materials'. Oxford University Press.

Tarascon, J.M., McKinnon, W.R., Coowar, F., Bowmer, T.N., Amatucci, G., Guyomard, D., (1994) *J. Electrochem Soc.*, **141** 1421

Tomlinson, S.M., Freeman, C.M., Catlow, C.R.A., Donnerberg, H., Leslie, M., (1989) *J. Chem. Soc., Faraday Trans. II* **85** 367

Tosi, M.P., (1964) *Solid State Phys.* **16** 1

Vanderbilt, D., (1990) *Phys. Rev. B,* **41** 7892

Van der Ven, A., Ceder, G., (1999) *Phys. Rev. B,* **59** 742

Vivier, V., Farcy, J., Pereira-Ramos, J-P., (1998) *Electrochemica Acta.* **44** 831

Wedepohl, P.T., (1967) *Proc. Phys. Soc.*, **92** 79

Weinert, M., Wimmer, E., Freeman, A.J., (1982) *Phys. Rev. B,* **26** 4571

West, K., Zachau-Christiansen, B., Jacobsen, T., (1983) *Electrochimica Acta* **28** 1829

West, K., Zachau-Christiansen, B., Jacoben, T., Atlung, S., (1985) *J. Power Sources*, **14** 235

West, K., Zachau-Christiansen, B., Jacobsen, T., Skaarup S., (1993) *Electrochimica Acta.* **38** 1215

West, K., Zachau-Christiansen, B., Jacobsen, T., Skaarup S., (1995) *Solid State Ionics* **76** 15

Westman, S., (1961) *Acta Chem. Scand.* **15** 217

White, J.A., Bird, D.M., (1994) *Phys. Rev. B* **50** 4954

Whittingham, M.S., (1976) *J. Electrochem. Soc.* **132** 315

Wilhelmi, K-A., Waltersson, K., Kihlborg, L., (1971) *Acta Chem. Scand.* **25** 2675

Williford, R.E., Begg, B.D., Weber, W.J., Hess, N.J., (2000) *J. Nuclear Mat.* **278** 207

Winter, M., Besenhard, J.O., (1999) *Electrochimica Acta*, **45** 31

Wolfenstine, J., Sakamoto, J., Huang, C.K., (1998) *J. Power Sources* **75** 181

Wolverton, C., Zunger, A., (1998) *Phys. Rev. B* **81** 606

Woodley, S.M., Battle, P.D. Gale, J.D., Catlow, C.R.A., (1999) *Phys. Chem. Chem. Phys.* **1** 2535

Woodley, S.M., Catlow, C.R.A., Piszora, P., Stempin, K, Wolska, E., (2000) *J. Solid State Chem*, in press.

Zhang, J-G., Liu, P., Turner, J.A., Tracy, C.E., Benson, D.K., (1998) *J. Electrochem. Soc.* **145** 1889

Zhong, Q., Bonakdarpour, A., Zhang, M., Gao, Y., Dahn, J.R., (1997) *J. Electrochem Soc.*, **144** 205